# A fresh look at the pre-industrial air-sea carbon flux using the alkalinity budget

Alban Planchat<sup>1,2,3</sup>, Laurent Bopp<sup>1</sup>, and Lester Kwiatkowski<sup>4</sup>

**Correspondence:** Alban Planchat (alban.planchat@unibe.ch)

Abstract. The disparities in Disparities between observational and model-based estimates of the ocean carbon sink, whether derived from observations or models, raise questions about our ability to accurately assess its magnitude and trend persist, highlighting the need for improved understanding and methodologies to reconcile differences in both magnitude and trends over recent decades. A potential factor contributing to this inconsistency is key source of uncertainty lies in the pre-industrial air-sea air–sea carbon flux, which is thought to arise essential for isolating the anthropogenic component from observations. This flux, thought to result globally from an imbalance between riverine discharge and sediment burial of carbon. The characterization of this flux is essential for isolating the anthropogenic component of the total air-sea carbon flux estimated from observations; however, it, remains highly uncertain, limiting confidence in the impactful applications of the confidence in impactful applications such as the Global Carbon Budget (GCB). In this study, we propose a fresh look at the pre-industrial air-sea carbon flux using the alkalinity budget. We demonstrate the relevance of a novel-present a new theoretical framework that directly enables the calculation enables direct estimation of the riverine/burial-driven pre-industrial carbon outgassing using both carbon and alkalinity budgets. We also introduce a practical framework to evaluate the spatial distribution of this flux through a This approach is validated with a series of ocean biogeochemical simulations. Our reassessment, grounded in existing earbon and alkalinity budgets, yields an estimated riverine, which also highlight the main factors influencing its regional distribution. We then demonstrate the utility of the framework through two proof-of-concept applications. The first revisits the pre-industrial riverine/burial-driven pre-industrial carbon outgassing of 0.49 [0.34; 0.70] PgC yr<sup>-1</sup>, which is lower than the most recent central estimate of  $0.65 \pm 0.30$  PgC yr<sup>-1</sup>. This adjustment partially reduces the disparities between observation-based and model-derived estimates of the anthropogenic ocean carbon sink. Using a composite simulation derived from a linear combination of our sensitivity experiments, we reassess the spatial distribution of this flux, attributing 29 % to the southern region (south of 20°S), 40 % to the inter-tropical region (20°S-20°N), and 31 % to the northern region (north of 20°N). Notably, these findings represent an intermediate distribution compared to those used in the GCB over time, with recent values at 14 %, 64 %, and 22 %, and historical values at 49 %, 25 %, and 26 %. Addressing the current inconsistencies between the combined air sea carbon flux using existing carbon and alkalinity budgets, offering a simple method for reassessment as these budgets are updated. The second application leverages sensitivity simulations to construct a composite simulated

<sup>&</sup>lt;sup>1</sup>LMD-IPSL, CNRS, Ecole Normale Supérieure/PSL Res. Univ, Ecole Polytechnique, Sorbonne Université, Paris, 75005, France

<sup>&</sup>lt;sup>2</sup>Climate and Environmental Physics, Physics Institute, University of Bern, Bern, Switzerland

<sup>&</sup>lt;sup>3</sup>Oeschger Centre for Climate Change Research, University of Bern, Bern, Switzerland

<sup>&</sup>lt;sup>4</sup>LOCEAN, Sorbonne Université-CNRS-IRD-MNHN, Paris, 75005, France

estimate that aligns with both carbon and alkalinity budgets is thus an urgent priority for building confidence in the global to assess the regional distribution of the pre-industrial riverine/burial-driven pre-industrial carbon outgassing, and intermodel comparisons are required to constrain its regional distributionair—sea carbon flux. This approach is well suited for model intercomparisons, enabling efficient reassessment of regional flux patterns and helping to reduce biases related to ocean model physics or biogeochemical parameterizations.

#### 30 1 Introduction

50

Accurately estimating the anthropogenic carbon sink in the ocean is crucial for gaining a deeper understanding of the underlying mechanisms, and is a prerequisite for projecting its future evolution and the climate response to future emissions scenarios (Canadell et al., 2021). This anthropogenic carbon flux is currently assessed with yearly updates by the Global Carbon Budget (GCB; Friedlingstein et al., 2024), using both observational products and model simulations employing Global Ocean Biogeochemical Models (GOBMs). Nevertheless, reconstructions based on However, reconstructions derived from surface ocean pCO<sub>2</sub> data, which constitute the primary—currently the main observation-based methods, mostly exceed the model estimates, both at the global and regional scale (e.g. Hauck et al., 2020; Crisp et al., 2022; Friedlingstein et al., 2024). This disparity has grown approach—tend to yield higher estimates than models, both globally and regionally. This mismatch has grown steadily since the early 2000s, now reaching a 10to—20 % difference over the past decade (Friedlingstein et al., 2024) (e.g. Hauck et al., 2020; DeVries et al., 2023; Gruber et al., 2023; Friedlingstein et al., 2024).

Recent studies have begun to investigate the origins of discrepancies in both the magnitude and trend of observational versus model-based estimates of the ocean anthropogenic carbon sink. Analyses of GOBM-derived estimates (Terhaar et al., 2024) and pCO<sub>2</sub>-based products (Ford et al., 2024) point to multiple sources of uncertainty, including methodological differences, model biases, and data limitations. On the modeling side, GOBMs have been shown to underestimate the global sink magnitude (Terhaar et al., 2022), as well as decadal variability, especially in the Southern Ocean (Mayot et al., 2023, 2024). On the observational side, the sparse and uneven spatial and temporal coverage of surface ocean pCO<sub>2</sub> measurements remains a major limitation (Hauck et al., 2023; Landschützer et al., 2023; Dong et al., 2024). While the causes of these mismatches are likely multifaceted, one less-discussed contributor is the uncertainty surrounding the pre-industrial air–sea carbon flux and its influence on pCO<sub>2</sub>-based estimates.

The net air-sea carbon flux derived from  $pCO_2$ -based data encompasses both anthropogenic and natural components. The natural component originates, at the global scale, from the balance between riverine discharge and the burial of organic matter (OM) and calcium carbonate (CaCO<sub>3</sub>). As these external fluxes together represent a net source of carbon for the ocean, they result in a net carbon outgassing at equilibrium steady state during the pre-industrial era. Consequently, assessing the anthropogenic carbon flux through observations requires determining the pre-industrial riverine/burial-driven air-sea carbon flux and its spatial distribution (e.g. Hauck et al., 2020; Friedlingstein et al., 2024).

Assessing this outgassing carbon flux remains highly uncertain, with estimates ranging from 0.23 to 0.78 PgC yr<sup>-1</sup> (Aumont et al., 2001; Jacobson et al., 2007; Resplandy et al., 2018; Lacroix et al., 2020; Regnier et al., 2022), depending on the

modeling approach used to derive them (forward or inverse) and literature estimates of riverine and burial fluxes (see Table E1). Specifically, the most recent estimate of  $0.65 \pm 0.30$  Pg Cyr<sup>-1</sup> is that used in the latest GCB release (Regnier et al., 2022; Friedlingstein et al., 2024, Table 1).

The spatial distribution of this riverine/burial-driven air-sea carbon flux is also highly uncertainand. It strongly depends on the assumptions and methods used for its assessment to assess it, including how sediment burial processes are represented, and both the magnitude and characteristics of riverine carbon inputs – particularly the balance between organic and inorganic forms, as well as the lability of terrestrial organic matter – (see Table E1). The historical value, obtained earlier estimate, derived from a modeling analysis (Aumont et al., 2001) , and used for a long time in the GCB, distributes distributed this flux as follows: 49 % in the southern region, 25 % in the inter-tropical region, and 26 % in the northern region. In contrast, the latest most recent estimate, currently used in the GCB and also based on a modeling study (Lacroix et al., 2020, Table 1), evaluates this distribution as suggests a very different partitioning: 14 %, 64 % and 22 %, respectively, which completely reshapes the reshaping our understanding of the regional distribution of this flux.

70

85

The uncertainties associated with Uncertainties in estimating the riverine/burial-driven pre-industrial outgassing may contribute to disparities the persistent discrepancies between observation-based and model-derived estimates of the anthropogenic ocean carbon sink, both globally and regionally (Friedlingstein et al., 2024, their Fig. 11 and 14). These disparities have emerged and disappeared without apparent reason, often in conjunction with fluctuated over time, largely in response to stepwise adjustments made by the GCB team following new reassessments of the riverine/burial-driven pre-industrial outgassing and its distribution, as well as the choices made within the GCB magnitude and spatial distribution of this flux in the literature (Fig. 1and, Table 1). For instance, there was a notable global decrease in riverine/burial-driven a substantial decrease in the global estimate of the pre-industrial outgassing from 2019 to 2020, which contributed to a significant reduction in discrepancies. Additionally, a regional shift occurred notable narrowing of the global observation—model gap. More recently, from 2022 to 2023, characterized by a reduction in bias in the southern region and a corresponding redistribution of the flux between regions, from the southern region to the tropics, led to a reduced southern hemisphere bias and a compensating increase in the inter-tropical region discrepancy.

Enhancing our understanding of the riverine/burial-driven air-sea carbon flux is critical to achieving more precise estimates of the anthropogenic carbon flux and its distribution from data-driven assessments. Numerical models are a promising approach to hold great promise in addressing this challenge, especially when estimating its distribution particularly for estimating the spatial distribution of the flux. However, at present, the representation of the pre-industrial air-sea carbon flux remains uncertain in inter-model comparison exercises like CMIP6 (the 6th phase of the Coupled Model Intercomparison Project, Eyring et al., 2016) and the 2022 GCB (Friedlingstein et al., 2024)2024 GCB (Friedlingstein et al., 2024), likely due to differences in model setups and various/incomplete representations of sediment burial and riverine discharge (Terhaar et al., 2024). The magnitude of this global net flux ranges from -0.73 to 0.38 PgC yr<sup>-1</sup>, while its inter-hemispheric gradient, defined as the difference between its values in the northern and southern hemispheres, ranges from -0.09 to 0.82 PgC yr<sup>-1</sup> (Fig. 1a).

The methods employed thus far to estimate the riverine/burial-driven air-sea carbon flux at the global scale mostly rely on closing the ocean carbon budget. However, they often exhibit limitations in addressing the ocean alkalinity budget. Alkalinity

**Table 1.** Review of the air-sea carbon outgassing from riverine/burial fluxes of carbon and Alk used in the GCBs. Both the global values and their regional distribution are presented, along with the associated references.

	Air-sea carbon out	gassing from r	iverine/burial fluxes of c	arbon and A	lk		
	Global		Distribution				
GCB	Reference(s)	C+C 1	Reference	GtC yr-1 (%)			
	Reference(s)	GtC yr-1	Reference	South	Inter-tropics	North	
2023 to 2024	Regnier et al. (2022)	$0.65 \pm 0.3$	Lacroix et al. (2020)	0.09 (14)	0.42 (64)	0.14 (22)	
2022	Regnier et al. (2022)	0.65	Aumont et al. (2001)	0.32 (49)	0.16 (25)	0.17 (26)	
2020 to 2021	Jacobson et al. (2007)	0.61	Aumont et al. (2001)	0.30 (49)	0.15 (25)	0.16 (26)	
2020 to 2021	& Resplandy et al. (2018)	0.01	Aumont et al. (2001)	0.30 (49)	0.13 (23)	0.10 (20)	
2018 to 2019	Resplandy et al. (2018)	0.78	Aumont et al. (2001)	0.38 (49)	0.19 (25)	0.20 (26)	
2013 to 2017	Jacobson et al. (2007)	0.45	Not applicable				
1959-2011	Not applicable						

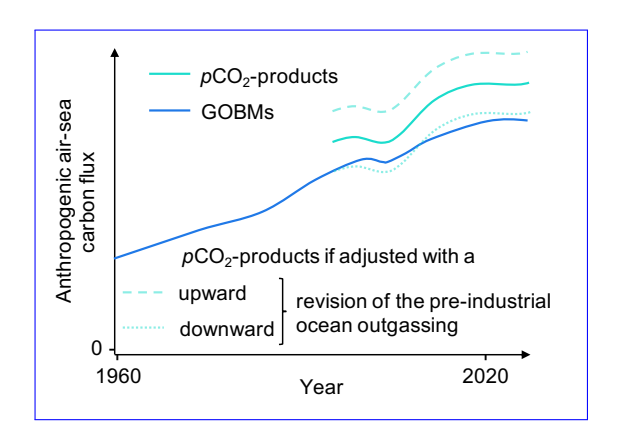


**Figure 1.** Schematic illustration of how a bias in evaluating the pre-industrial ocean carbon outgassing affects the assessment of the anthropogenic carbon flux based on  $pCO_2$ -products. A downward revision of the pre-industrial outgassing would decrease anthropogenic carbon flux estimates based on  $pCO_2$ -products, while an upward revision would increase it. This effect applies both globally and regionally.

(Alk), defined as the excess of proton acceptors over proton donors, or of positive conservative charges over negative ones, plays a pivotal role in driving air-sea carbon exchanges, which are strongly dependent on the relative balance between Alk and dissolved inorganic carbon (DIC; e.g. Humphreys et al., 2018). Similar to carbon, the Alk budget is controlled by both sources and sinks at the boundaries of the oceanic domain (Middelburg et al., 2020). Conventionally, it is hypothesized that the global Alk inventory has been in equilibrium conserved during the pre-industrial era, with Alk riverine discharge compensated by the burial of CaCO<sub>3</sub> (e.g. Revelle and Suess, 1957; Aumont et al., 2001; Planchat et al., 2023). balancing the Alk riverine discharge (e.g. Revelle and Suess, 1957; Aumont et al., 2001; Planchat et al., 2023).

Nonetheless, the hypothesis of a potentially disequilibrated global Alk inventory an imbalanced Alk budget during the preindustrial era remains plausible, considering the overall balance of based on estimates of global Alk sources and sinks (e.g. Milliman, 1993; Middelburg et al., 2020). Such an Alk inventory disequilibrium would drive a disequilibrium in the global

100

earbon inventory and affect the air-sea carbon flux. This hypothesis gains additional support from paleoclimatology studies, which suggest the possibility of an Alk inventory disequilibrium due to Paleoclimatic studies suggest that such an imbalance could arise from additional CaCO<sub>3</sub> burial (e.g. Cartapanis et al., 2018) or from a carbonate compensation mechanism involving biological processes alongside riverine input (Boudreau et al., 2018). inputs (Boudreau et al., 2018). Unlike carbon, Alk is not exchanged with the atmosphere, so balancing its budget depends on processes acting over longer timescales, particularly through interactions with the continents (e.g. erosion) and marine biogeochemistry (e.g. sediment dynamics). As a result, Alk budget balancing is slow, yet interactive with the carbon cycle through changes in atmospheric CO<sub>2</sub> and ocean acidity (Hain et al., 2014). An imbalance in the Alk budget would induce an additional air–sea carbon flux beyond that directly inferred from the ocean carbon budget, ultimately resulting in a non-conserved global ocean carbon inventory.

Here, we reevaluate the riverine/burial-driven take a fresh look at the pre-industrial air-sea air-sea carbon flux by introducing a new theoretical framework that uses enables direct estimation of the riverine/burial-driven pre-industrial carbon outgassing, based on both carbon and Alk budgets. After testing the approach through a series of sensitivity simulations using a global biogeochemical model and covering a broad spectrum of uncertainties related to riverine and burial fluxes, we derive a new estimate of the We validate this approach using a suite of ocean biogeochemical simulations, which also help identify the key drivers of its regional distribution. We then demonstrate the utility of this framework through two proof-of-concept applications: (i) revisiting the global magnitude of the pre-industrial riverine/burial-driven pre-industrial air-sea carbon flux based on air-sea carbon flux using existing carbon and Alk budgets. Subsequently, using a practical framework, we reassess the spatial distribution of the flux by constructing a-; and (ii) reassessing its regional distribution using sensitivity simulations to construct a composite simulated estimate from a linear combination of our sensitivity simulations consistent with both budgets.

#### 2 Methods

105

In this study, we use 'steady-state' to refer to the temporal stability of the globally integrated air—sea carbon flux. We describe the carbon and Alk budgets as 'balanced' or 'imbalanced' according to whether fluxes into and out of the ocean are quantitatively balanced. An imbalanced budget drives a deviation in the global inventory: a positive (resp. negative) imbalance leads to an increase (resp. decrease) in the global inventory. Unless otherwise stated, all simulations and results refer to pre-industrial conditions.

#### 2.1 Overview and definitions Theoretical framework

### 2.1.1 Global-Governing equation of the pre-industrial riverine/burial-driven air-sea carbon flux

The collection of surface ocean  $pCO_2$  data, and associated statistical methods, only allow for the direct reconstruction of the contemporary air-sea carbon flux ( $F_{\text{cont.}}^{\text{C, air-sea}}$ ), which encompasses both an anthropogenic ( $F_{\text{ant.}}^{\text{C, air-sea}}$ ) and a natural ( $F_{\text{nat.}}^{\text{C, air-sea}}$ ) component (e.g. Hauck et al., 2020), as follows:

$$F_{\text{cont.}}^{\text{C, air-sea}} = F_{\text{ant.}}^{\text{C, air-sea}} + F_{\text{nat.}}^{\text{C, air-sea}}$$

$$\tag{1}$$

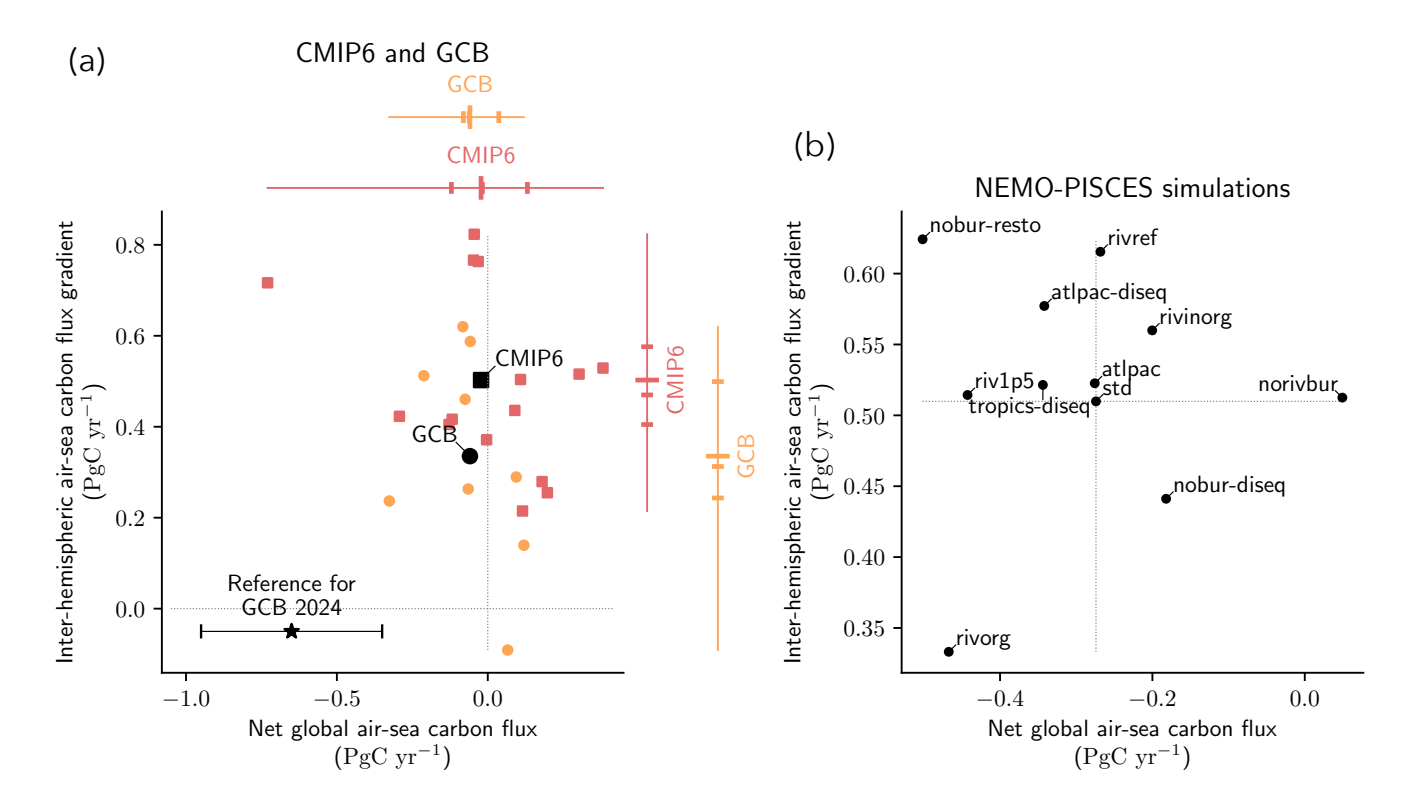


**Figure 2.** Pre-industrial air-sea carbon flux from models. The globally integrated pre-industrial flux (x-axis) and its interhemispheric gradient (y-axis) are indicated for (a) CMIP6 Earth system models (ESMs) and GCB Global Ocean Biogeochemical Models (GOBMs), as well as for (b) the NEMO-PISCES sensitivity simulations. (a) The 15 CMIP6 ESMs (10 GCB GOBMs; see Appendix B1) are plotted with red squares (orange circles). The black square and circle refer to the CMIP6 and GCB ensemble means. The CMIP6 and GCB ensemble ranges (line), mean (major tick) and quartiles (minor ticks) are respectively displayed to the top and right in red and orange. The star refers to the reference value used in the GCB 2024 (Table 1; Friedlingstein et al., 2024). The inter-hemispheric air-sea carbon flux gradient is defined as the difference between its values in the northern and southern hemispheres (Sect. 2.1.3).

where all-positive fluxes are directed into the ocean (consistent throughout this manuscript). Therefore, it is crucial to determine the natural component to extract the anthropogenic carbon flux from  $pCO_2$ -based products. Within the anthropogenic carbon flux, we incorporate the perturbation of the natural carbon flux in response to climate change, ensuring that  $F_{\rm ant.}^{C, \, \rm air-sea}$  genuinely represents fully reflects the carbon sink resulting from all human-induced disturbances (e.g. Hauck et al., 2020). Additionally, we assume that there have been no alterations to riverine and burial fluxes in response to the Anthropocene, allowing us to directly consider Accordingly.  $F_{\rm nat.}^{C, \, \rm air-sea}$  is directly defined as the riverine/burial-driven pre-industrial (mention generally omitted hereafter) air-sea carbon flux ( $F_{\rm riv}^{C, \, \rm air-sea}$ ), i.e.:

135

140

$$F_{\text{nat.}}^{\text{C, air-sea}} = F_{\text{riv./bur.}}^{\text{C, air-sea}}$$
(2)

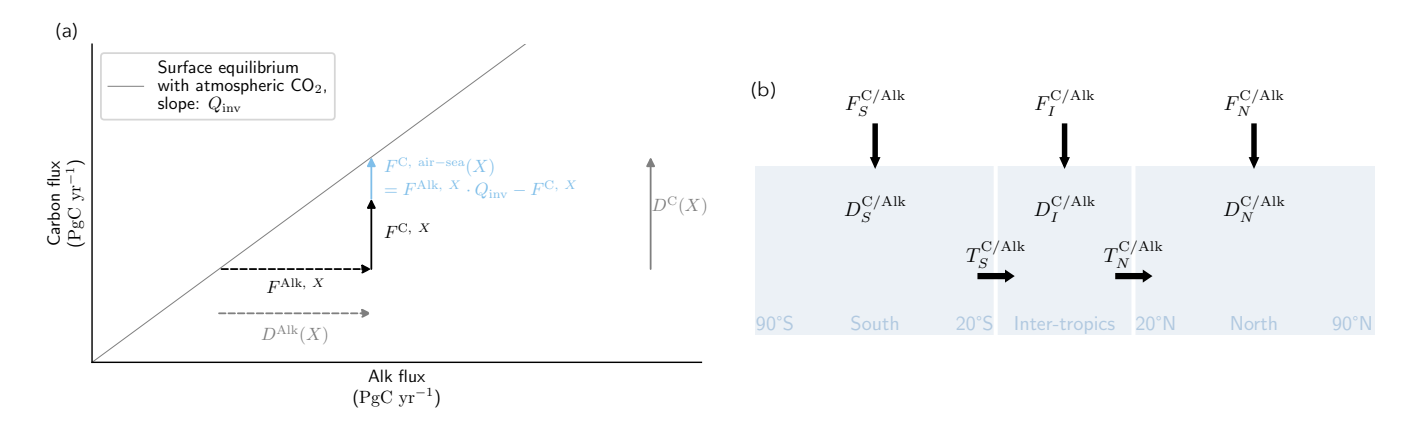


Figure 3. Schematics of the thereotical theoretical framework introduced in this manuscript. (a) Schematic construction for Conceptual representation of a process X (e.g. CaCO<sub>3</sub> burial), impacting which affects carbon  $(F^{C, X})$  and Alk  $(F^{Alk, X})$ , of the air-sea thereby induces, at steady state, a compensating carbon flux resulting from the associated local imbalance  $(F^{\prime C, air-sea}(X)F^{C, air-sea}(X))$ , as well as and the related disequilibrium resulting deviations in carbon and Alk inventories  $(D^{\prime C/Alk}(X)D^{C/Alk}(X))$ . The surface equilibrium of the Alk:DIC pair with atmospheric CO<sub>2</sub> is represented by a solid grey line. Carbon (Alk) fluxes are represented through solid (dashed) arrows, and the colors of the arrows is consistent with what is used throughout the manuscript (e.g. Fig. 2). The combination of the Alk and carbon fluxes associated with the process X results in a disequilibrium with the atmospheric CO<sub>2</sub> concentration, and requires an air-sea earbon flux to restore equilibrium. (b) Schematic diagram of carbon and Alk budgets by ocean region.  $F^{C/Alk}$  and  $T^{C/Alk}$  respectively refer to the total external fluxes (directed into the ocean) and to the northward transport of carbon and Alk.  $D^{C/Alk}$  corresponds to the carbon and Alk inventory disequilibria deviations in each basin. S, I and N refer to the different ocean regions, respectively the southern hemisphere, the inter-tropical zone, and the northern hemisphere.

The anthropogenic carbon flux can then be derived from  $pCO_2$ -based data as follows:

$$F_{\text{ant.}}^{\text{C, air-sea}} = F_{\text{cont.}}^{\text{C, air-sea}} - F_{\text{riv./bur.}}^{\text{C, air-sea}}$$
(3)

When assuming a global Alk inventory equilibrium Assuming a steady-state pre-industrial air—sea carbon flux and a balanced

Alk budget, the global riverine/burial-driven air—sea carbon flux can be directly deduced from the carbon budget at

equilibrium inferred by closing the ocean carbon budget (e.g. Regnier et al., 2022):

$$F_{\text{riv./bur.}}^{\text{C, air-sea}} + F^{\text{C, riv./bur.}} = 0$$

$$\tag{4}$$

with:

$$F^{C, \text{ riv./bur.}} = F^{C, \text{ riv.}} + F^{C, \text{ bur. org.}} + F^{C, \text{ bur. inorg.}} + F^{C, \text{ minor components}}$$
(5)

where 'riv.' stands for 'riverine discharge', 'bur. org.' for 'OM burial', 'bur. inorg.' for 'CaCO<sub>3</sub> burial', and 'minor components' encompass other minor external fluxes, such as carbon release by mid-ocean ridges and groundwater discharge. Thus, assuming a conserved pre-industrial global Alk inventoryequilibrium, the riverine/burial-driven air-sea carbon flux is the opposite of the

riverine and burial fluxes of carbon:

$$F_{\text{riv./bur.}}^{\text{C, air-sea}} = -F^{\text{C, riv./bur.}}$$
(6)

However, when considering a pre-industrial imbalanced Alk budget (i.e. a non-conserved global Alk inventorynot in equilibrium), it becomes essential necessary to account for the Alk balance in order budget explicitly to infer the riverine/burial-driven air-sea carbon flux:

$$F^{\text{Alk, riv./bur.}} = F^{\text{Alk, riv.}} + F^{\text{Alk, bur. org.}} + F^{\text{Alk, bur. inorg.}} + F^{\text{Alk, minor components}}$$
(7)

where 'minor components' encompass this time other minor external fluxes such as anaerobic processes, silicate weathering, and groundwater discharge. Importantly, under the assumption of a steady-state system – that is, with a stable air–sea carbon flux –, any imbalance in alkalinity (Alk ) triggers a corresponding carbon fluxto achieve equilibrium with the atmospherethe Alk budget induces a compensating carbon flux. To estimate this flux, we extend the conceptual framework introduced by Humphreys et al. (2018) by utilizing a phase diagram (Alk, DIC) in the form of an Alk and DIC flux diagram, while operating on a global scale (Fig. 3a). For any flux affecting carbon and/or Alk, it is possible to derive an air-sea carbon flux and the associated global carbon and Alk inventory imbalances. This approach relies on the equilibrium relationship between the Alk-DIC pair and the Alk:DIC pair and atmospheric CO<sub>2</sub>eoncentration. At global scale, at equilibriumsteady-sate, any deviation in Alk is directly proportional to a DIC anomaly, and this proportionality coefficient can be estimated with high precision, as follows:

$$Q_{\rm inv} \simeq \frac{\text{Alk}}{3 \cdot \text{Alk} - 2 \cdot \text{DIC}}$$
 (8)

where  $Q_{\rm inv}$ , as previously defined in Planchat et al. (2023), represents the inverse of the 'isocapnic quotient' approximation introduced by Humphreys et al. (2018). In the case of an ocean at equilibrium (Humphreys et al., 2018, see Appendix A). In this study,  $Q_{\rm inv}$  is defined based on the mean surface values of Alk and DIC. In the case of a steady-state air-sea carbon flux (see Fig. B1), every external flux-process X (e.g. riverine discharge) that exerts an impact on carbon ( $F^{\rm C, X}$ ) and/or Alk ( $F^{\rm Alk, X}$ ), results in a global imbalance, shifting the surface ocean away from equilibrium with the atmosphere. Specifically, this requires an air-sea carbon flux ( $F^{\rm C,air-sea}(X)$ ; Fig. 3a) to maintain global equilibrium with respect to the atmospheric CO<sub>2</sub>eoncentration. This also leads to disequilibria deviations in global carbon and Alk inventories ( $D^{\rm C}$  and  $D^{\rm Alk}$ , respectively). In summary, for any given process X, we can define:

$$\begin{cases}
F^{\text{C, air-sea}}(X) = F^{\text{Alk, } X} \cdot Q_{\text{inv}} - F^{\text{C, } X} \\
D^{\text{C}}(X) = F^{\text{Alk, } X} \cdot Q_{\text{inv}} \\
D^{\text{Alk}}(X) = F^{\text{Alk, } X}
\end{cases} (9)$$

Applying this theoretical framework to the total external carbon and Alk fluxes ( $F^{C, riv./bur.}$  and  $F^{Alk, riv./bur.}$ , respectively), we can deduce the riverine/burial-driven air-sea carbon flux ( $F^{C, air-sea}_{riv./bur.}$ ) and the respective disequilibria deviations in global carbon and Alk inventories as follows:

$$\begin{cases}
F_{\text{riv./bur.}}^{\text{C, air-sea}} = F^{\text{Alk, riv./bur.}} \cdot Q_{\text{inv}} - F^{\text{C, riv./bur.}} \\
D^{\text{C}} = F^{\text{Alk, riv./bur.}} \cdot Q_{\text{inv}} \\
D^{\text{Alk}} = F^{\text{Alk, riv./bur.}}
\end{cases} (10)$$

It is worth noting that this general expression also applies to the specific case where the global Alk inventory is in equilibrium conserved ( $F^{Alk, riv./bur.} = 0$ ).

# 2.1.2 Air-sea-Regional proxies for the spatial distribution of the pre-industrial riverine/burial-driven air-sea carbon fluxfrom local/regional imbalance

While it is feasible to establish a A direct relationship between the influence of carbon and Alk fluxes on the net air-sea carbon flux at the global seale and the net global air-sea carbon flux can be established under the assumption of an equilibrated ocean steady-state air-sea carbon flux. However, this approach is not directly applicable at the local or regional scaledue to the complex dynamics of ocean circulation, which transport both earbon and Alk, does not apply directly at the regional scale, where ocean circulation transports both Alk and DIC, and biogeochemical processes also generate regional sources and sinks.

# The concept of the regional carbon: Alk budget imbalance

185

190

195

200

To gain a deeper understanding of the factors shaping the spatial distribution of the riverine/burial-driven air-sea carbon flux, we expand upon the theoretical framework previously outlined for the global scale (refer to Section 2.1.1) and adapt it as a proxy for application at local and regional scales.

Indeed, at local/regional scale, this conceptual tool only permits estimates of a potential. This is essential to understanding the extent to which specific regional carbon: Alk budget imbalances can drive the global air-sea carbon flux resulting from a local/regional carbon: Alk imbalance (Fig. 3a). Specifically, this as well as deviations in carbon and Alk inventories.

The air-sea carbon flux calculated by applying Eq. 10 to the riverine and burial fluxes of a specific region can only be considered a potential air-sea carbon flux, defined locally/regionally, only becomes effective at equilibrium and at i.e. a capacity to generate such a flux at the global scale. There is indeed no guarantee of its local/regional applicability due to the transport of the induced carbon :Alklocal/regional imbalance. In summary, we can adapt Eq. 9 for any process X affecting carbonand/or Alk, and for a given latitude (lat) with zonally integrated values, or for a specific ocean region (south: S, inter-tropies: I, north: N):

$$\begin{cases} F_{\mathrm{lat}/N/S/I}^{\prime\mathrm{C, \, air-sea}}(X) = F_{\mathrm{lat}/N/S/I}^{\mathrm{Alk}, \, X} \cdot Q_{\mathrm{inv, \, lat}/N/S/I} - F_{\mathrm{lat}/N/S/I}^{\mathrm{C, \, X}} \\ D_{\mathrm{lat}/N/S/I}^{\prime\mathrm{C, \, X}} = F_{\mathrm{lat}/N/S/I}^{\mathrm{Alk}, \, X} \cdot Q_{\mathrm{inv, \, lat}/N/S/I} \\ D_{\mathrm{lat}/N/S/I}^{\prime\mathrm{Alk}, \, X} = F_{\mathrm{lat}/N/S/I}^{\mathrm{Alk}, \, X} \end{cases}$$

where  $F_{\text{lat}/N/S/I}^{\text{IC}}$  is the air-sea carbon flux from local/regional imbalance, and  $D_{\text{lat}/N/S/I}^{\text{IC}}$  as well as  $D_{\text{lat}/N/S/I}^{\text{IAlk}}$  are the associated disequilibria entailed for the global, without any guarantee that it fully occurs within the same region. Due to ocean circulation and the associated transport of carbon and Alk inventories, respectively (Fig. 3a). This comprehensive set of equations is essential to understanding the extent to which the local/regional carbon: Alk imbalance can drive the global air-sea carbon flux as well, as carbon and Alk disequilibria. In this context, these remain potential fluxes and potential disequilibria, which is why a prime is used in their notation to distinguish them from global scale fluxes (Eq. 9). and Alk, regional carbon: Alk

budget imbalances in riverine and burial fluxes explain the regional distribution of the drivers of the global air—sea carbon flux. However, they only partially explain the regional distribution of the flux itself.

# 2.1.3 Defining the inter-hemispheric flux gradient

# The inter-hemispheric flux gradient and transport

- Ocean—Understanding the spatial distribution of the pre-industrial riverine/burial-driven air-sea carbon flux is crucial for understanding the biases between observational and model-based estimates of the anthropogenic carbon sink. Yet, ocean circulation and carbon pumps within the ocean induce an asymmetry in the ocean on either side of the Intertropical Convergence Zone (ITCZ), which serves as an inter-hemispheric transport barrier. This asymmetry notably slows down the atmospheric earbon flux from the northern to the southern hemispheres (Murnane et al., 1999). (e.g. Murnane et al., 1999; Aumont et al., 2001; Resplane).
- 220 To assess the significance of this asymmetry on the air-sea carbon flux, particularly its components associated with riverine and burial fluxes, we provide two metrics for large-scale inter-hemispheric fluxes: (i) the inter-hemispheric air-sea carbon flux gradient (G), which is defined as the integrated net flux north of 20°N ( $F_N^{\rm C, air-sea}$ ) minus that south of 20°S ( $F_S^{\rm C, air-sea}$ ):

$$G = F_N^{C, \text{ air-sea}} - F_S^{C, \text{ air-sea}}$$

$$\tag{11}$$

and (ii) the inter-hemispheric ocean transport of carbon ( $T^{\rm C}$ ) and Alk ( $T^{\rm Alk}$ ), both directed northward, defined as the mean transport between 20°N ( $T_N^{\rm C/Alk}$ ) and 20°S ( $T_S^{\rm C/Alk}$ ):

$$T^{\text{C/Alk}} = \frac{1}{2} \cdot \left( T_N^{\text{C/Alk}} + T_S^{\text{C/Alk}} \right) \tag{12}$$

These two metrics rely on the subdivision of the ocean into two poleward basins, one south of 20°S and the other north of 20°N, separated by an intertropical basin (Fig. 3b and see Appendix C; e.g. Aumont et al., 2001; Resplandy et al., 2018).

In this context, total carbon and Alk regional fluxes can be written as follows:

230 
$$\begin{cases} F_{N/S/I}^{\text{C}} = F_{N/S/I}^{\text{C, air-sea}} + F_{N/S/I}^{\text{C, riv./bur.}} \\ F_{N/S/I}^{\text{Alk}} = F_{N/S/I}^{\text{Alk, riv./bur.}} \end{cases}$$

Specifically, by considering these fluxes  $(F_{N,S,I}^{\mathrm{C/Alk}})$  along with regional carbon and Alk disequilibria  $(D_{N,S,I}^{\mathrm{C/Alk}})$  and assuming an ocean at equilibrium (see (Fig. B1), we derive two expressions for the ocean transport of carbon and Alk through their respective budget closure equations  $(T_{N/S}^{\mathrm{C/Alk}})$ :

$$\left\{ \begin{array}{l} T_{N/S}^{\text{C/Alk}} + F_{\geq 20^{\circ}N/20^{\circ}S}^{\text{C/Alk}} + D_{\geq 20^{\circ}N/20^{\circ}S}^{\text{C/Alk}} = 0 \\ -T_{N/S}^{\text{C/Alk}} + F_{<20^{\circ}N/20^{\circ}S}^{\text{C/Alk}} + D_{<20^{\circ}N/20^{\circ}S}^{\text{C/Alk}} = 0 \end{array} \right.$$

Hence, we define the ocean transport of carbon and Alk as the average of its two expressions (Eq. D2; Fig. 3b):

$$T_{N/S}^{\text{C/Alk}} = \frac{1}{2} \cdot \left[ \left( F_{<20°N/20°S}^{\text{C/Alk}} + D_{<20°N/20°S}^{\text{C/Alk}} \right) - \left( F_{\geq20°N/20°S}^{\text{C/Alk}} + D_{\geq20°N/20°S}^{\text{C/Alk}} \right) \right]$$

In particular:

$$\left\{ \begin{array}{l} T_N^{\text{C/Alk}} = \frac{1}{2} \cdot \left[ \left( F_S^{\text{C/Alk}} + D_S^{\text{C/Alk}} + F_I^{\text{C/Alk}} + D_I^{\text{C/Alk}} \right) - \left( F_N^{\text{C/Alk}} + D_N^{\text{C/Alk}} \right) \right] \\ T_S^{\text{C/Alk}} = \frac{1}{2} \cdot \left[ \left( F_S^{\text{C/Alk}} + D_S^{\text{C/Alk}} \right) - \left( F_I^{\text{C/Alk}} + D_I^{\text{C/Alk}} + F_N^{\text{C/Alk}} + D_N^{\text{C/Alk}} \right) \right] \end{array} \right.$$

from which an expression of the inter-hemispheric transport of carbon and Alk (Eq. 12)can be derived:

$$240 \quad T^{\text{C/Alk}} = \frac{1}{2} \cdot \left[ \left( F_S^{\text{C/Alk}} + D_S^{\text{C/Alk}} \right) - \left( F_N^{\text{C/Alk}} + D_N^{\text{C/Alk}} \right) \right]$$

Subsequently, 3b and see Appendix C). A decomposition of the inter-hemispheric air-sea carbon flux gradient is equivalent to:

$$G = \underbrace{-2 \cdot T^{\text{C}}}_{\text{Transport component}} \underbrace{-\left(F_N^{\text{C, riv./bur.}} - F_S^{\text{C, riv./bur.}}\right) - \left(D_N^{\text{C}} - D_S^{\text{C}}\right)}_{\text{Riverine and burial component}}$$

At first glance, it may appear that this expression is exclusively formulated in terms of carbon, seemingly without any consideration of Alk. However, Alk plays a subtle yet integral role in this equation. Firstly, because  $T^C$  depends on both the southern and northern air-sea carbon fluxes (Eq. D5 and D1), and these regional fluxes are chemically driven by the relative imbalance between Alk and DIC. Secondly, the disequilibrium in the carbon content of the northern and southern oceans ( $D_N^C$  and  $D_S^C$ , respectively) is directly linked to the disequilibrium in Alk content (Eq.  $\ref{eq:content}$ ). Thus, the role of Alk is intricately interwoven within the formulation of G (Eq. D7). (G) into components associated with carbon transport and with riverine and burial processes is provided in Appendix D2.

### 2.2 Model and Simulations

250

255

260

#### 2.2.1 Model and configuration

As part of the NEMO (Nucleus for European Modelling of the Ocean) suite of models, we used here the marine biogeochemical model PISCES (Pelagic Interactions Scheme for Carbon and Ecosystem Studies) to refine our estimation of take a fresh look at the pre-industrial air-sea air-sea carbon flux. This refinement-involved a comprehensive consideration of both the carbon and Alk budgets, with a specific focus on external fluxes, notably CaCO<sub>3</sub> burial. While globally resembling PISCES-v2, as detailed in Aumont et al. (2015) and utilized in IPSL-CM6A-LR (Boucher et al., 2020), we introduced two key modifications in PISCES: (i) an adjustment to the N-fixation parameterization, following Bopp et al. (2022), and (ii) an adaptation of the burial fraction of CaCO<sub>3</sub> to maintain the balance the Alk budget and conserve the global Alk inventory without necessitating an Alk restoring scheme (see Planchat et al., 2023, their Appendix A2 for details). Our simulations were conducted offline using a tripolar ORCA (orthogonal curvilinear ocean mesh) grid with a nominal resolution of 2° and included 30 vertical levels. The ocean physics were derived from pre-industrial simulations of IPSL-CM5A-LR (Dufresne et al., 2013, based on NEMOv3.2), with a repeated 500-yr period, and a fixed and homogeneous atmospheric CO<sub>2</sub> concentration of 284 ppm at the ocean surface. To ensure model stability and attainment of a steady state (i.e. stable air-sea carbon flux; e.g. Orr et al., 2017, see Fig. B1), all

simulations presented below used the same initial conditions and have been run 2550 yr after an initial 500-yr spin-up using the

Table 2. Summary of the NEMO-PISCES sensitivity simulations with a short description (see Sect. B2.1 and Table B1 for more details).

Simulation	Description	Alk budget
std	Standard (riverine discharge, as well as OM and CaCO <sub>3</sub> burial simulated)	Balanced
norivbur	No external fluxes of carbon and Alk, except air-sea carbon fluxes	Balanced
rivref	Refractory organic riverine discharge	Balanced
rivorg	Fully organic riverine discharge	Balanced
rivinorg	Fully inorganic riverine discharge	Balanced
riv1p5	Riverine discharge of carbon and Alk multiplied by 1.5	Balanced
nosed-resto	No OM and CaCO <sub>3</sub> burial, but restoration of the Alk content	Balanced
nosed-diseq	No OM and CaCO <sub>3</sub> burial	Imbalanced
atlpac	Constrained balance of extra CaCO <sub>3</sub> burial/dissolution between the deep Atlantic/Pacific	Balanced
atlpac-diseq	Constrained imbalance of extra CaCO <sub>3</sub> burial/dissolution between the deep Atlantic/Pacific (-0.10 PgC yr-1)	Imbalanced
tropics-diseq	Constrained extra CaCO <sub>3</sub> burial in the shallow tropics (-0.10 PgC yr-1)	Imbalanced

standard configuration (Sect. 2.2.2). We calculated the carbon and Alk budgets related to their associated external sources/sinks using data from the last 50 yr of the simulations. The carbon and Alk inventory disequilibria deviations were estimated through linear regression over the same period.

#### 2.2.2 Standard simulation (std) and its riverine/burial component

280

The standard simulation (referred to as 'std'), based on the standard configuration described above, involves carbon and Alk riverine supply as well as organic matter OM and CaCO<sub>3</sub> burial. Riverine supply of carbon and Alk is based on output from the Global Erosion Model (GEM) of Ludwig et al. (1996) and considers both inorganic and organic carbon riverine discharge (0.37 and 0.14 PgC yr<sup>-1</sup>, respectively). Carbon and Alk are added at river mouths using a monthly climatology that is applied recursively. The inorganic fraction is supposed to be in the form of bicarbonate ionsand thus affects added as bicarbonate ions, thus affecting both DIC and Alk in a similar manner. The organic fraction is assumed to be fully labile and remineralizes instantaneously at the river mouth, thus impacting only DIC. This simulation also includes the burial of OM and CaCO<sub>3</sub> produced by pelagic organisms, which is are exported to the ocean interior and only partially remineralized or dissolved in the water column and at the seafloor (e.g. Planchat et al., 2023). These combined fluxes constitute the riverine and burial fluxes (Eq. 5 and 7), which, as introduced in Sect. 2.1.1, lead to the riverine/burial-driven air-sea carbon flux.

While To isolate the riverine/burial-driven component of the air-sea carbon flux, a simulation without riverine and burial fluxes was conducted (referred to as 'norivbur'), simulating only the component of the flux associated with the ocean carbon pumps. Indeed, while at the global scale, the net air-sea carbon flux directly corresponds to the riverine/burial-driven air-sea carbon flux (Eq. 2), at the local/regional scale, regional scale (N, S, or I, Fig. 3b), the air-sea carbon flux ( $F_{\rm nat}^{\rm C}$ ,  $F_{\rm nat}^{\rm c}$ ) can be decomposed into two components: one associated with the functioning of the ocean carbon pumps ( $F_{\rm pump}^{\rm C}$ ,  $F_{\rm nat}^{\rm c}$ ) and the other associated with the riverine and burial fluxes ( $F_{\rm riv}^{\rm C}$ ,  $F_{\rm riv}^{\rm c}$ ), which is our primary focus. Thus, for a given latitude (lat) with

zonally integrated values or for a specific ocean region (south: S, inter-tropics: I, north: N):

To isolate the riverine/burial-driven component, a simulation without riverine and burial fluxes was conducted (referred to as 'norivbur') which simulates only the component of the flux associated with the ocean carbon pumps. This Subsequently, by taking the difference between the std and norivbur simulations, this allows us to determine the riverine/burial-driven air-sea carbon flux, including its spatial distribution, by taking the difference between the std and norivbur simulations: of our standard configuration.

$$F^{\text{C, air-sea}} \underbrace{\text{riv./bur., lat/N/S/I}}_{\text{riv./bur., N/S/I}} \underbrace{\text{riv./bur., N/S/I}}_{\text{nat., lat/N/S/I}} = F^{\text{C, air-sea}} \underbrace{\text{nat., lat/N/S/I}}_{\text{nat., N/S/I}} (\text{std}) - F^{\text{C, air-sea}} \underbrace{\text{nat., lat/N/S/I}}_{\text{nat., N/S/I}} (\text{norivbur})$$
(14)

where the 'nat.' label was omitted since the simulations were conducted under pre-industrial conditions, and therefore, no anthropogenic component was included.

# 295 **2.2.3** Sensitivity simulations and global estimate

285

290

300

305

310

The set of sensitivity simulations considered covers a broad range of perturbations to the carbon and Alk riverine and burial fluxes. These simulations aim to assess the effects of different assumptions regarding these external fluxes on the riverine/burial-driven air-sea carbon flux (Table 2, Fig. 2b; see Appendix B2.1). Importantly, within the context of our study, the absolute values of the fluxes – whether they align with literature estimates or not – are not of primary concern. What matters are the relative differences between these values across simulations, which reflect the assumptions being tested.

First, we introduced variations in the magnitude and characteristics of riverine inputs, which, by riverine discharge to account for uncertainties in its magnitude and partly unresolved characteristics (e.g. labile/refractory, organic/inorganic partitioning). By closing the Alk budget, also these variations influenced CaCO<sub>3</sub> burial. In 'rivref', the OM riverine discharge was considered fully refractory (i.e. persisting on a time-scale-timescale longer than that of ocean circulation), in contrast to the lability assumption from labile assumption in the standard simulation. We explored fully organic and inorganic riverine discharges in 'rivorg' and 'rivinorg', respectively. Additionally, we, and also increased riverine discharge by a factor of 1.5 in 'riv1p5', while maintaining the same partitioning as std. Second, to assess the effect of a non-conserved Alk inventory or Alk restoration scheme, we disabled OM and CaCO<sub>3</sub> burial, artificially restoring Alk in 'nobur-resto', or assuming Alk-disequilibrium-a non-conserved Alk inventory in 'nobur-diseq'. Third, we introduced additional varied CaCO<sub>3</sub> burial to address uncertainties in its pre-industrial magnitude and spatial distribution. We added CaCO<sub>3</sub> burial/dissolution between the Atlantic and Pacific, maintaining an Alk equilibrium balancing the Alk budget in 'atlpac', or not in 'atlpac-diseq', and additional we also added CaCO<sub>3</sub> burial in the tropics, resulting in an Alk disequilibrium imbalanced Alk budget in 'tropics-diseq'. In all our sensitivity simulations, the '

We classify our simulations as either 'equilibrated' (suffix '-eq') or 'disequilibrated' (suffix '-diseq' suffix indicates an Alk disequilibrium, i. e. an increasing or decreasing global Alk inventory while maintaining a steady-state air-sea carbon flux. Furthermore, it-'), based on the conservation of global carbon and Alk inventories. In both cases, the air-sea carbon flux has reached a steady state. Equilibrated simulations are characterized by balanced global carbon and Alk budgets, resulting in conserved inventories over time. In contrast, disequilibrated simulations exhibit imbalanced budgets, leading to evolving global inventories, which are therefore not conserved. It is important to note that these variations only directly affected the variations applied in our set of sensitivity simulations directly affected only carbon and Alk, with nutrient fluxes left unaltered to avoid influencing fluxes, while nutrient fluxes were held constant in order to avoid perturbing OM and CaCO<sub>3</sub> production. Finally, we report that at the global scale, for the standard simulation,  $Q_{\rm inv} \simeq 0.797$  (Eq. 8), and this coefficient exhibits shows minimal variation across all sensitivity simulations considered (< 0.002 in absolute terms).

The theoretical framework introduced in this study (Sect. 2.1.1) is evaluated through our set of sensitivity simulations. It is then used directly to estimate the global magnitude of the pre-industrial riverine/burial-driven air-sea carbon flux and to investigate the global carbon and Alk inventory disequilibria (Eq. 10) from the existing carbon and Alk budgets, which include all oceanic external sources/sinks of carbon and Alk. We used the most recent carbon (Regnier et al., 2022) and Alk (Middelburg et al., 2020) budgets, although they are independent of each other and partly inconsistent (Table 3). For instance, the gap in the CaCO<sub>3</sub> burial (0.24 versus 0.35 PgC yr<sup>-1</sup>) would drive a 0.22 PgC yr<sup>-1</sup> difference in the Alk budget. We took great care to account for the uncertainties/extremes associated with the various external sources/sinks of carbon and Alk.

# 2.3 Composite simulated estimate and distribution

320

325

330

335

340

345

A practical framework was then developed, presented as an alternative method for estimating the distribution of the pre-industrial riverine/burial-driven air-sea carbon flux, specifically its inter-hemispheric partitioning. For each literature estimate of the various external sources/sinks of carbon and Alk, we constructed a skewed Gaussian distribution to match the median/mean value and the uncertainty/extreme range. To achieve this, we followed a two-step process. First, we created a triangular distribution based on the estimated median/mean value and the extremes (minimum and maximum) using Python's 'random.triangular' function from the *numpy* library. Then, we employed the 'stats.skewnorm.fit' function from the *scipy* library in Python to fit a skewed Gaussian probability density function (PDF) to this triangular distribution. This approach ensured that we maintained the integrity of the extreme and median/mean values obtained from the literature while working with continuous PDFs.

To derive the distribution of the pre-industrial riverine/burial-driven air-sea carbon flux, we constructed a composite simulated estimate by linearly combining our sensitivity simulations. This process aimed to align the riverine and burial fluxes of the composite simulated estimate with literature estimates (Middelburg et al., 2020; Regnier et al., 2022) and involved four steps (see Fig. E2, and Table 3). We began with the riverine/burial-driven air-sea carbon flux from the standard simulation (extracted from std minus norivbur) in the first step. In the second step, our objective was to match the riverine discharge and OM burial of carbon in the composite simulated estimate with the literature estimate, achieved by using the simulation where the riverine discharge was multiplied by 1.5 (extracted from riv1p5 minus std). The third step focused on matching the riverine discharge and OM burial of Alk, using the simulation where the riverine discharge was entirely inorganic (extracted from rivinorg minus

std), ensuring no impact on the previously matched values of the riverine discharge and OM burial of carbon. Finally, in the fourth step, we aimed to match the CaCO<sub>3</sub> burial of Alk by using the simulation with an additional CaCO<sub>3</sub> burial/dissolution with an Alk disequilibrium (extracted from atlpac-diseq minus std), without affecting the previously matched values of the riverine discharge and OM burial of carbon and Alk. Given the intrinsic link between CaCO<sub>3</sub> burial effect on Alk and DIC with a 2:1 ratio, Step 4 should also enable to match the CaCO<sub>3</sub> burial of carbon. However, due to the inconsistency between the two most recent budgets for carbon and Alk (Table 3), an extra step was required, equivalent to Step 3, but only considering the CaCO<sub>3</sub> burial of carbon in excess. In summary, this composite simulated estimate, built on a linear combination of our sensitivity simulations constrained by external carbon and Alk fluxes from the literature, provides an alternative view of the distribution of the pre-industrial riverine/burial-driven air-sea carbon flux.

#### 3 Results

350

355

360

375

#### 4 Results and discussion

# 3.1 Pre-industrial air-sea carbon flux and its riverine/burial-driven component

In the pre-industrial era, the simulated air-sea carbon flux, derived from the standard simulation (std), remains stable at  $-0.27~\mathrm{PgC}~\mathrm{yr}^{-1}$  (see Fig. B3a), indicating a net global ocean outgassing. However, the distribution of the surface air-sea carbon flux exhibits considerable heterogeneity among different regions, primarily driven by ocean circulation patterns (Fig. 4a). Regions characterized by carbon-rich deep-water upwellings, such as equatorial and southern ocean upwelling zones, tend to show carbon outgassing. Conversely, poleward heat transport within the ocean, exemplified by western boundary currents like the Gulf Stream, promotes carbon absorption as surface waters cool. Consequently, the outcome is a pronounced meridional air-sea carbon flux gradient, with ingassing in the northern hemisphere (+0.57 PgC yr<sup>-1</sup>), outgassing in the intertropical zone (-0.91 PgC yr<sup>-1</sup>), and minimal outgassing in the southern hemisphere (-0.06 PgC yr<sup>-1</sup>), primarily due to the impact of southern ocean upwelling between 45-65°S (Fig. 4b,c). The inter-hemispheric air-sea carbon flux gradient (*G*; Sect. 2.1.3) is +0.51 PgC yr<sup>-1</sup>, while the inter-hemispheric transport of carbon and Alk ( $T^{\rm C}$  and  $T^{\rm Alk}$ ; Sect. 2.1.3) amounts to  $-0.35~\mathrm{PgC}~\mathrm{yr}^{-1}$  and  $-0.07~\mathrm{PgC}~\mathrm{yr}^{-1}$ , respectively (see Fig. B3a).

The air-sea carbon flux can be subsequently decomposed into a component associated with the functioning of the ocean carbon pumps and a component associated with riverine and burial fluxes (Sect. 2.2.2). More specifically, we use the simulation without riverine and burial fluxes (norivbur) is used to isolate the distribution of air-sea carbon fluxes associated with the internal functioning of the ocean carbon pumps. Indeed, regional air-sea carbon fluxes are primarily influenced by these pumps, which establish and sustain vertical and horizontal carbon gradients within the ocean (e.g. Sarmiento and Gruber, 2006; Murnane et al., 1999; Aumont et al., 2001; Resplandy et al., 2018). Thus, both the physical pump (involving ocean circulation and air-sea carbon exchange) and the biological pump (comprising processes like production, export, and the remineralization/dissolution of OM and CaCO<sub>3</sub>) play pivotal roles in elucidating the overall distribution of the air-sea carbon flux. These air-sea carbon fluxes exhibit significant ingassing in the northern hemisphere (+0.67 PgC yr<sup>-1</sup>) and outgassing in the inter-tropical

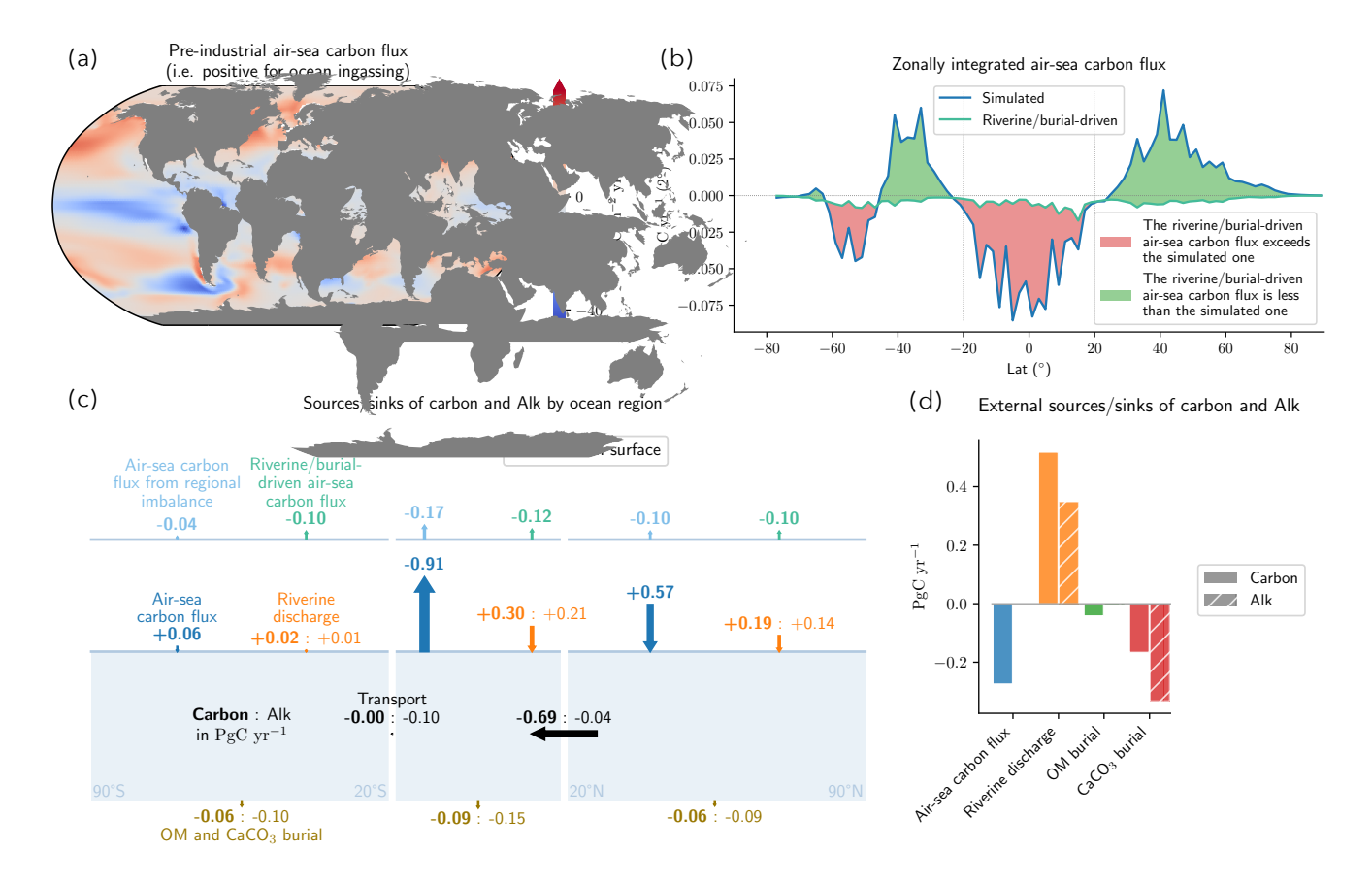


Figure 4. Description of the standard NEMO-PISCES simulation (std; see Fig. B2 for additional elements). (a) Map of the pre-industrial air-sea carbon flux, where positive values indicate ocean ingassing. (b) Zonally The zonally integrated air-sea carbon flux (dark blue), derived from local imbalance (light blue), and the riverine/burial-driven component air-sea carbon flux (aquamarine). When the local imbalance riverine/burial-driven flux exceeds (is less than) the simulated air-sea carbon fluxone, the area in between is shaded in red (green). (c) Partitioning of the riverine (orange) and burial (dark gold) fluxes by ocean region (southern, inter-tropical, and northern). The fluxes, in petagrams of carbon per year (PgC yr¹) for carbon (in bold) and Alk (in normal font), are directed by arrows, with orientation indicating the sign, and size reflecting the absolute magnitude of the flux. The regional partitioning of the riverine/burial-driven air-sea carbon flux stemming (aquamarine) and of the potential air-sea carbon flux from regional carbon: Alk budget imbalances and riverine/burial-driven fluxes is (light blue) are also provided above. (d) Partitioning of the integrated external sources and sinks of carbon (shaded) and Alk (hatched). The negative impact of OM burial on Alk is attributed to the release of ammonium when OM is remineralized at the seafloor rather than buried. Detailed descriptions of (c) and (d) can be found in Supplementary S1 and S2.

zone (-0.79 PgC yr<sup>-1</sup>), with minimal ingassing in the southern hemisphere (+0.16 PgC yr<sup>-1</sup>; see Table B1). Overall, the air-sea carbon flux associated with the oceanic carbon pumps is expected to be net-zero when integrated at the global scale, although norivbur shows a small residual component (+0.05 PgC yr<sup>-1</sup>; see Fig.B3a). This residual component is attributed to a residual carbon budget imbalance due to internal ocean processes (see Appendix B0.3).

Finally, by taking the difference between our standard simulation and the simulation without riverine and burial fluxes (std minus norivbur), we isolate the component of interest, i.e. that induced by riverine and burial fluxes (Sect. 2.2.2). This riverine/burial-driven air-sea carbon flux results in a net global outgassing of 0.31 PgC yr<sup>-1</sup>, distributed among the northern, inter-tropical, and southern regions as follows: 0.10, 0.12, and 0.10 PgC vr<sup>-1</sup> (Fig. 4c).

# 3.2 The global riverine/burial-driven air-sea carbon flux

#### 3.2.1 Role of sediment burial fluxes

395

400

405

410

At global scale, Accounting for the riverine carbon flux input alone in the standard simulation (+0.52 PgC yr<sup>-1</sup>) is insufficient to fully account for the explain the simulated air-sea carbon outgassing (0.27 PgC yr<sup>-1</sup>)alone (Fig. 4d and 5a). Indeed, it is necessary to consider carbon fluxesassociated with OM. Burial-associated carbon fluxes, from both OM (-0.17 PgC yr<sup>-1</sup>) and CaCO<sub>3</sub> burial (amounting to -0.17 and (-0.04 PgC yr<sup>-1</sup>, respectively; Fig. 2d and see Fig. B3a), which lessen the air-sea carbon act to partially offset this input, thereby reducing the net outgassing to 0.31 PgC yr<sup>-1</sup>.

The importance of burial fluxes in driving the riverine/burial-driven air-sea carbon flux is furthermore exemplified by our set of sensitivity simulations (Fig. 5a,b). Increasing the river-riverine input by a factor of 1.5, while maintaining its partitioning (riv1p5), drives results in an increase in carbon outgassing by of 0.17 PgC yr<sup>-1</sup>, which is only partly consistent with. This is less than the increase in riverine carbon discharge (+0.26 PgC yr<sup>-1</sup>; see Fig. B3b). This discrepancy arises because a portion), as part of this additional carbon (0.09 PgC yr<sup>-1</sup>) of the additional carbon is sequestered in the form of is buried as CaCO<sub>3</sub> to maintain equilibrium in the global Alk inventory. Similarly, considering that riverine discharge consists exclusively of either organic or a balanced Alk budget (see Fig. B3b). Similarly, a change in the partitioning of the riverine input between organic and inorganic forms (rivorg and rivinorg), the does not alter the total magnitude of the river carbon input remains unaffected. However, riverine carbon input compared to the standard configuration, but it does affect the air-sea carbon ougassing is impacted (reaching outgassing. It reaches 0.47 and 0.20 PgC yr<sup>-1</sup>, respectively; (see Table B1), primarily due to as the associated decrease (increase—0.38 PgC yr<sup>-1</sup>) or increase (+0.14 PgC yr<sup>-1</sup>) in the Alk riverine riverine Alk discharge relative to std (—0.38 and +0.14 PgC yr<sup>-1</sup>, respectively; see Fig. B3b), which is accompanied by a corresponding reduction (increase) leads to corresponding changes in CaCO<sub>3</sub> earbon burial relative to std burial (+0.19 and -0.07 PgC yr<sup>-1</sup>, respectively). This underscores the significance of considering to maintain a balanced Alk budget. This highlights the pivotal role of CaCO<sub>3</sub> burial when constructing the ocean carbon budget, especially when evaluating the net in shaping the air-sea carbon flux.

The total carbon outgassing obtained from a simple carbon budgetonly holds however for our simulations in which the global Alk inventory is in equilibrium under the assumption of a balanced Alk budget, where riverine Alk inputs are offset by CaCO<sub>3</sub> burial (Fig. 5b; Sect. 2.1.1), balancing the Alk input from rivers with the burial of CaCO<sub>3</sub> 4d).

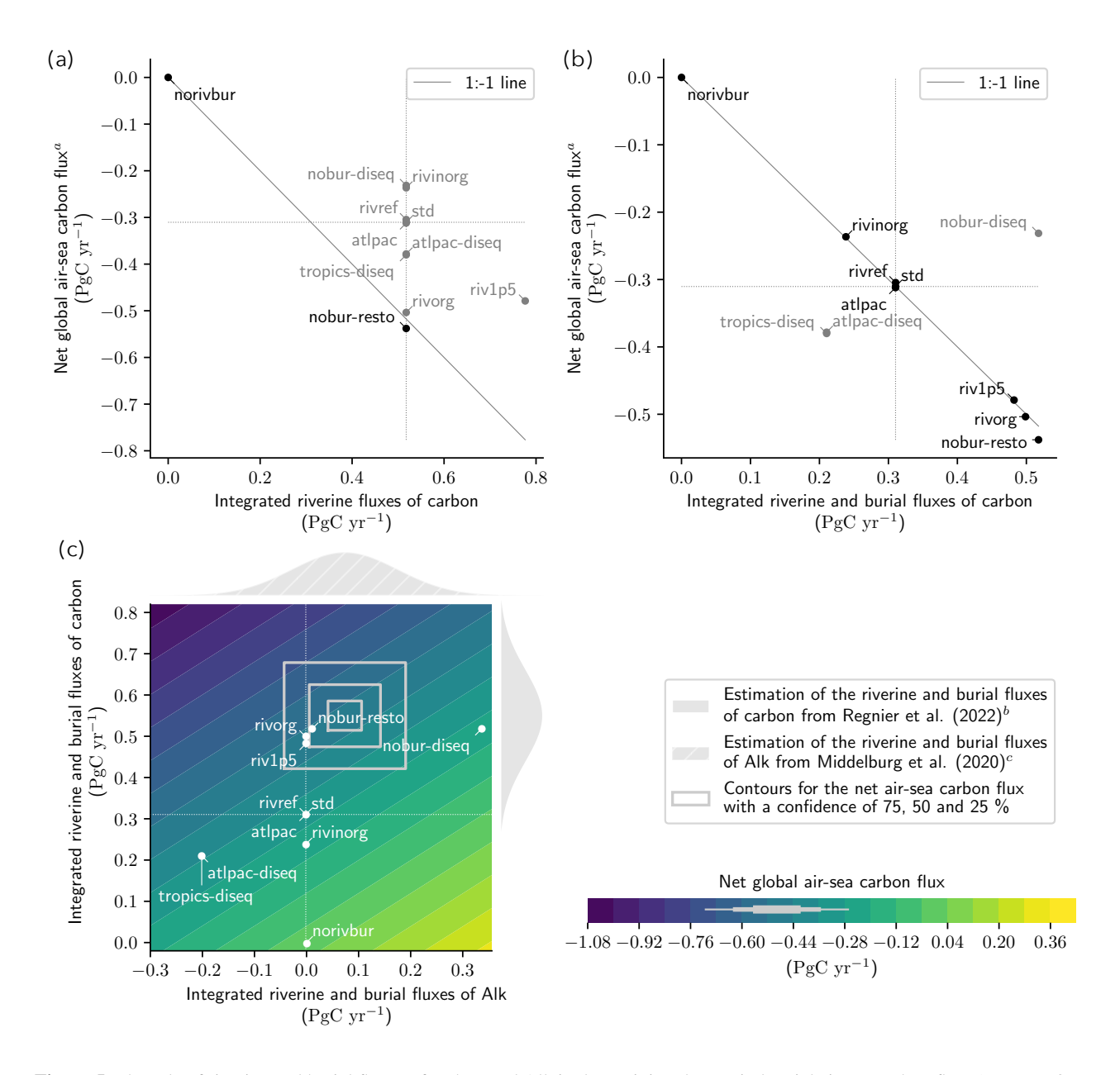


Figure 5. The role of riverine and burial fluxes of carbon and Alk in determining the pre-industrial air-sea carbon flux. (continued)

Figure 5. (continued). (a, b) Comparison between the net global air-sea carbon flux and (a) the integrated riverine fluxes of carbon, or (b) the integrated riverine and burial fluxes of carbon. When the net air-sea carbon flux balances the considered external fluxes (on the 1:1 line), simulation names are indicated in black. This applies to (a) simulations that do not account for burial and maintain conserve the global Alk inventory at equilibrium (norivbur and nobur-resto), and (b) all simulations maintaining conserving the global Alk inventory at equilibrium (excluding nobur-diseq, atlpac-diseq, and tropics-diseq). (c) Theoretical framework that accounts for Alk and carbon budgets to reconstruct the net air-sea carbon flux. The net air-sea carbon flux (filled contours) is determined by multiplying the integrated riverine and burial fluxes of Alk (x-axis) by  $Q_{inv}$  and then subtracting the integrated riverine and burial fluxes of carbon (y-axis). The deviation of the net air-sea carbon flux from this relationship in the NEMO-PISCES sensitivity simulations is small (less than 0.01 PgC yr<sup>-1</sup> for all, except nobur-resto: less than 0.03 PgC yr<sup>-1</sup>). Simulations with a conserved global Alk inventory at equilibrium—align with the zero x-axis line. The most recent carbon and Alk budgets (Table 3) provide estimates of riverine and burial fluxes of carbon b and Alkc, as shown at the top and on the right in grey. The net air-sea carbon flux reconstructed from these flux estimates are indicated as grey rectangles, with confidence intervals at 75 %, 50 %, and 25 %, and projected on the color bar.

However, such a carbon budget – which deduces the pre-industrial air-sea carbon flux from riverine and burial fluxes of carbon – is only valid under the condition of a balanced Alk budget (Fig. 4d5b). When the global Alk inventory is not in equilibrium this assumption does not hold, it becomes necessary to consider the Alk budget in addition to the carbon budget to account for both the carbon and Alk budgets to correctly assess the riverine/burial-driven air-sea carbon flux (Sect. 2.1.1).

# 3.2.2 Impact of an imbalanced alkalinity budget

The possibility of an alkalinity budget not being in equilibrium imbalanced Alk budget during the pre-industrial era has been hypothesized several times in multiple times over the past three decades (e.g. Milliman, 1993; Middelburg et al., 2020; Cartapanis et al., 2018; Boudreau et al., 2018). If this is the case, such a disequilibrium would have implications on the pre-industrial air-sea carbon flux (Methods). Two of our sensitivity simulations enable assessment of The simulations atlpac-diseq and tropics-diseq allow us to assess the implications of such a deviation in the global Alk inventory disequilibrium. First, in atlpac-diseq, we introduced additional (Table 2; see also Table B1), by controlling both the magnitude and spatial distribution of CaCO<sub>3</sub> burial in the deep Atlantic to better represent what is known from actual reconstructions of sediment types. Second, in tropics-diseq, we increased a way that better reflects current paleoceanographic reconstructions (e.g. Cartapanis et al., 2018). Both simulations implement an imbalanced Alk budget (-0.10 PgC yr<sup>-1</sup>) via additional CaCO<sub>3</sub> burialin the either in the deep Atlantic (atlpac-diseq) or in the shallow tropics to account for accumulation by coral reefs (tropics-diseq; Cartapanis et al., 2018).

In both simulations, the additional CaCO<sub>3</sub> burial drives additional carbon outgassing when compared to the std simulation.

This may appear counter-intuitive when relying on represent coral reef processes (tropics-diseq). They lead to the same increase in steady-state air-sea carbon outgassing relative to std (+0.07 PgC yr<sup>-1</sup>). This outcome may seem counterintuitive when

<sup>&</sup>lt;sup>a</sup>The net air-sea carbon flux of the NEMO-PISCES sensitivity simulations was adjusted for their respective residual carbon budget imbalances (see Appendix B0.3).

<sup>&</sup>lt;sup>b</sup>This distribution also includes fluxes from groundwater discharge.

<sup>&</sup>lt;sup>c</sup>This distribution also includes fluxes from anaerobic processes, groundwater discharge, and reverse weathering.

applying a simple carbon budget, since these two simulations prescribed additional both simulations prescribe extra carbon removal from the ocean (to the sediment) and resulted sediments), yet result in enhanced carbon loss at the air-sea interface to the atmosphere (Fig. 5b). The extra CaCO<sub>3</sub> burial not only acts as an additional carbon sink for the ocean relative to std (0.10 PgC yr<sup>-1</sup>; see Fig. B3b) but, due to the induced carbon:Alk imbalance (Sect. 2.1.2), it also leads to an increased carbon outgassing at equilibrium by 0.07 PgC yr<sup>-1</sup> in both simulations relative to std. As a result, the disequilibrium in In fact, the associated outgassing leads to a net decrease in the global ocean carbon inventory relative to std (-0.16 PgC yr<sup>-1</sup>) is even greater in absolute term than the extra, which exceeds, in absolute terms, the additional CaCO<sub>3</sub> burial (0.10 PgC yr<sup>-1</sup>), due to the associated outgassing (; see Fig. B3b).

When the global Alk inventory is in disequilibrium, the

435

440

455

460

# 3.2.3 Validating the governing equation of the pre-industrial riverine/burial-driven air-sea carbon flux

Importantly, even with an imbalanced Alk budget that drives deviations in the global carbon and Alk inventories, the ocean can maintain a steady-state air-sea carbon flux is no longer solely determined by the riverine and burial fluxes of carbon but also by the carbon:Alk imbalance induced by these fluxes relative to the equilibrium ratio with the atmospheric  $CO_2$  concentration  $(Q_{inv}; Sect. 2.1.2)$ . In such cases, the (Fig. B1). Overall, the theoretical framework introduced in Sect. 2.1.1 is fully validated by our set of sensitivity simulations. At pre-industrial steady state, the net air-sea carbon flux  $(F^{C, air-sea})$  can be expressed as the product of the integrated riverine and burial fluxes of Alk Alk flux  $(F^{Alk})$  multiplied by  $Q_{inv}$ , minus the integrated riverine and burial fluxes of carbon carbon flux  $(F^{C, bur./riv.})$ :

$$F^{\text{C, air-sea}} = \underbrace{Q_{\text{inv}} \cdot F^{\text{Alk}}}_{D^{\text{C}}} - F^{\text{C, bur./riv.}}, \tag{15}$$

where  $D^{C}$  and  $D^{Alk}$  represent the global carbon and Alk inventory disequilibria. This underscores the significance of the global Alk inventory in estimating the deviations, respectively. This formulation highlights the critical role of pre-industrial air-sea carbon flux and, consequently, the importance of assumptions made regarding Alk equilibrium.

Specifically, we emphasize that with a global Alk inventory disequilibrium, the ocean can maintain an equilibrium with the atmospheric  $CO_2$  concentration, resulting in a nearly constant air-sea carbon flux (Fig. B1) but a global carbon inventory disequilibrium (Fig. 5b). When the global Alk inventory is in equilibrium ( $F^{Alk} = 0$ ), a direct relationship between the riverine and burial fluxes of carbon and the net air-sea carbon flux becomes evident ( $F^{C, air-sea} = -F^{C, bur./riv.}$ ).

# 3.2.4 A new estimate of the global riverine/burial-driven air-sea carbon flux

Literature-based estimates of riverine/burial fluxes of carbon and Alk, from the most recent carbon and Alk budgets (Sect. 4.2.1 and see Fig. E3), including the calculation of the corresponding air-sea carbon flux, as well as carbon and Alk content disequilibria. The values are presented in petagrams of carbon per year. Values in brackets represent the uncertainty or extreme range, while the bold value indicates the best estimate or average. The intervals are arranged with the smallest absolute value

first, except when both positive and negative values are present in the range. Type of Carbon flux Alk flux Associated air-sea Associated DIC Associated Alk sources/sinks (from Regnier et al., 2022) (from Middelburg et al., 2020) earbon flux disequilibrium disequilibrium  $(Q_{\text{inv}} \cdot F^{\text{Alk}} - F^{\text{C}})(Q_{\text{inv}} \cdot F^{\text{Alk}})(F^{\text{Alk}})$  Riverine discharge a = 0.650; 1.1500.578; 0.929-0.189; -0.4100.461; 0.7400.578, 0.9290.900 0.756 -0.297 0.603 0.756 OM burial a = 0.059; -0.1550.014; 0.0370.070; 0.1840.011; 0.0290.014; 0.037-0.107 0.024 0.126 0.019 0.024 CaCO3 burial a = 0.141; a = 0.345-0.648; a = 0.828-0.315; a = 0.375-0.516; a = 0.660-0.648; a = 0.828-0.243-0.708-0.321-0.564-0.708 Total a = 0.450; a = 0.650-0.056; a = 0.138-0.340; a = 0.695-0.045; a = 0.110-0.056; a = 0.1380.550 a = 0.072 a = 0.072

Using the theoretical framework introduced in this manuscript and literature-based estimates of riverine/burial fluxes of carbon and Alk, based on the most recent carbon and Alk budgets, we derive, from Eq. 15, a Alk budget assumptions – as well as the persistent uncertainties and unknowns – in estimating the pre-industrial riverine/burial-driven air-sea carbon fluxestimate of –0.49 [–0.34; –0.70] PgC yr<sup>-1</sup> (Table 3 and Fig. 5c). This pre-industrial riverine/burial-driven air-sea carbon flux is associated to carbon and Alk inventory disequilibria of 0.06 [–0.05; 0.11] PgC yr<sup>-1</sup> and 0.07 [–0.06; 0.14] PgC yr<sup>-1</sup> for carbon and 0.07 [–0.06; 0.14] PgC yr<sup>-1</sup> for Carbon and 0.07 [–0.06; 0.14] PgC yr<sup>-1</sup> for Alk.

This estimate of -0.49 [-0.34; -0.70] PgC yr<sup>-1</sup> represents a downward revision of the latest riverine/burial-driven air-sea earbon flux estimate of  $-0.65 \pm 0.30$  PgC yr<sup>-1</sup> currently used in the GCB (Friedlingstein et al., 2024) and based on an in-depth review of the land-to-ocean continuum of the global carbon cycle Regnier et al. (2022). Utilizing our value to estimate anthropogenic earbon uptake in the ocean from pCO<sub>2</sub>-based estimates would reduce the overall discrepancy between these observation-based estimates and model values by 0.16 PgC yr<sup>-1</sup> over the entire period considered, thereby mitigating the current offset (Friedlingstein et al., 2025).

.

480

485

490

465

The discrepancy between our reassessment of riverine/burial-driven outgassing and the value currently used in the GCB underscores the crucial importance of clearly defining ocean boundary conditions and the pressing need to develop a combined and consistent earbon and Alk budget for the ocean to achieve a robust estimate. Part of this discrepancy arises because atmospheric carbon uptake by continental shelves (0.10 PgC yr<sup>-1</sup> Regnier et al., 2022) is fully integrated into our net pre-industrial riverine/burial-driven air-sea carbon flux as we also consider OM and CaCO<sub>3</sub> burial in these regions, reducing this flux by 0.10 PgC yr<sup>-1</sup>. The remaining reduction of 0.06 PgC yr<sup>-1</sup> is linked to a slight imbalance in the global Alk inventory (0.07 PgC yr<sup>-1</sup> Middelburg et al., 2020). However, the current inconsistency between the independently developed carbon and Alk budgets makes our estimate unreliable. If the burial flux of CaCO for carbon (Middelburg et al., 2020) is aligned with that for Alk (+0.22 PgC yr<sup>-1</sup>; Table 3), the outgassing would decrease by an additional 0.18 PgC yr<sup>-1</sup>. Conversely, if the burial flux of CaCO<sub>3</sub> for Alk (Middelburg et al., 2020) is aligned with that for carbon (-0.11 PgC yr<sup>-1</sup>; Table 3), the outgassing would also drop, in this case by 0.11 PgC yr<sup>-1</sup>, further reducing the current offset (Friedlingstein et al., 2024). Thus, it is essential to establish a combined and consistent carbon and Alk budget to confidently reassess this pre-industrial outgassing within the theoretical framework presented here.

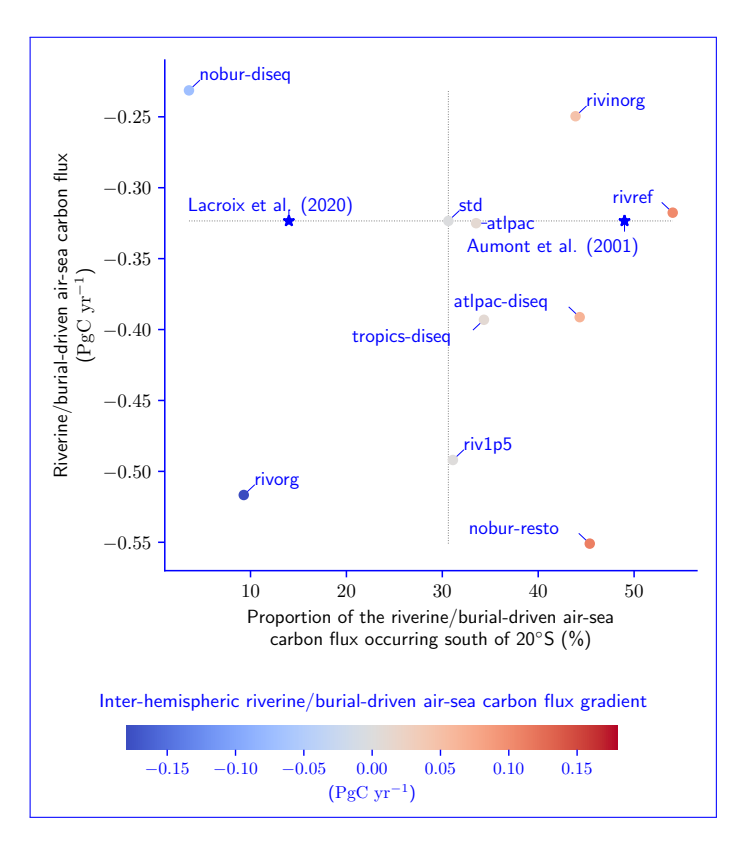


**Figure 6.** Distribution Spatial distribution of the riverine/burial-driven air-sea carbon flux and its key drivers. (a) Comparison between the riverine/burial-driven air-sea carbon flux (y-axis, PgC yr<sup>-1</sup>), the fraction of this flux occurring south of 20°S (x-axis, %) and its interhemispheric gradient (color dots, PgC yr<sup>-1</sup>). The fraction of this flux occurring south of 20°S is also shown for Aumont et al. (2001) and Lacroix et al. (2020) (black stars), assuming the same riverine/burial-driven air-sea carbon flux as our standard simulation (std). (b) Inter-hemispheric gradient of the riverine/burial-driven air-sea carbon flux (filled contours) and its two components, from carbon:Alk imbalances (Sect. 2.1.2 and 2.1.3). One component (x-axis) is associated with the inter-hemispheric gradient of air-sea carbon flux driven by northern and southern carbon:Alk imbalances (and inventory disequilibria), while the other component (y-axis) corresponds to the inter-hemispheric gradient of air-sea carbon flux associated to the inter-hemispheric transport of the carbon:Alk imbalance (Eq. D7 and see Fig. D1). The deviation in the simulated inter-hemispheric gradient in NEMO-PISCES sensitivity simulations as compared to the reconstructed ones using the two components is minimal (< 0.01 PgC yr<sup>-1</sup>, not shown).

#### 495 3.3 The regional spatial distribution of the riverine/burial-driven air-sea carbon flux

#### 3.3.1 A highly contrasting Contrasting regional distribution fluxes

The inter-hemispheric gradient of the pre-industrial air-sea carbon flux is primarily controlled by ocean interior processes and the functioning of the ocean carbon pumps. Specifically, in an ocean without any riverine and burial carbon fluxes (norivbur), the inter-hemispheric gradient amounts to +0.51 PgC yr<sup>-1</sup> (see Fig. B3a). The biological pump contributes to carbon uptake

in the northern hemisphere through surface biological activity and leads to carbon release in the southern hemisphere due to the upwelling of carbon-rich deep waters, as documented in previous studies (e.g. Murnane et al., 1999; Aumont et al., 2001; Resplandy et al., 2018). When subtracting the gradient estimated from simulation norivbur to all other sensitivity simulations, we find that only a fraction of the inter-hemispheric air-sea carbon flux gradient is accounted for by riverine and burial fluxes (ranging from -0.18 to +0.11 PgC yr<sup>-1</sup> in our set of sensitivity simulations).

Our set of sensitivity simulations, exploring different assumptions on which explore various assumptions about riverine and burial fluxes, encompass the uncertainty range of associated with the inter-hemispheric gradient of the riverine/burial-driven air-sea carbon flux (Fig. 6a). The main point of contention around the inter-hemispheric regarding this gradient lies in the fraction of this the flux occurring in the southern hemisphere, where most of the discrepancy in estimating the largest discrepancies in estimates of the anthropogenic carbon flux sink between pCO<sub>2</sub>-based and model estimates existed methods and model simulations were located in GCBs (from 2018 to 2022; e.g. Hauck et al., 2020; Friedlingstein et al., 2022b)prior to being mostly transferred, before being mostly shifted to the inter-tropical region (since 2023; e.g. Friedlingstein et al., 2023, 2024). In our simulations, the fraction of the flux occurring in the southern hemisphere ranges from less than 5 % (nobur-diseq) to more than 50 % (rivref). By comparison, it was estimated at 49 % (Aumont et al., 2001) and then revised to 14 % (Lacroix et al., 2020) in the GCBs (TableYY—1 and Fig.7a 6), and even as low as 4 % in the literature (Jacobson et al., 2007). This is intriguing because particularly intriguing, as one might expect that this distribution is primarily influenced this distribution to be primarily governed by the strength of the meridional overturning circulation – and its effect on the southward transport of net-role in transporting riverine/burial-carbon burial-derived carbon southward – , but yet our sensitivity simulations, with unchanged despite identical ocean dynamics, reveal highly contrasting distributions.

# 3.3.2 Influencing factors

505

510

515

530

There is no direct correlation between the magnitude of the riverine/burial-driven air-sea carbon flux and the proportion of this flux occurring south of 20°S (Fig. 6a). Notably, the substantial uncertainty on the refractory nature of organic riverine discharge (e.g., Aumont et al., 2001; Gruber et al., 2009) (e.g. Aumont et al., 2001; Gruber et al., 2009) is demonstrated to result in a significant shift in the proportion of the riverine/burial-driven air-sea carbon flux occurring in the southern ocean (54 % in rivref vs. 31 % in std; Fig.6a), even though the total flux remains nearly the same. Conversely, when the riverine discharge is increased by 50 % (riv1p5), the distribution of the riverine/burial-driven air-sea carbon flux remains unchanged compared to std, while the total outgassing increases from 0.32 PgC yr<sup>-1</sup> (std) to 0.49 PgC yr<sup>-1</sup> (riv1p5; see Table B1).

The decoupling between the magnitude of the net riverine/burial-driven air-sea carbon flux and its inter-hemispheric gradient is primarily linked to the distribution, both horizontally and vertically, of the carbon:Alk budget imbalance resulting from riverine and burial fluxes –(Sect. 2.1.2). When an excess of CaCO<sub>3</sub> burial is considered at the bottom of the Atlantic (primarily in the northern hemisphere; atlpac-diseq), the resulting impact of the carbon:Alk budget imbalance on the riverine/burial-driven air-sea carbon flux occurs remotely, in the southern hemisphere, due to the meridional overturning circulation. This results in a relative outgassing compared to std  $(-0.07 \text{ PgC yr}^{-1})$ , and an increase in the inter-hemispheric riverine/burial-driven air-sea carbon flux gradient  $(+0.07 \text{ PgC yr}^{-1})$ ; see Fig. B3b). On the contrary, when the surplus of CaCO<sub>3</sub> burial is in the shallow

tropics (tropics-diseq), the riverine/burial-driven air-sea carbon flux anomaly compared to std is equivalent to the one reported for atlpac-diseq, but the inter-hemispheric gradient is this time nearly not impacted relative to std (+0.01 PgC yr<sup>-1</sup>) since the flux anomaly is concentrated in the shallow tropics, primarily affecting the local regional air-sea carbon flux. Similarly, flux anomalies resulting from carbon:Alk budget imbalances with respect to the riverine fluxes tend to manifest locally, regionally (i.e. primarily in the northern hemisphere): (i) a fully organic riverine discharge (rivorg) leads to a relative outgassing compared to std (-0.19 PgC yr<sup>-1</sup>), aligned with a decrease in the inter-hemispheric gradient (-0.18 PgC yr<sup>-1</sup>); and (ii) a fully inorganic riverine discharge (rivinorg) leads to a relative ingassing compared to std (+0.07 PgC yr<sup>-1</sup>), aligned with an increase in the inter-hemispheric gradient (+0.05 PgC yr<sup>-1</sup>; see Fig. B3b).

Nevertheless, it is crucial to have access to both the value of the

- 4 Proof-of-concept applications and discussions
- 4.1 The global flux

# 545 **4.1.1 Approach**

535

540

550

555

560

The theoretical framework introduced in this study (Sect. 2.1.1) has been validated by our set of sensitivity simulations (Sect. 3.2). It is therefore now possible to estimate the global magnitude of the pre-industrial riverine/burial-driven air-sea carbon flux and its spatial distribution to properly estimate the magnitude and distribution of the oceanic anthropogenic carbon uptake (e.g. Hauck et al., 2020; Friedlingstein et al., 2022b, 2024). It is possible to decompose the inter-hemispheric gradient of the riverineto investigate the associated global carbon and Alk inventory deviations (Eq. 10) based on existing carbon and Alk budgets, which encompass all external oceanic sources and sinks of carbon and Alk. For consistency with the literature, we rely on the most recent carbon (Regnier et al., 2022) and Alk (Middelburg et al., 2020) budgets, even though they were derived independently and are partly inconsistent (Table 3). We carefully accounted for the uncertainties and extreme values associated with the various external sources/burial-driven air-sea flux into a component associated with the inter-hemispheric transport of a carbon :Alk imbalance and a component associated with a carbon :Alk imbalance stemming from riverine and burial fluxes (including inventory disequilibria; Fig. 6b, sinks of carbon and Alk (Table 3).

# 4.1.2 Findings

Using the theoretical framework introduced in this manuscript and literature-based estimates of riverine/burial fluxes of carbon and Alk, based on the most recent carbon and Alk budgets, we derive, from Eq.  $\overline{D7}$ , 15, a pre-industrial riverine/burial-driven air-sea carbon flux estimate of -0.49 [-0.34; -0.70] PgC yr $^{-1}$  (Table 3 and Fig. E15c). This demonstrates that when considering riverineand burial fluxes (std relative to norivbur), the component associated with these external fluxes (-0.07) pre-industrial riverine/burial-driven air-sea carbon flux is associated with global carbon and Alk inventory deviations of 0.06 [-0.05; 0.11] PgC yr $^{-1}$  ) is offset by the transport-related component (+0.07) and 0.07 [-0.06; 0.14] PgC yr $^{-1}$ , respectively (see Fig. E1). This estimate is based on an integrated external flux of 0.55 [0.45; 0.65] PgC yr $^{-1}$  for carbon and 0.07 [-0.06; 0.14] PgC yr $^{-1}$  for Alk.

**Table 3.** Literature-based estimates of riverine/burial fluxes of carbon and Alk, from the most recent carbon and Alk budgets (Sect. 4.2.1 and see Fig. E3), including the calculation of the corresponding air-sea carbon flux, as well as carbon and Alk content deviations. The values are presented in petagrams of carbon per year. Values in brackets represent the uncertainty or extreme range, while the bold value indicates the best estimate or average. The intervals are arranged with the smallest absolute value first, except when both positive and negative values are present in the range.

Type of sources/sinks	Carbon flux (from Regnier et al., 2022)	Alk flux (from Middelburg et al., 2020)	Associated air-sea carbon flux	Associated DIC deviation	Associated Alk deviation
			$(Q_{\text{inv}} \cdot F^{\text{Alk}} - F^{\text{C}})$	$(Q_{\mathrm{inv}} \cdot F^{\mathrm{Alk}})$	$(F^{\text{Alk}})$
Riverine discharge <sup>a</sup>	[0.650; 1.150]	[0.578; 0.929]	[-0.189; -0.410]	[0.461; 0.740]	[0.578, 0.929]
	0.900	0.756	-0.297	0.603	0.756
$\mathbf{OM}$ burial $^b$	[-0.059; -0.155]	[0.014; 0.037]	[0.070; 0.184]	[0.011; 0.029]	[0.014; 0.037]
	-0.107	0.024	0.126	0.019	0.024
CaCO <sub>3</sub> burial	[-0.141; -0.345]	[-0.648; -0.828]	[-0.315; -0.375]	[-0.516; -0.660]	[-0.648; -0.828]
	-0.243	-0.708	-0.321	-0.564	-0.708
Total	[0.450; 0.650]	[-0.056; 0.138]	[-0.340; -0.695]	[-0.045; 0.110]	[-0.056; 0.138]
	0.550	0.072	-0.493	0.057	0.072

<sup>&</sup>lt;sup>a</sup>Including fluxes from groundwater discharge and anaerobic processes.

#### 4.1.3 Discussion

565

570

575

580

This new estimation of the pre-industrial riverine/burial-driven air-sea carbon flux represents a downward revision of the latest value of  $-0.65 \pm 0.30 \, \text{PgC yr}^{-1}$ ), resulting in a null inter-hemispheric currently adopted in the GCB (Friedlingstein et al., 2024), which was derived from a comprehensive assessment of the global land-to-ocean carbon continuum Regnier et al. (2022). Applying our revised estimate in the calculation of the anthropogenic carbon uptake based on  $p\text{CO}_2$ -based methods would reduce the overall discrepancy between observation-based and model-derived oceanic carbon uptake estimates by 0.16 PgC yr $^{-1}$  over the historical period, thus alleviating a portion of the present offset (Fig. 1; Friedlingstein et al., 2024).

The discrepancy between our reassessment of the riverine/burial-driven air-sea carbon flux gradient for std (Fig. 5b and Fig. 6b). In the case of a surplus of outgassing and the value currently used in the GCB underscores the crucial importance of clearly defining ocean boundary conditions and the pressing need to develop a combined and consistent carbon and Alk budget for the ocean to achieve a robust estimate. Part of this discrepancy arises because atmospheric carbon uptake by continental shelves (0.10 PgC yr<sup>-1</sup>; Regnier et al., 2022) is fully integrated into our net pre-industrial riverine/burial-driven air-sea carbon flux as we also consider OM and CaCO<sub>3</sub> burial in these regions, reducing this flux by 0.10 PgC yr<sup>-1</sup>.

The current inconsistencies between the independently developed carbon and Alk budgets make our estimate less robust and highlight the need for a combined revision of both. Beyond the 0.10 PgC yr<sup>-1</sup> reduction in outgassing due to differing ocean boundary definitions relative to GCB, the remaining 0.06 PgC yr<sup>-1</sup> decrease in our new estimate is linked to a slight imbalance in the Alk budget (+0.07 PgC yr<sup>-1</sup> Middelburg et al., 2020). However, the discrepancy in CaCO<sub>3</sub> burial in the deep

<sup>&</sup>lt;sup>b</sup>Including fluxes from reverse weathering.

Atlantic (atlpac-diseq), the increase in the inter-hemispheric riverine estimates between the most recent carbon and Alk budgets (Regnier et al., 2022; Middelburg et al., 2020) would translate into a 0.22 PgC yr<sup>-1</sup> difference in the Alk budget (Table 3). If the carbon flux associated with CaCO<sub>3</sub> burial were aligned with the Alk budget from Middelburg et al. (2020), the outgassing would decrease by an additional 0.18 PgC yr<sup>-1</sup>. Conversely, aligning the Alk flux associated with CaCO<sub>3</sub> burial with the carbon value from Regnier et al. (2022) would reduce the outgassing by 0.11 PgC yr<sup>-1</sup>. Thus, reconciling CaCO<sub>3</sub> burial fluxes in both carbon and Alk budgets is expected to further reduce the current outgassing offset (Friedlingstein et al., 2024). Establishing a combined and internally consistent carbon and Alk budget is therefore essential to confidently reassess the pre-industrial outgassing within the theoretical framework presented here.

# 4.2 The flux distribution

# 4.2.1 Approach

585

590

595

600

605

610

The set of sensitivity simulations conducted to validate our theoretical framework spans a wide range of assumptions regarding riverine and burial fluxes of carbon and Alk, thereby providing all the necessary tools to reassess the spatial distribution of the riverine/burial-driven air-sea carbon fluxgradient relative to std (+0.07 PgC yr<sup>-1</sup>; see Fig. B3b)is primarily attributed to the transport of a carbon:Alkimbalance (Fig. 6b). Conversely, when the As in our global estimate (Sect. 4.1), this reassessment strategy is grounded in the most recent global budgets of carbon and Alk. By logically combining specific sensitivity simulations, we construct a composite simulation that aligns with these global budgets and allows us to re-evaluate the distribution of the riverine/burial-driven pre-industrial air-sea carbon flux.

First, for each literature-based estimate of the external sources and sinks of carbon and Alk, we constructed a skewed Gaussian probability density function (PDF) that captures the median/mean value and the reported uncertainty range. This was achieved in two steps for each literature estimate of the various external sources/sinks of carbon and Alk. A triangular distribution was first generated using the estimated central value and minimum/maximum bounds via the 'random.triangular' function from the Python library *numpy*. This triangular distribution was then fitted with a skewed normal PDF using the 'stats.skewnorm.fit' function from the *scipy* library. This approach allowed us to preserve the essential characteristics of the literature values (median/mean and extremes) while working with continuous distributions.

Second, we constructed a composite simulation that isolates the effect of riverine and burial fluxes on the air-sea carbon flux (i.e. excluding the influence of internal carbon pumps). This was achieved by linearly combining a subset of our sensitivity simulations. Throughout the remainder of the manuscript, we refer to the composite simulated estimate as the pre-industrial riverinedischarge is entirely organic (rivorg), it is mostly the external flux component that causes the decrease in the inter-hemispheric /burial-driven air-sea carbon flux derived from this combined simulation. The following four-step workflow is designed to ensure that the riverine and burial fluxes in the composite simulation are consistent with the latest literature estimates (Middelburg et al., 202

Step 1: We initialized our composite simulation by isolating the effect of riverine and burial fluxes on the air-sea carbon fluxgradient relative to std (-0.18 PgC yr<sup>-1</sup>; see Fig. B3b and Fig. 6b), and the same outcome occurs when the riverine

- discharge is entirely inorganic (rivinorg). This emphasizes that the spatial distribution of the carbon: Alk imbalance stemming from external fluxes, in conjunction with oceanic transport, plays a significant role in shaping the, removing the contribution of internal carbon pumps. This was done by subtracting the norivbur simulation from the standard simulation ('std'-'norivbur').
- Step 2: Next, we adjusted the carbon fluxes associated with riverine discharge and OM burial to match literature estimates. This was achieved by weighting the simulation where riverine inputs were increased by a factor of 1.5 ('riv1p5'-'std'), as the overall riverine flux amplitude was the first variable that needed to be tuned. At the end of this stage, the composite simulated estimate was a linear combination of 'std'-'norivbur' and 'riv1p5'-'std'.
  - Step 3: We then adjust the Alk fluxes associated with riverine discharge and OM burial to match literature estimates. This was achieved by weighting the simulation where all riverine discharge was considered inorganic ('rivinorg'-'std'), which did not alter the carbon values already matched in Step 2. The composite simulated estimate became a linear combination of the result from Step 2 and 'rivinorg'-'std'.

625

630

635

- Step 4: Finally, we ensured that Alk fluxes associated with CaCO<sub>3</sub> burial also matched the literature estimate. This was done using the simulation with enhanced CaCO<sub>3</sub> burial/dissolution and a global Alk imbalance ('atlpac-diseq'-'std'), without affecting the fluxes adjusted in previous steps. Given the 2:1 stoichiometric ratio between Alk and DIC in CaCO<sub>3</sub> processes, this step simultaneously ensured consistency for both the carbon and Alk components of CaCO<sub>3</sub> burial. The final composite estimate was a linear combination of the result from Step 3 and 'atlpac-diseq'-'std'.
- Extra step (correction): Due to inconsistencies between the most recent carbon and Alk budgets specifically in the CaCO<sub>3</sub> burial flux (Table 3) an additional correction step was required. This correction, applied similarly to Step 3, again uses 'rivinorg'-'std' to consider an increased carbon sink via CaCO<sub>3</sub> burial, while maintaining Alk balance. This adjustment targets only the excess CaCO<sub>3</sub> burial of carbon needed to reconcile our composite simulation with the carbon budget from Regnier et al. (2022). Note that this step would not be necessary if the carbon and Alk budgets were internally consistent.

In summary, this composite simulated estimate, built as a weighted linear combination of targeted sensitivity simulations and constrained by the latest literature estimates of riverine and burial fluxes, provides a spatially explicit representation of the pre-industrial inter-hemispheric riverine/burial-driven air-sea carbon fluxgradient. By design, the integrated value of this flux in the composite simulation is consistent with that obtained by applying the theoretical framework to the most recent carbon and Alk budgets from the literature (Sect. 4.1).

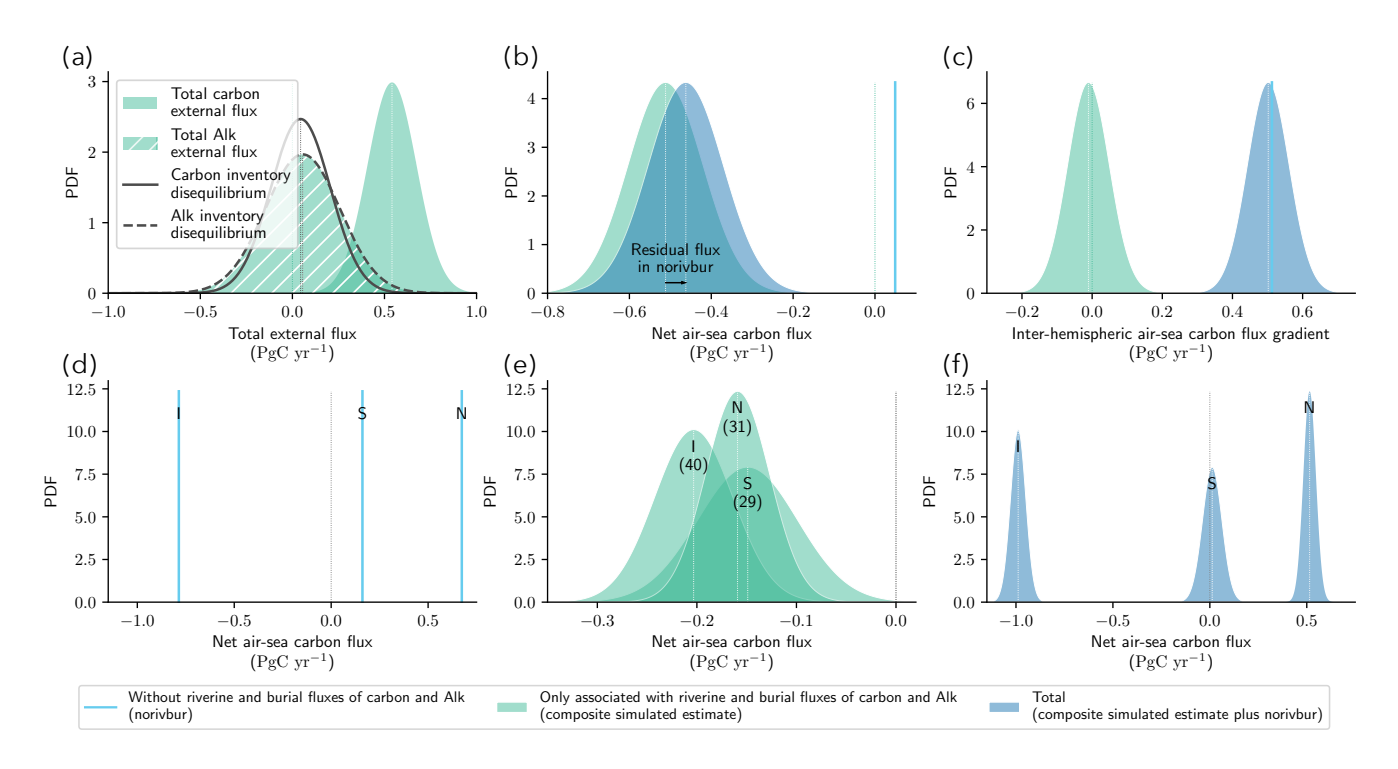


Figure 7. Description of the composite simulated estimate resulting from a linear combination of the NEMO-PISCES sensitivity simulations and literature-based estimates of riverine/burial fluxes of carbon and Alk (Sect. 4.2.1 and see Fig. E3). (a) PDF illustrating the total riverine and burial fluxes of carbon (shaded) and Alk (hatched) in the composite simulated estimate, along with the associated PDF for the resulting disequilibrium-deviation in carbon (solid) and Alk (dashed) content. (b,c) PDFs of the net air-sea carbon flux and the inter-hemispheric air-sea carbon flux gradient. Within each of these sub-panels, the PDF associated with no riverine and burial fluxes of carbon and Alk (norivbur; cyan line) is juxtaposed with the one corresponding to only riverine and burial fluxes of carbon and Alk (composite simulated estimate minus norivbur; aquamarine) to obtain the total value (composite simulated estimate; dark blue). Further details on the residual component where no riverine and burial fluxes are considered are explained in Appendix. B0.3. (d, e, f) The associated spatial distribution for the southern, inter-tropical, and northern regions: (d) without riverine and burial fluxes of carbon; (e) exclusively related to riverine and burial fluxes of carbon and Alk; and (f) the overall distribution. In (e), the percentage of each component is provided in brackets.

# 4.2.2 A new estimate of the regional distribution of the riverine/burial-driven air-sea flux

# 4.2.2 Findings

The construction of a composite simulated estimate resulting from a linear combination of the NEMO-PISCES our sensitivity simulations to align with the literature-based estimates for integrated fluxes of carbon and Alk budgets (Fig. 7a; Sect. 4.2.1 and see Fig. E3) enables an estimation a reassessment of the distribution of this riverine/burial-driven air-sea carbon outgassing  $(0.15\pm0.13, 0.20\pm0.10, \text{ and } 0.16\pm0.08 \text{ PgC yr}^{-1}$  for the southern, inter-tropical, and northern regions, respectively; Fig. 7e). The uncertainty associated with these values is primarily linked to the uncertainties/extremes in literature-based estimates (see Fig. E1). Such a distribution implies that 29 % of the outgassing occurs in the southern region, 40 % in the inter-tropical region, and 31 % in the northern region. This represents

### 4.2.3 Discussion

660

665

670

675

The distribution we found corresponds to an intermediate distribution compared to those used adopted in the GCB over time, with recent values at falling between the most recent estimate of 14 %, 64 %, and 22 % (Lacroix et al., 2020), and historical values at the earlier estimate of 49 %, 25 %, and 26 % (Aumont et al., 2001, Table 1). This would partially confirm the reduction in the discrepancy between  $pCO_2$ -based and model estimates in the southern region, while avoiding the introduction of a bias in the inter-tropical region, as it was noted in GCB 2023, (Friedlingstein et al., 2023) compared to previous GCBs (e.g. Friedlingstein et al., 2022b).

Furthermore, by By summing the fluxes from the composite simulated estimate and the simulation without riverine and burial fluxes (norivbur), we obtain the total inter-hemispheric air-sea carbon flux gradient , which can be obtained. Notably, this amounts to  $0.50 \pm 0.15$  PgC yr<sup>-1</sup> (Fig. 7c). Notably, this value, which aligns with the inter-hemispheric CO<sub>2</sub> concentration gradient in the atmosphere between the South Pole and Mauna Loa during the pre-industrial era, which . It was historically assessed at +0.82 ppm (Keeling et al., 1989) and more recently reevaluated at  $+0.55 \pm 0.15$  ppm (Resplandy et al., 2018) through interpolation of atmospheric CO<sub>2</sub> concentration measurements.

A more comprehensive characterization of riverine and burial fluxes of carbon and Alk remains a critical challenge for accurately constraining the spatial distribution of the riverine/burial-driven air—sea carbon flux. This is particularly true for the fate of terrestrial organic carbon and its associated lability, which remains highly uncertain (Aumont et al., 2001; Jacobson et al., 2007; Gru . Nevertheless, the approach proposed in this study is flexible and can accommodate future revisions of these external fluxes. Fundamentally, the selection of sensitivity simulations used to construct the composite simulation (Sect. 4.2.1; see also Fig. E2) can be revisited as scientific understanding progresses or as model representations evolve. For instance, in NEMO-PISCES, burial tends to occur predominantly near coastal margins. To counterbalance this biased feature in the composite simulation, we selected the sensitivity simulation with extra CaCO<sub>3</sub> burial in the deep Atlantic basin (atlpac-diseq), rather than the one with increased burial in the shallow tropics (tropics-diseq).

The use of sensitivity simulations to build a composite simulation underscores the method's potential for reassessing the distribution of the pre-industrial air–sea carbon flux. By drawing from a set of pre-existing simulations and grounding

the reassessment in the theoretical framework developed in this study, the spatial pattern of the flux can be revised in a consistent and coherent manner, without the need for additional model runs. This approach is particularly well suited for model intercomparison exercises, as it allows for efficient re-evaluation of regional fluxes and contributes to reducing biases linked to differences in ocean circulation or biogeochemical parameterizations across models.

#### 5 Conclusion and perspectives

680

685

690

695

700

705

The theoretical framework introduced here provides a novel We have offered a fresh perspective on the pre-industrial air-sea earbon flux through the lens of the air-sea carbon flux by leveraging the ocean alkalinity budget. Sensitivity The theoretical framework we introduced, validated through sensitivity simulations conducted with NEMO-PISCESunderscore the utility and robustness of this framework in quantifying, demonstrates both its robustness and practical relevance for assessing the riverine/burial-driven pre-industrial air-sea earbon flux using external carbon and alkalinity flux estimates. Specifically, based on the most recent literature-based estimates of carbon and alkalinity budgets (Regnier et al., 2022; Middelburg et al., 2020), we reassessed the pre-industrial outgassing flux associated with riverine and burial fluxes to be 0.49 [0.34;0.70] PgC yr<sup>-1</sup>. This value is notably lower than the current estimate used in the GCB(0.65 ± 0.30 PgC yr<sup>-1</sup> Friedlingstein et al., 2024). Importantly, this revised estimate reduces the discrepancy air-sea carbon flux in the context of the GCB.

Through two proof-of-concept applications, we demonstrate the potential of this theoretical framework to identify biases between observation-based and model-derived estimates of the anthropogenic ocean carbon sink by 0.16 PgC yr<sup>-1</sup>. However, the revised flux estimate does not correct for any temporally varying biases (e.g. Hauck et al., 2023).

Additionally, oceanic carbon sink at both global and regional scales, and to partially correct persistent offsets. In the first application, we revisit the global magnitude of the framework demonstrated its flexibility in integrating potential revisions of pre-industrial external carbon and alkalinity fluxes, as well as to consider changes in external fluxes resulting from human activities' impact, including both riverineand burial fluxes (e.g., Regnier et al., 2022). This adaptability is crucial, given the major uncertainties surrounding the pre-industrial alkalinity budget (e.g. Cartapanis et al., 2018) and the inconsistencies between current combined riverine/burial-driven air—sea carbon flux using existing carbon and alkalinity budgets. This yields a simple and rapid method for reassessment whenever these budgets are revised. In the second application, we propose a method to reassess the spatial distribution of the pre-industrial riverine/burial-driven air—sea carbon flux. This is achieved by constructing a composite simulation, based on a linear combination of sensitivity simulations, that aligns with both carbon and alkalinity budgets, which highlight an urgent need for a comprehensive review. Finally, the framework also emphasized the critical importance of precisely defining the boundary conditions of the oceanic domain. This approach is particularly well-suited for model intercomparison exercises, as it enables efficient reassessment of regional fluxes while helping to mitigate biases related to ocean physics or biogeochemical parameterizations.

These flexible applications now call for four key efforts from the community regarding the pre-industrial riverine/burial-driven air—sea carbon flux:

(i) To reduce uncertainty in its global magnitude:

- Clarify the definition of ocean domain boundaries at the coastal interface, within the land-to-ocean continuum, where
  multiple processes intersect (e.g. riverine discharge, and part of OM and CaCO<sub>3</sub> burial; Regnier et al., 2022; Gruber et al., 2023)
  -fluxes intersect (riverine discharge, and part of organic matter and CaCO<sub>3</sub> burial).
  - Establish a combined and internally consistent carbon and alkalinity budget, as current independently developed estimates remain inconsistent (e.g. CaCO<sub>3</sub> burial).

A practical framework was developed to estimate the distribution of the pre-industrial riverine /burial-driven air-sea carbon flux.Constructed as a linear combination of sensitivity simulations, this framework aligns with literature-based estimates of external carbon and alkalinity fluxes (Regnier et al., 2022; Middelburg et al., 2020). The reassessed distribution is 29 % in the southern region, 40 % in the inter-tropical region, and 31 % in the northern region, which is an intermediate distribution compared tothose used in the GCB over time, with recent values at 14 %, 64 %, and 22 % (Lacroix et al., 2020), and historical values at 49 %, 25 %, and 26 % (Aumont et al., 2001).

- 720 (ii) To reduce uncertainty in its regional distribution:
  - Improve our understanding of the intrinsic properties of riverine and burial fluxes (e.g. the fate of terrestrial organic matter).
  - Promote intermodel comparison efforts to identify systematic biases and improve robustness across modeling approaches.

As ocean circulation likely plays a pivotal role in partitioning these fluxes, applying this framework within a Global Ocean Biogeochemistry Model (GOBM) intercomparison exercise holds promise for better constraining the spatial distribution of this pre-industrial outgassing flux and enhancing confidence in the shared and adopted values in the GCB. Additionally, a better understanding of the intrinsic properties of these external fluxes is needed, such as whether the organic carbon brought by rivers is refractory or not (Aumont et al., 2001; Jacobson et al., 2007; Gruber et al., 2009). A more comprehensive characterization of external carbon and alkalinity fluxes remains a critical challenge for accurately constraining the magnitude and distribution of the riverine/burial-driven air-sea carbon flux.

# Appendix A: Methods

715

### **Appendix A: Theoretical framework**

As a complement to the theoretical framework introduced in Sect. 2.1.1, we outline here how to derive  $Q_{inv}$ , the inverse of the 'isocapnic quotient' approximation introduced by Humphreys et al. (2018). Specifically, we develop the method proposed by Planchat et al. (2023), and subsequently demonstrate its full consistency with the approach employed by Humphreys et al. (2018)

For a fixed salinity (S) and temperature (T),  $pCO_2$  – the partial pressure of  $CO_2$  in seawater – can be differentiated as follows:

740 
$$dpCO_2 = \frac{\partial pCO_2}{\partial Alk} \bigg|_{DIC,S,T} \cdot dAlk + \frac{\partial pCO_2}{\partial DIC} \bigg|_{Alk,S,T} \cdot dDIC$$
 (A1)

Assuming  $pCO_2$  is fixed – for instance, at equilibrium with atmospheric  $CO_2$  – leads to:

$$\frac{\text{dDIC}}{\text{dAlk}}\bigg|_{p\text{CO}_2, S, T} = -\frac{\partial p\text{CO}_2}{\partial \text{Alk}}\bigg|_{\text{DIC}, p\text{CO}_2, S, T} \cdot \frac{\partial \text{DIC}}{\partial p\text{CO}_2}\bigg|_{\text{Alk}, p\text{CO}_2, S, T}$$
(A2)

Yet,  $pCO_2$  is defined by:

$$pCO_2 = \frac{K_2}{K_0 \cdot K_1} \cdot \frac{\left[HCO_3^-\right]^2}{\left[CO_3^{2-}\right]} \tag{A3}$$

where  $K_0$ ,  $K_1$  and  $K_2$  are the stoichiometric equilibrium/dissociation constants of the  $CO_2$  system (e.g. Sarmiento and Gruber, 2006)

We then introduce the simplifying assumption:

$$\begin{cases} [HCO_3^-] \simeq 2DIC - Alk \\ [CO_3^{2-}] \simeq Alk - DIC \end{cases}$$
(A4)

This assumption is reasonable given that  $[HCO_3^-]^2$  and  $[CO_3^{2-}]$  together typically account for over 99 % of DIC and over 97 % of Alk (Sarmiento and Gruber, 2006; Humphreys et al., 2018). Under this assumption, Eq. A3 can be approximated as:

$$pCO_2 \simeq \frac{K_2}{K_0 \cdot K_1} \cdot \frac{(2DIC - Alk)^2}{Alk - DIC}$$
(A5)

Accordingly, the partial derivatives of  $pCO_2$  with respect to Alk and DIC at constant  $pCO_2$ , S, and T become:

$$\begin{cases}
\frac{\partial p \text{CO}_2}{\partial \text{Alk}} \Big|_{\text{DIC}, p \text{CO}_2, S, T} \simeq \frac{K_2}{K_0 \cdot K_1} \cdot \frac{(3\text{Alk} - 2\text{DIC}) \cdot (2\text{DIC} - \text{Alk})}{(\text{Alk} - \text{DIC})^2} \\
\frac{\partial p \text{CO}_2}{\partial \text{DIC}} \Big|_{\text{Alk}, p \text{CO}_2, S, T} \simeq \frac{K_2}{K_0 \cdot K_1} \cdot \frac{-\text{Alk} \cdot (2\text{DIC} - \text{Alk})}{(\text{Alk} - \text{DIC})^2}
\end{cases}$$
(A6)

Substituting these expressions into Eq. A2 gives:

755 
$$\left. \frac{\text{dDIC}}{\text{dAlk}} \right|_{p \in O_2, S, T} = \frac{1}{Q} = Q_{\text{inv}} \simeq \frac{\text{Alk}}{3\text{Alk} - 2\text{DIC}}$$
 (A7)

It is worth noting that the same expression can also be derived following the method presented in Humphreys et al. (2018, their Appendix . Using the same approximation as in Eq. A4, they arrive at the following form for Alk (see their Eq. C.6):

$$Alk \simeq 2DIC + \frac{\beta}{2} - \sqrt{\frac{\beta^2}{4} + \beta DIC}$$
(A8)

with:

760 
$$\beta = \frac{(2\text{DIC} - \text{Alk})^2}{(\text{Alk} - \text{DIC})} = p\text{CO}_2 \cdot \frac{K_0 \cdot K_1}{K_2}$$
(A9)

Differentiating Alk with respect to DIC at constant  $pCO_2$ , S, and T then yields:

$$\frac{\mathrm{dAlk}}{\mathrm{dDIC}}\bigg|_{p\mathrm{CO}_2, S, T} \simeq 2 - \frac{\beta}{2 \cdot \sqrt{\frac{\beta^2}{4} + \beta \mathrm{DIC}}} = 2 - \frac{1}{\sqrt{1 - \frac{4\mathrm{DIC}}{\beta}}}$$
(A10)

After rearrangement, this leads to the same expression for  $Q_{\text{inv}}$ :

$$\frac{\mathrm{dAlk}}{\mathrm{dDIC}}\bigg|_{p \in \mathcal{O}_2, S, T} = Q = \frac{1}{Q_{\mathrm{inv}}} \simeq \frac{3\mathrm{Alk} - 2\mathrm{DIC}}{\mathrm{Alk}}$$
(A11)

An exact formulation of Q is also provided by Humphreys et al. (2018, their Appendix D).

# **Appendix B: Model and simulations**

#### B1 CMIP6 ESMs, and GCB GOBMs, and associated air-sea carbon fluxes

We present an evaluation of the representation of the pre-industrial air-sea carbon flux in ESMs and GOBMS that participated in the CMIP6 exercise (Eyring et al., 2016) and the 2024 GCB exercise (Friedlingstein et al., 2024). This assessment offers valuable insights into the current state of the art regarding the modeling of this flux in the models utilized for intercomparison studies. To ensure comparability, we regridded the CMIP6 data to a regular 1°x1° grid using the distance-weighted average remapping method 'remapdis' provided by the Climate Data Operator (CDO). This step was taken as because the data available from the 2024 GCB (Hauck et al., 2022) were already on a regular 1°x1° grid. However, it is important to note that this regridding process introduced a minor error in the integrated air-sea carbon flux values.

We assessed 15 CMIP6 ESMs from 12 different climate modelling centers (Eyring et al., 2016): CanESM5 (r1i1p2f1) and CanESM5-CanOE (r1i1p2f1) from CCCma, with two distinct marine biogeochemical models; CMCC-ESM2 (r1i1p1f1) from CMCC; CNRM-ESM2-1 (r1i1p1f2) from CNRM-CERFACS; ACCESS-ESM1-5 (r1i1p1f1) from CSIRO; IPSL-CM6A-LR

(r1i1p1f1) from IPSL; MIROC-ES2L (r1i1p1f2) from MIROC; UKESM1-0-LL (r1i1p1f2) from MOHC; MPI-ESM1-2-LR (r1i1p1f1) and MPI-ESM1-2-HR (r1i1p1f1) from MPI-M, with two different resolutions; MRI-ESM2-0 (r1i2p1f1) from MRI, CESM2-WACCM (r1i1p1f1) from NCAR; NorESM2-LM (r1i1p1f1) from NCC; GFDL-CM4 (r1i1p1f1) and GFDL-ESM4 (r1i1p1f1) from NOAA-GFDL, with two distinct marine biogeochemical models. Only the air-sea CO<sub>2</sub> flux (positive donward, 'fgCO<sub>2</sub>' in kgC m<sup>-2</sup> s<sup>-1</sup>) of the pre-industrial control simulations was considered, from 1850 to 2100, and yearly averaged. Each ESM was weighted in the calculation of the CMIP6 mean, such that each modelling group has the same total contribution. We also assessed the 10 GOBMs used in the 2024 GCB exercise (Friedlingstein et al., 2024): NEMO3.6-PISCESv2-gas (CNRM), NEMO4.2-PISCES (IPSL), MPIOM-HAMOCC6, MRI-ESM2-3, ACCESS, MICOM-HAMOCC (NorESM-OC), MOM6-COBALT (Princeton), FESOM-2.1-REcoM3, NEMO-PlanckTOM12 and CESM-ETHZ). Once again, only the air-sea CO<sub>2</sub> flux (positive donward, 'fgCO<sub>2</sub>' in mol m<sup>-2</sup> s<sup>-1</sup>) of the control simulations (i.e. constant atmospheric CO<sub>2</sub>, no climate change and variability) was considered, from 1959 to 2023, and yearly averaged. We found that the drift in the ESMs and GOBMs in the net air-sea carbon flux was consistently less than 0.10 PgC (100 yr)<sup>-1</sup>, and as such, it had negligible impact on the related results (see Fig. 2a and D3a).

# **B2** NEMO-PISCES sensitivity simulation configurations simulations

# **B2.1 Configurations**

780

785

790

800

805

We provide here additional details regarding the various configurations of the sensitivity simulations conducted using NEMO-PISCES (Table B1). In the standard configuration, the slight deviation (-0.02 PgC yr<sup>-1</sup>) between Alk riverine discharge (+0.35 PgC yr<sup>-1</sup>) and inorganic carbon riverine discharge (+0.37 PgC yr<sup>-1</sup>) arises from the supply of inorganic nitrogen by rivers, presumed to be in the form of nitrate, which has a negative impact on Alk (Fig. B3). It is worth noting that the latitudinal distribution of riverine inputs is based on Ludwig et al. (1996) and may undergo revision in the future, particularly following Li et al. (2017), although the human imprint on these fluxes cannot be removed. Lastly, we emphasize that we did not evaluate the implications of partitioning riverine inputs between inorganic and organic components on biological production, and consequently, its effects on the air-sea carbon flux, as we only altered DIC and Alk in the various configurations. Finally, we accounted for atmospheric deposition in our sensitivity simulations, since atmospheric nitrogen deposition is considered a nitrate source, which impacts Alk. This has however a negligible effect, as does the dilution effect (see Supplementary S2).

The manuscript has been crafted to be accessible and comprehensible for both observationalists and modelers. However, the disequilibria deviations mentioned for the carbon and Alk inventories manifest themselves in model outputs in the form of drifts. Furthermore, all the sensitivity simulations conducted also address modeling issues. In particular, a case that can be encountered in marine biogeochemistry models, both historically and even today, is the consideration, or lack thereof, of the OM and CaCO<sub>3</sub> burial, and the consequences this can have on the carbon flux, depending on whether the global Alk inventory is equilibrated conserved through a global-scale Alk restoration scheme, or left in disequilibrium deviating (nosed-resto, nosed-diseq; Planchat et al., 2023). Finally, the choice of the different configurations, and their resulting impact on the air-sea carbon flux, also serve as a reminder of the importance of carefully considering the global Alk inventory in models, and controlling its

potential disequilibrium deviation/drift according to desired hypotheses (e.g. global Alk inventory equilibrium a balanced Alk budget or not).

From a practical standpoint, in NEMO-PISCES, CaCO<sub>3</sub> burial predominantly occurs in coastal areas (Fig. B1a), with limited differentiation in burial at depth between the Atlantic (less acidic) and Pacific (more acidic) regions (Sarmiento and Gruber, 2006; Cartapanis et al., 2018; Ridgwell and Zeebe, 2005, Fig. B1a). To address this limitation, we introduced the configuration 'atlpac-diseqatlpac' wherein we constrain extra CaCO<sub>3</sub> burial in the deep Atlantic while simulating extra CaCO<sub>3</sub> dissolution in the deep Pacific. This adjustment aims to enhance the representation of CaCO<sub>3</sub> burial while maintaining a balanced Alk budget (i.e. conserving the global Alk inventory equilibrium (; Fig. B1b). Additionally, considering the possibility of a disequilibrium in the global Alk inventory an imbalanced Alk budget during the pre-industrial era due to extra CaCO<sub>3</sub> burial at depth (Cartapanis et al., 2018), we created two configurations to account for this extra carbon burial (0.10 PgC yr<sup>-1</sup>): (i) in the deep Atlantic (atlpac-diseq), and (ii) in the shallow tropical regions (tropics-diseq), simulating the accumulation of carbon by corals-coral reefs (Fig. B1b).

820

Table B1. Summary of the sensitivity simulations led with NEMO-PISCES with their full description and characteristics (supplement to Table 2).

					1			
	Configuration				Parame	Parameterization		
Simulation	Description	Alk budget	Riverine discharge	OM burial	CaCO <sub>3</sub> burial	Atmospheric deposition	c Net addition	Alk restoration
std	Standard	Balanced	×	×	To conserve the global Alk	×	1	1
					inventory			
norivbur	No external fluxes of carbon and Alk,	Balanced	ı	1	ı	ı	ı	1
	except air-sea carbon fluxes							
rivref	Refractory organic riverine discharge	Balanced	Alk and carbon from organic	×	To conserve the global Alk	×	I	1
			riverine discharge are spread all		inventory			
			over the ocean					
rivorg	Fully organic riverine discharge	Balanced	For every mole of carbon	×	To conserve the global Alk	×	I	ı
			discharged by rivers, Alk is		inventory			
			discharged with the N: Cratio of					
			organic carbon discharge					
rivinorg	Fully inorganic riverine discharge	Balanced	For every mole of carbon	×	To conserve the global Alk	×	ı	ı
			discharged by rivers, a mole of Alk		inventory			
			is also discharged					
riv1p5	Riverine discharge of carbon and Alk	Balanced	1.5 times the amount of carbon	×	To conserve the global Alk	×	ı	ı
	multiplied by 1.5		and Alk supplied in std		inventory			
nosed-resto	No OM and CaCO <sub>5</sub> burial,	Balanced	×	ı	I	×	I	×
	but restoration of the Alk content							
nosed-diseq	No OM and CaCO <sub>3</sub> burial	Imbalanced	×	1	I	×	I	1
atlpac	Constrained balance of extra CaCO3	Balanced	×	×	To conserve the global Alk	×	Equivalent amount of carbon and Alk	1
	burial/dissolution between the deep				inventory, without		added/removed in the deep Pacific/Atlantic	
	Atlantic/Pacific				considering 'net addition'		(0.10 PgC yr-1 of carbon and 0.20 PgC yr-1 of Alk)	
atlpac-diseq	Constrained imbalance of extra CaCO3	Imbalanced	×	×	To conserve the global Alk	×	Twice more carbon and Alk removed in the deep	1
	burial/dissolution between the deep				inventory, without		Atlantic compared to the deep Pacific	
	Atlantic/Pacific (-0.10 PgC yr-1)				considering 'net addition'		(-0.20 PgC yr-1 relative to 0.10 PgC yr-1 of carbon,	
							and -0.40 PgC yr-1 relative to 0.20 PgC yr-1 of Alk)	
tropics-diseq	tropics-diseq Constrained extra CaCO3 burial in the	Imbalanced	×	×	To conserve the global Alk	×	Removal of carbon and Alk in the shallow tropics	ı
	shallow tropics (-0.10 PgC yr-1)				inventory, without		(-0.10 PgC yr-1 for carbon and -0.20 PgC yr-1 for Alk)	
					considering 'net addition'			

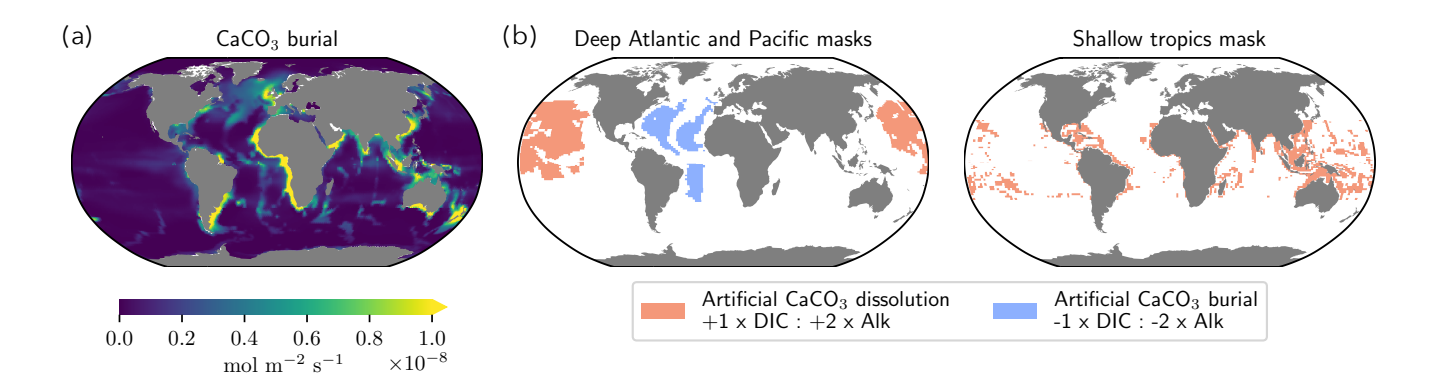


**Figure B1.** Towards a controlled adjustment of extra CaCO<sub>3</sub> burial/dissolution. (a) Map depicting CaCO<sub>3</sub> burial in the standard simulation (std). (b, c) Masks employed to drive (b) a balanced (atlpac) or an imbalanced (atlpac-diseq) additional CaCO<sub>3</sub> burial/dissolution between the deep Atlantic and Pacific, as well as (c) an extra CaCO<sub>3</sub> burial in the tropics. Red (blue) shading represents an addition (removal) of DIC and Alk in the grid cell at a 1:2 ratio. The grid cells considered for this addition/removal are located at 4750 m for the deep Atlantic and Pacific masks, and between 0 and 100 m for the tropics mask.

# **B3** The practical framework

830

835

We provide a schematic of the practical framework introduced in this manuscript (Sect. 4.2.1), which follows a four-step workflow to construct a composite simulation aligning with the most recent carbon and Alk budgets (Fig. E2).

Schematic of the practical framework introduced in this manuscript. Four-step workflow to construct a composite simulated estimate of the riverine/burial-driven air-sea carbon flux from a linear combination of our sensitivity simulations to match the most recent carbon and Alk budgets (riverine discharge, OM burial, and CaCO<sub>3</sub> burial). An additional step, equivalent to Step 3 but not shown in this general workflow, was necessary to adjust the CaCO<sub>3</sub> burial of carbon in excess (Regnier et al., 2022), compared to the values accounted for Alk (Middelburg et al., 2020).

### **B3** Ocean regions, and boundary conditions

The boundaries chosen to demarcate the southern, inter-tropical, and northern regions at 20°S and 20°N (see Fig. 4b, 3a, as well as Tables B1, E1, and E2) have indeed been previously employed in the literature (e.g., Aumont et al., 2001; Resplandy et al., 2018). These boundaries primarily align with physical features of the ocean, especially concerning air-sea carbon fluxes. It is in, or very close, to these latitudes that the air-sea carbon flux resulting from local imbalance reconciles with the simulated one (see Fig. 4c). By employing these boundaries, the air-sea carbon flux from regional carbon:Alk imbalances (see Sect. 2.1.2) closely matches the simulated values for each oceanic region (see Supplementary S1). This alignment deteriorates when the boundaries are shifted away from 20°S and 20°N. Consequently, we have opted for a consistent approach, maintaining the 20°S/N boundary to delineate distinct oceanic regions, despite the shift to 30°S/N boundaries in the GCB, primarily to correspond with terrestrial

biomes (Friedlingstein et al., 2024). However, for potential use in the GCB, we share values of the spatial distribution with boundaries at 30°S/N in Table E2.

### **Appendix C: Results and discussion**

#### **B1** NEMO-PISCES sensitivity simulations

## **B0.1** Spin-up

We track here the evolution of the net air-sea carbon flux during the spin-up for all the NEMO-PISCES sensitivity simulations (Table B1 and Fig. B1a), which are initially branched to a simulation at quasi-steady state equivalent to our standard simulation (std). Two characteristic time-scales emerge (Fig. B1b): (i) a short-term equilibration stabilisation over the first 50 yr, and (ii) a long-term equilibration stabilisation beyond 50 yr. The short-term (long-term) equilibration stabilisation primarily corresponds to the response of the surface (deep) ocean to the modifications associated with the configuration regarding the DIC and Alk external fluxes (Fig. B1c,d). Thus, for the simulation where we constrain extra CaCO<sub>3</sub> burial in the shallow tropics, only an equilibration a stabilisation of the surface ocean is generally needed, resulting in only a short-term equilibration a stabilisation. On the contrary, in the case where this extra CaCO<sub>3</sub> burial is constrained in the deep Atlantic, only an equilibration a stabilisation of the deep ocean is generally needed, resulting in only a long-term equilibrationstabilisation. Finally, in the case where riverine organic matter input is considered to be entirely refractory (rivref), a significant anomaly in external fluxes is induced at the surface compared to the standard simulation (std), as well as in the deep ocean because this organic carbon input is spread all over the ocean. This results in both short-term and long-term responses.

### **B0.2** Standard simulation (std)

860

865

We provide additional details here regarding the standard simulation (std, Fig. B2) to offer points of comparison with historical modeling studies that have initiated research efforts on this pre-industrial carbon flux (Aumont et al., 2001; Murnane et al., 1999).

## **B0.3** Residual carbon budget imbalance

A minor imbalance in the carbon budget from external sources/sinks persists without any associated ocean carbon content disequilibrium deviation in our sensitivity simulations. This discrepancy is particularly evident in the standard simulation (std; see 'Total' and 'Drift' in Fig. 4d) but is also observed in other simulations such as rivref, rivorg, rivinorg, riv1p5, atlpac, atlpac-diseq, and tropics-diseq (see Supplementary S2). To understand this counter-intuitive counterintuitive result initially, we must examine diazotrophic organisms, which produce OM without altering Alk. Let's imagine a thought experiment where the ocean contains external sources/sinks of carbon and Alk, such as riverine discharge and CaCO<sub>3</sub> burial, but maintains a global Alk inventory of zerobalanced Alk budget. Then, the ocean carbon balance can be performed independently of Alk to infer the air-sea carbon flux at equilibrium steady state (see Sect. 3.2.23.2.3). Now, let's introduce the production of OM

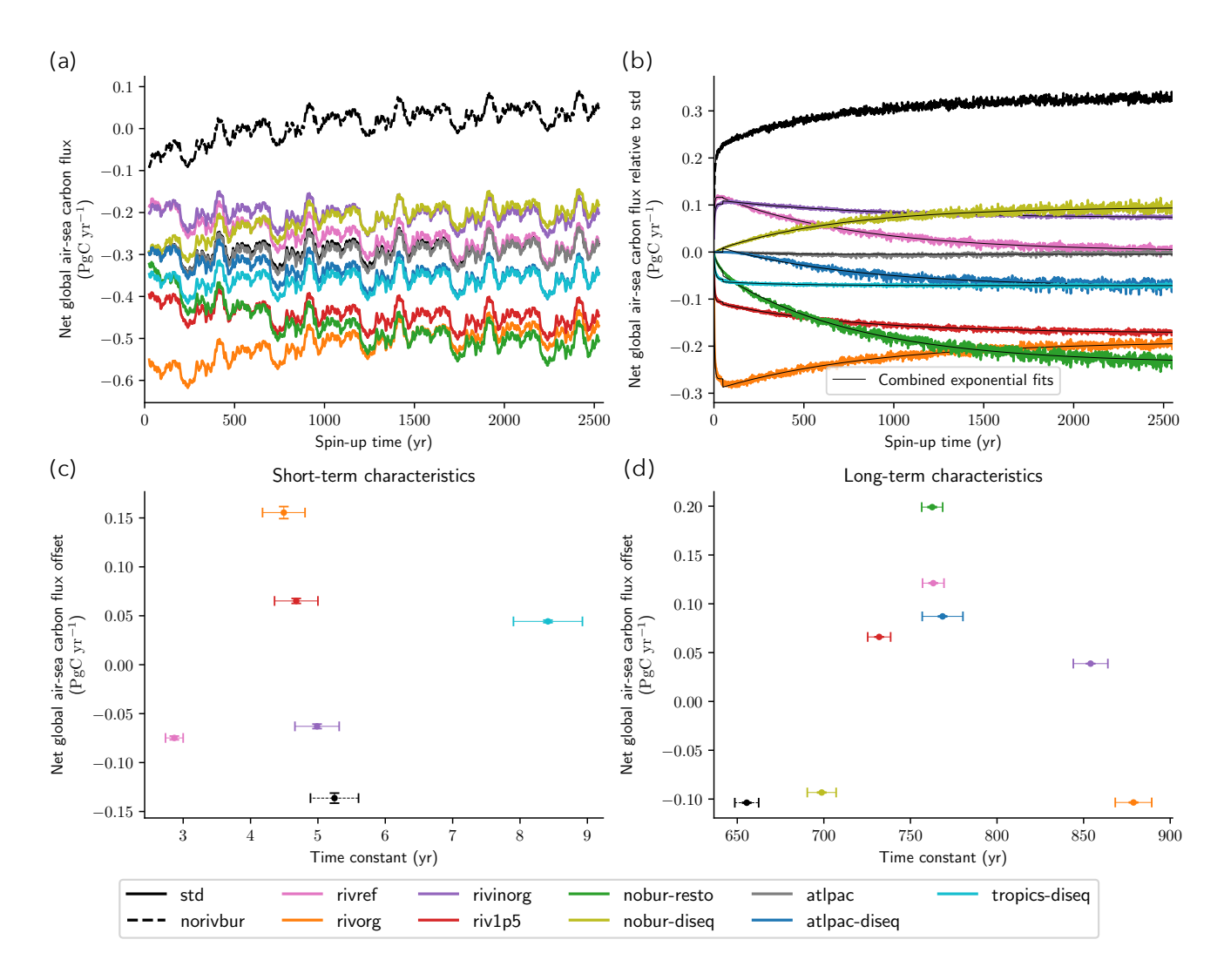
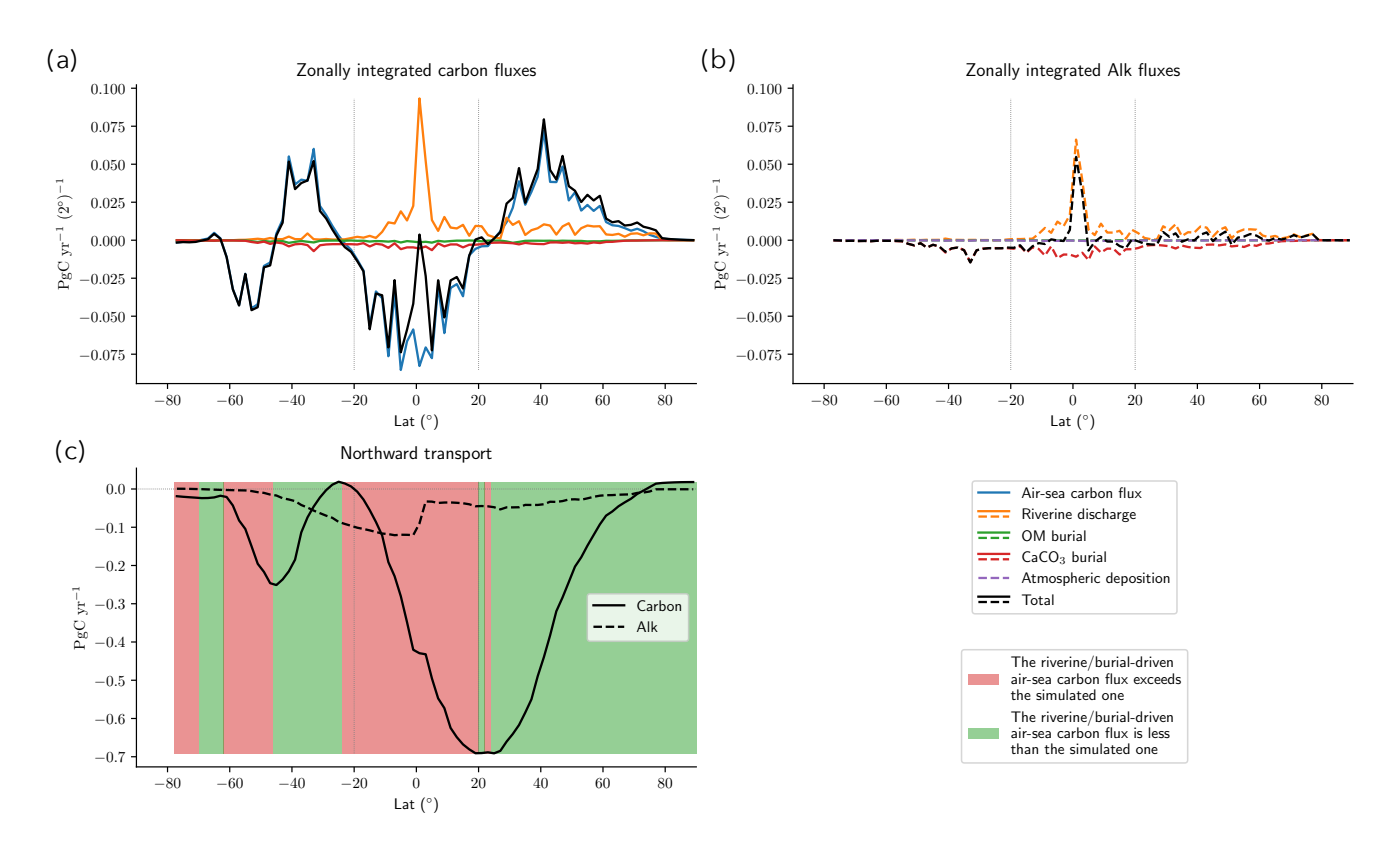


Figure B1. Spin-up of the NEMO-PISCES sensitivity simulations. (a) Time series of the net air-sea carbon flux with a 50-yr rolling mean throughout the 2550 yr of the simulations. (b) Same time series in relative to std and without smoothing. The thin black lines refer to the combined exponential fits  $(y = \alpha \cdot e^{-\frac{t}{\tau}} + \beta)$ , where  $\alpha$  is the net air-sea carbon flux offset,  $\tau$  is the time constant, and  $\beta$  is the baseline; using the *curve\_fit* function from the *scipy* python library): (i) one for the short-term considering the first 50 yr; and (ii) one for the long-term, considering the remaining 2500 yr. (c, d) for the short-term (c) and long-term (d) exponential fits, the net air-sea carbon flux offset  $\alpha$  is displayed in function of the time constant  $\alpha$  with their associated uncertainties.



**Figure B2.** Description of the standard NEMO-PISCES simulation (std; continued from Fig. 2). Zonally integrated (a) carbon and (b) Alk fluxes in supplement to Fig. 2b. (c) Latitudinal distribution of the northward transport of carbon (solid) and Alk (dahsed). When the local regional imbalance exceeds (falls behind) the simulated air-sea carbon flux, the area in between is shaded in red (green).

by diazotrophic organisms into this ocean at equilibriumsteady-state ocean, assuming that all of it is buried. These organisms will consume carbon in the surface ocean and export it in the sediments without affecting Alk. This leads to a carbon sink in the ocean, which, when brought back to equilibriumsteady state, is counter-balanced by a positive air-sea carbon flux. Therefore, the imbalance in the carbon budget for std results from the OM burial produced by diazotrophs. In reality, the effect of diazotrophic organisms is more complex, as only a fraction of their OM is buried, and the rest is remineralized, leading to an increase in Alk. However, a similar effect on the air-sea carbon flux would be observed, albeit with a different magnitude. Since we could not determine the distribution of this induced air-sea carbon flux, we could not correct this slight imbalance in the carbon budget from external sources/sinks, except in Fig. 5, where only the total value of the air-sea carbon flux is considered, without its distribution. Please note that this unaccounted-for air-sea carbon flux stemming from external ocean carbon and Alk sources/sinks also contributes to the understanding of the slight discrepancy between the simulated air-sea carbon flux and the one resulting from the carbon; Alk global imbalance (e.g. +0.04 PgC yr<sup>-1</sup> for std; see Fig. 4c and Fig. B3a).

Another type of imbalance in the carbon budget is evident in the simulation without external ocean source/sink (norivbur), accompanied by a disequilibrium in non-conserved ocean carbon and Alk contents-inventories (see 'Total' and 'Drift' in Supplementary S2 and Fig. B3a). This imbalance arises from the representation of nitrogen reactions in NEMO-PISCES, which includes the restoration of nitrate content in the ocean. An imbalance between nitrification (decreasing Alk) and denitrification (increasing Alk) leads to an internal Alk disequilibrium imbalance (an imbalance stemming from N-reactions is also reported in COBALTv2 Stock et al., 2020). This is not compensated for by the strategy used to maintain the global-conserve the Alk inventory, as CaCO<sub>3</sub> burial is not considered in this simulation (see Sect. 2.2). At equilibriumsteady state, this positive global Alk inventory disequilibrium ( $D^{tAlk}$  deviation ( $D^{Alk}$ ) results in an air-sea carbon flux ( $E^{tC_{t}}$  air-sea  $E^{tC_{t}}$  air-sea) and an ocean carbon content disequilibrium ( $D^{tC}$  deviation ( $D^{C}$ ) of the same magnitude:  $E^{tC_{t}}$  air-sea  $E^{tC_{t}}$  air-sea  $E^{tC_{t}}$  air-sea  $E^{tC_{t}}$  air-sea  $E^{tC_{t}}$  air-sea  $E^{tC_{t}}$  air-sea and an ocean carbon content disequilibrium ( $E^{tC_{t}}$  air-sea and  $E^{tC_{t}}$  and  $E^{tC_{t}}$  are an anon-conserved ocean carbon content. As expected, this imbalance is almost equivalent in the simulation

Very minor residual undesirable disturbances, such as disequilibria deviations or slight inconsistencies in the budgets over the 50-year period considered, may persist due to the minor non-linearity occurring during the burial of CaCO<sub>3</sub> when the global Alk inventory is constrained to be equilibrated conserved by the burial of CaCO<sub>3</sub>. Additionally, the modeling scheme of the physical part of NEMO-PISCES induces a slight Alk disequilibrium deviation and a slightly more pronounced carbon content disequilibrium deviation (respectively -0.002 PgC yr<sup>-1</sup> and +0.01 PgC yr<sup>-1</sup> in std).

## **B0.4** NEMO-PISCES sensitivity simulation ensemble

885

890

895

900

910

We provide a comprehensive overview of the global-scale carbon and Alk budgets for all NEMO-PISCES sensitivity simulations (Fig. B3). Even more detailed information can be found in Supplementary S1 and S2 (https://doi.org/10.5281/zenodo. 8421898). Finally, we also provide a comprehensive characterization of the air-sea carbon flux in the NEMO-PISCES sensitivity simulations, including both the total flux and the riverine/burial-driven component (Table B1).

## Appendix C: Ocean regions, and boundary conditions

The boundaries chosen to demarcate the southern, inter-tropical, and northern regions at 20°S and 20°N (see Fig. 3a, 4b, as well as Tables B1, E1, and E2) have indeed been previously employed in the literature (e.g. Aumont et al., 2001; Resplandy et al., 2018). These boundaries primarily align with physical features of the ocean, especially concerning air-sea carbon fluxes. It is in, or very close, to these latitudes that the air-sea carbon flux resulting from regional carbon:Alk budget imbalance reconciles with the simulated one (see Fig. 4c). By employing these boundaries, the air-sea carbon flux from regional carbon:Alk budget imbalances (see Sect. 2.1.2) closely matches the simulated values for each oceanic region (see Supplementary S1). This

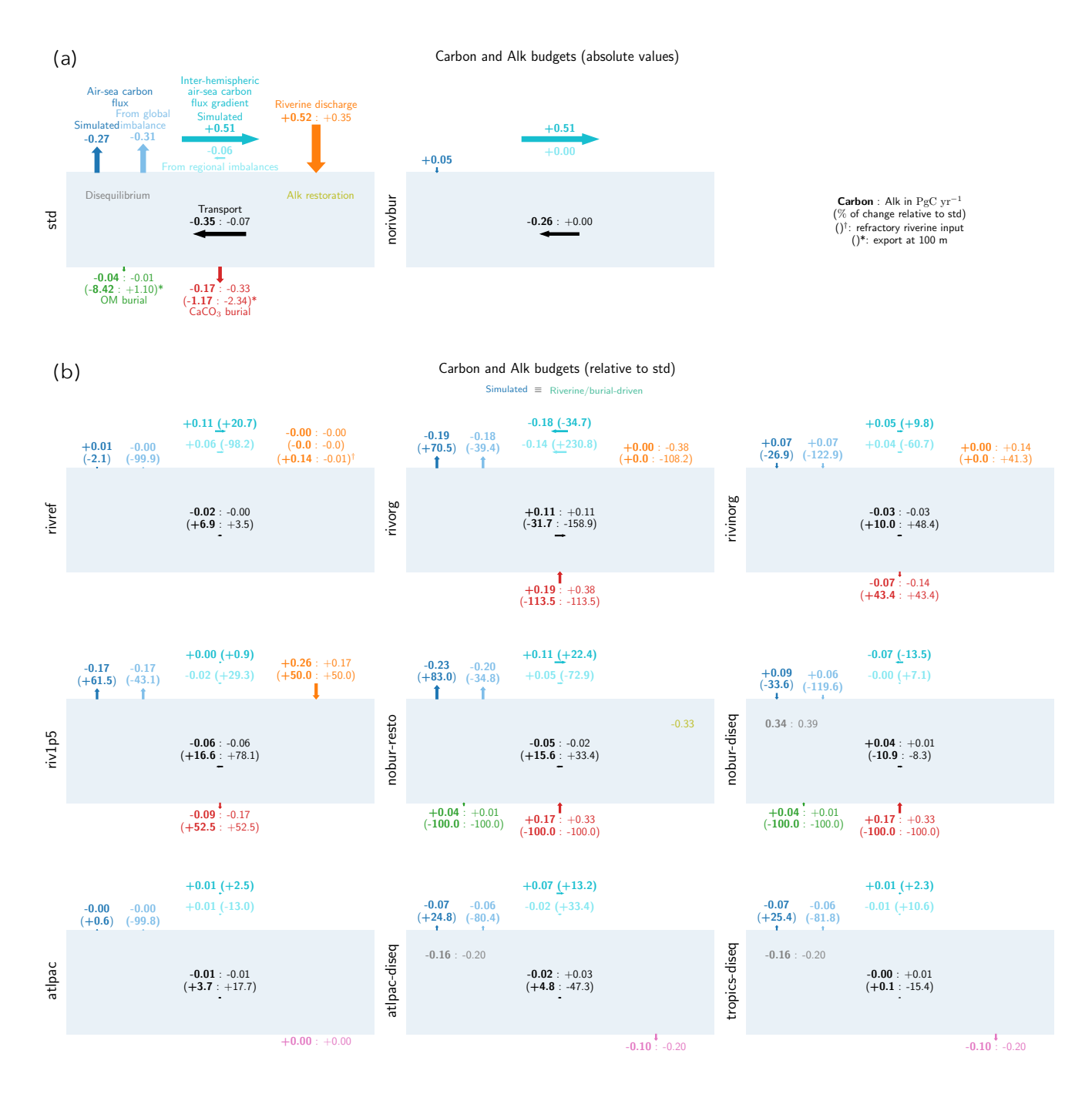


Figure B3. Global-scale carbon and Alk budgets for all NEMO-PISCES sensitivity simulations. (continued)

**Figure B3.** (*continued*). Carbon and Alk budgets (a) in absolute values for the standard simulation (std) and the simulation without riverine and burial fluxes of carbon and Alk (norivbur), or (b) relative to std for the other NEMO-PISCES sensitivity simulations. The type of representation is close to the one shared in Fig. 4c, but integrated over the whole ocean. All fluxes, in petagrams of carbon per year (PgC yr<sup>-1</sup>) for carbon (in bold) and Alk (in normal font), are directed by arrows, with orientation indicating the sign, and size reflecting the absolute magnitude of the flux. In (b), only the fluxes (riverine discharge, as well as OM and CaCO<sub>3</sub> burial) with a significant anomaly are displayed, along with their associated changes relative to the standard simulation (std) in brackets, for both carbon (bold) and Alk (normal font). Additionally, values for carbon and Alk disequilibria deviations (for simulations with a '-diseq' suffix), net addition flux (for atlpac, atlpacdiseq, and tropics-diseq), or the term of Alk restoration (for nosed-resto) is/are also shown when applicable (Table B1). In (a), for the standard simulation (std), a first approximation of the impact of OM and CaCO<sub>3</sub> production in the surface waters is also inferred from POC and PIC export at 100 m (in brackets with a star). Finally, in addition to the air-sea carbon flux (dark blue), the air-sea carbon flux stemming from global imbalance (light blue; Sect. 2.1.2 and Appendix B0.3 for an explanation of the residual imbalance) is also shared, as well as the associated inter-hemispheric air-sea carbon flux gradient (dark and light cyan). In (b), as the values are shown relative to the standard simulation (std), the simulated air-sea carbon flux anomalies are equivalent to the ones of the riverine/burial-driven air-sea carbon flux. A detailed description of the NEMO-PISCES sensitivity simulations can be found in Supplementary S1 and S2.

**Table B1.** Comprehensive description of the net air-sea carbon flux in the NEMO-PISCES sensitivity simulations. The values provided in parentheses are expressed relative to the simulation without riverine and burial fluxes, representing the riverine/burial-driven air-sea carbon flux or carbon transport.

C!1-4'			Net air-sea	carbon flux		Inter-hemispheric
Simulation	South	Inter-tropics	North	Total	Inter-hemispheric gradient	transport
	(<20°S)	$(20^{\circ}\text{S} - 20^{\circ}\text{N})$	(>20°N)	Iotai	(north - south)	of carbon
std	0.06 (-0.10)	-0.91 (-0.12)	0.57 (-0.10)	-0.27 (-0.32)	0.51 (-0.00)	-0.35 (-0.09)
norivbur	0.16	-0.79	0.67	0.05	0.51	-0.26
rivref	-0.01 (-0.17)	-0.86 (-0.08)	0.61 (-0.07)	-0.27 (-0.32)	0.62 (0.10)	-0.37 (-0.11)
rivorg	0.11 (-0.05)	-1.03 (-0.24)	0.45 (-0.23)	-0.47 (-0.52)	0.33 (-0.18)	-0.24 (0.02)
rivinorg	0.05 (-0.11)	-0.86 (-0.08)	0.61 (-0.06)	-0.20 (-0.25)	0.56 (0.05)	-0.38 (-0.12)
riv1p5	0.01 (-0.15)	-0.97 (-0.19)	0.52 (-0.15)	-0.44 (-0.49)	0.51 (0.00)	-0.40 (-0.15)
nobur-resto	-0.09 (-0.25)	-0.95 (-0.16)	0.54 (-0.14)	-0.50 (-0.55)	0.62 (0.11)	-0.40 (-0.14)
nobur-diseq	0.15 (-0.01)	-0.93 (-0.14)	0.59 (-0.08)	-0.18 (-0.23)	0.44 (-0.07)	-0.31 (-0.05)
atlpac	0.05 (-0.11)	-0.90 (-0.12)	0.57 (-0.10)	-0.28 (-0.33)	0.52 (0.01)	-0.36 (-0.10)
atlpac-diseq	-0.01 (-0.17)	-0.89 (-0.11)	0.57 (-0.11)	-0.34 (-0.39)	0.58 (0.06)	-0.36 (-0.11)
tropics-diseq	0.03 (-0.14)	-0.92 (-0.13)	0.55 (-0.13)	-0.34 (-0.39)	0.52 (0.01)	-0.35 (-0.09)

alignment deteriorates when the boundaries are shifted away from 20°S and 20°N. Consequently, we have opted for a consistent approach, maintaining the 20°S/N boundary to delineate distinct oceanic regions, despite the shift to 30°S/N boundaries in the GCB, primarily to correspond with terrestrial biomes (Friedlingstein et al., 2024). However, for potential use in the GCB, we share values of the spatial distribution with boundaries at 30°S/N in Table E2.

## Appendix D: Inter-hemispheric air-sea carbon flux gradient

# D1 Partitioning between the northern and southern components

We share additional insights regarding the inter-hemispheric air-sea carbon flux gradient, which is crucial for the global carbon cycle in its connection with the atmosphere and land (e.g. Keeling et al., 1989; Resplandy et al., 2018). It is thus valuable to distinguish in this inter-hemispheric gradient the component associated with the net air-sea carbon flux in both the southern and northern regions (Fig. D1).

## **D2** Partitioning between carbon transport and riverine and burial processes

# **D2.1** Expression

In addition to defining the inter-hemispheric air–sea carbon flux gradient (G), and the inter-hemispheric oceanic transports of carbon  $(T^{C})$  and Alk  $(T^{Alk})$ , we propose here a decomposition of G into contributions associated with carbon transport and with riverine and burial processes.

To this end, we recall that the total regional fluxes of carbon and Alk can be expressed as follows:

$$\begin{cases} F_{N/S/I}^{\text{C}} = F_{N/S/I}^{\text{C, air-sea}} + F_{N/S/I}^{\text{C, riv./bur.}} \\ F_{N/S/I}^{\text{Alk}} = F_{N/S/I}^{\text{Alk, riv./bur.}} \end{cases}$$
(D1)

Specifically, by considering these fluxes  $(F_{N,S,L}^{C/Alk})$  along with regional carbon and Alk deviations  $(D_{N,S,L}^{C/Alk})$  and assuming a steady-state ocean (see Fig. B1), we derive two expressions for the ocean transport of carbon and Alk through their respective budget closure equations  $(T_{N/S}^{C/Alk})$ :

$$\begin{cases} T_{N/S}^{\text{C/Alk}} + F_{\geq 20^{\circ} N/20^{\circ} S}^{\text{C/Alk}} + D_{\geq 20^{\circ} N/20^{\circ} S}^{\text{C/Alk}} = 0\\ -T_{N/S}^{\text{C/Alk}} + F_{< 20^{\circ} N/20^{\circ} S}^{\text{C/Alk}} + D_{< 20^{\circ} N/20^{\circ} S}^{\text{C/Alk}} = 0 \end{cases}$$
(D2)

Hence, we define the ocean transport of carbon and Alk as the average of its two expressions (Eq. D2; Fig. 3b):

935 
$$T_{N/S}^{\text{C/Alk}} = \frac{1}{2} \cdot \left[ \left( F_{<20^{\circ}N/20^{\circ}S}^{\text{C/Alk}} + D_{<20^{\circ}N/20^{\circ}S}^{\text{C/Alk}} \right) - \left( F_{\geq20^{\circ}N/20^{\circ}S}^{\text{C/Alk}} + D_{\geq20^{\circ}N/20^{\circ}S}^{\text{C/Alk}} \right) \right]$$
 (D3)

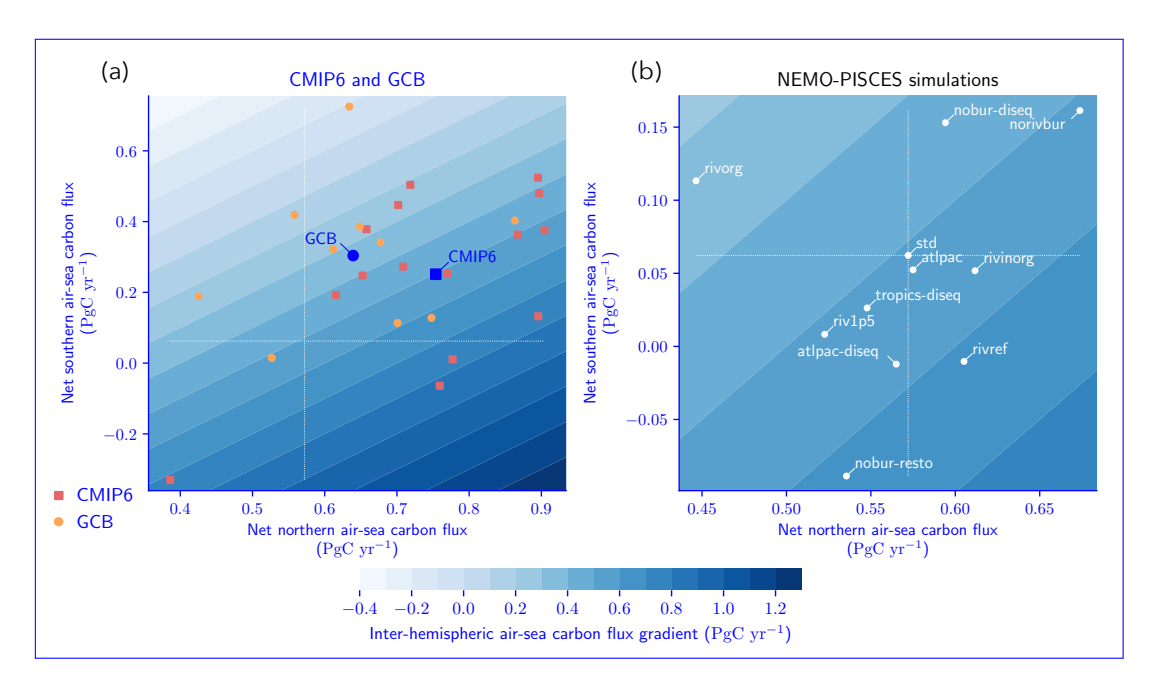


**Figure D1.** Decomposition of the inter-hemispheric air-sea carbon flux gradient (supplement to Fig. 2). Decomposition of the inter-hemispheric air-sea carbon flux gradient into the net southern and northern air-sea carbon fluxes for (a) CMIP6 and GCB, and (b) the NEMO-PISCES sensitivity simulations. Filled contours correspond to the inter-hemispheric air-sea carbon flux gradient. (a) The 15 CMIP6 ESMs (10 GCB GOBMs) are plotted with red squares (orange circles). The black square and circle refer to the CMIP6 and GCB ensemble means. In (b), secondary axes have been added to characterize the implied changes for the southern/northern air-land carbon flux relative to std, if the inter-hemispheric gradient is considered as well-represented. Then, a decrease in the net sourthern (northern) air-sea carbon flux relative to std entails an increase of the same magnitude in the net southern (northern) air-land carbon flux relative to std, and conversely.

In particular:

$$\begin{cases} T_{N}^{\text{C/Alk}} = \frac{1}{2} \cdot \left[ \left( F_{S}^{\text{C/Alk}} + D_{S}^{\text{C/Alk}} + F_{I}^{\text{C/Alk}} + D_{I}^{\text{C/Alk}} \right) - \left( F_{N}^{\text{C/Alk}} + D_{N}^{\text{C/Alk}} \right) \right] \\ T_{S}^{\text{C/Alk}} = \frac{1}{2} \cdot \left[ \left( F_{S}^{\text{C/Alk}} + D_{S}^{\text{C/Alk}} \right) - \left( F_{I}^{\text{C/Alk}} + D_{I}^{\text{C/Alk}} + F_{N}^{\text{C/Alk}} + D_{N}^{\text{C/Alk}} \right) \right]$$
 (D4)

from which an expression of the inter-hemispheric transport of carbon and Alk (Eq. 12) can be derived:

$$T^{\text{C/Alk}} = \frac{1}{2} \cdot \left[ \left( F_S^{\text{C/Alk}} + D_S^{\text{C/Alk}} \right) - \left( F_N^{\text{C/Alk}} + D_N^{\text{C/Alk}} \right) \right] \tag{D5}$$

940 Specifically, using Eq. D1, the inter-hemispheric transport of carbon can be rewritten as follows:

$$T^{\mathcal{C}} = \frac{1}{2} \cdot \left[ \left( F_S^{\mathcal{C}, \text{ air-sea}} + F_S^{\mathcal{C}, \text{ riv./bur.}} + D_S^{\mathcal{C}} \right) - \left( F_N^{\mathcal{C}, \text{ air-sea}} + F_N^{\mathcal{C}, \text{ riv./bur.}} + D_N^{\mathcal{C}} \right) \right]$$

$$(D6)$$

After rearrangement, the inter-hemispheric air-sea carbon flux gradient can be expressed as:

$$G = \underbrace{-2 \cdot T^{\text{C}}}_{\text{Transport component}} - \underbrace{-\left(F_N^{\text{C, riv./bur.}} - F_S^{\text{C, riv./bur.}}\right) - \left(D_N^{\text{C}} - D_S^{\text{C}}\right)}_{\text{Riverine and burial component}}$$
(D7)

At first glance, it may appear that this expression is exclusively formulated in terms of carbon, seemingly without any consideration of Alk. However, Alk plays a subtle yet integral role in this equation. Firstly, because  $T^C$  depends on both the southern and northern air-sea carbon fluxes (Eq. D5 and D1), and these regional fluxes are chemically driven by the relative imbalance between Alk and DIC. Secondly, the deviations in the carbon content of the northern and southern oceans ( $D_N^C$  and  $D_S^C$ , respectively) are directly linked to the deviations in Alk content (Eq. 10). Thus, the role of Alk is intricately interwoven within the formulation of G (Eq. D7).

## 950 D2.2 Results

955

960

965

970

It is possible to decompose the inter-hemispheric gradient of the riverine/burial-driven air-sea flux into a component associated with the inter-hemispheric transport of a carbon:Alk budget imbalance and a component associated with a carbon:Alk budget imbalance stemming from riverine and burial fluxes (including inventory deviations; Eq. D7, and Fig. D2, D3, and E1). Focusing solely on the effect of riverine and burial fluxes (i.e. relative to norivbur), the component associated with these external fluxes (-0.07 PgC yr<sup>-1</sup>) is offset by the transport-related component (+0.07 PgC yr<sup>-1</sup>) in the standard configuration, resulting in a null inter-hemispheric riverine/burial-driven air-sea carbon flux gradient for std (Fig. 5b and Fig. D2). In the case of a surplus of CaCO<sub>3</sub> burial in the deep Atlantic (atlpac-diseq), the increase in the inter-hemispheric riverine/burial-driven air-sea carbon flux gradient relative to std (+0.07 PgC yr<sup>-1</sup>; see Fig. B3b) is primarily attributed to the transport of a carbon:Alk budget imbalance (Fig. D2). Conversely, when the riverine discharge is entirely organic (rivorg), it is mostly the external flux component that causes the decrease in the inter-hemispheric air-sea carbon flux gradient relative to std (-0.18 PgC yr<sup>-1</sup>; see Fig. B3b and Fig. D2), and the same outcome occurs when the riverine discharge is entirely inorganic (rivinorg). This emphasizes that the spatial distribution of the carbon:Alk budget imbalance stemming from external fluxes, in conjunction with oceanic transport, plays a significant role in shaping the pre-industrial inter-hemispheric riverine/burial-driven air-sea carbon flux gradient.

### **Appendix E: Applications**

#### E1 Literature review

Here, we provide a literature review on: (i) the evolution of the assessment and characterization of the air-sea carbon flux since the late 1990s (Table E1); and (ii) the evolution of the estimation and characterization of the riverine/burial-driven air-sea carbon flux in comparison with our composite simulated estimate (Table E2). We also provide the PDFs of the literature-based estimates for the ocean's external sources/sinks of carbon and Alk, derived from the most recent carbon and Alk budgets

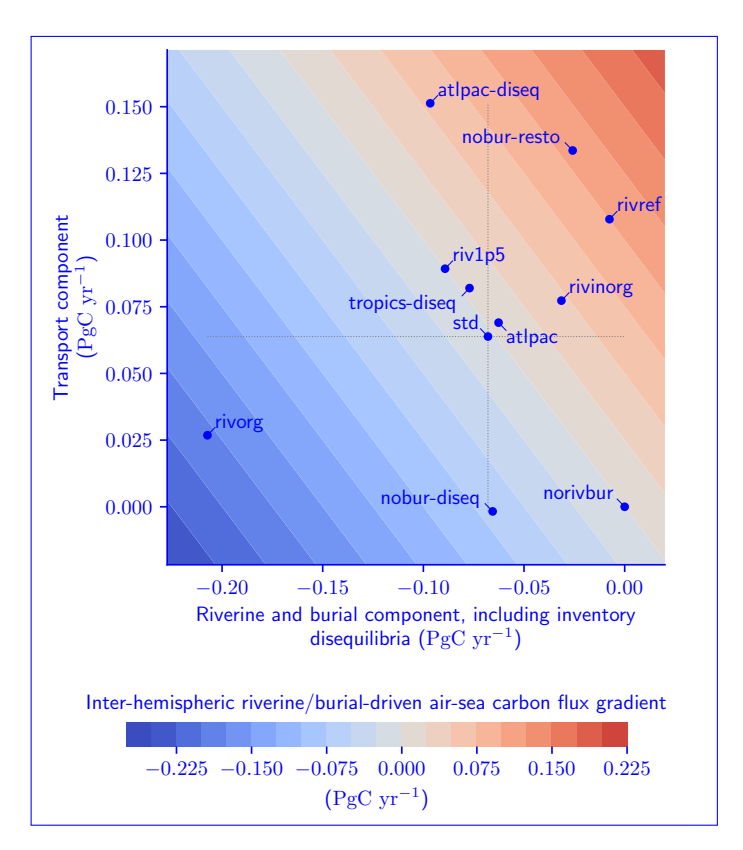


**Figure D2.** Drivers of the spatial distribution of the riverine/burial-driven air-sea carbon flux. Inter-hemispheric gradient of the riverine/burial-driven air-sea carbon flux (filled contours) and its two components, from carbon:Alk budget imbalances (see Sect. 2.1.2 and 2.1.3). One component (x-axis) is associated with the inter-hemispheric gradient of air-sea carbon flux driven by northern and southern carbon:Alk budget imbalances (and inventory deviations), while the other component (y-axis) corresponds to the inter-hemispheric gradient of air-sea carbon flux associated to the inter-hemispheric transport of the carbon:Alk budget imbalance (Eq. D7 and Fig. D1). The deviation in the simulated inter-hemispheric gradient in NEMO-PISCES sensitivity simulations as compared to the reconstructed ones using the two components is minimal ( $< 0.01 \, \mathrm{PgC} \, \mathrm{yr}^{-1}$ , not shown).

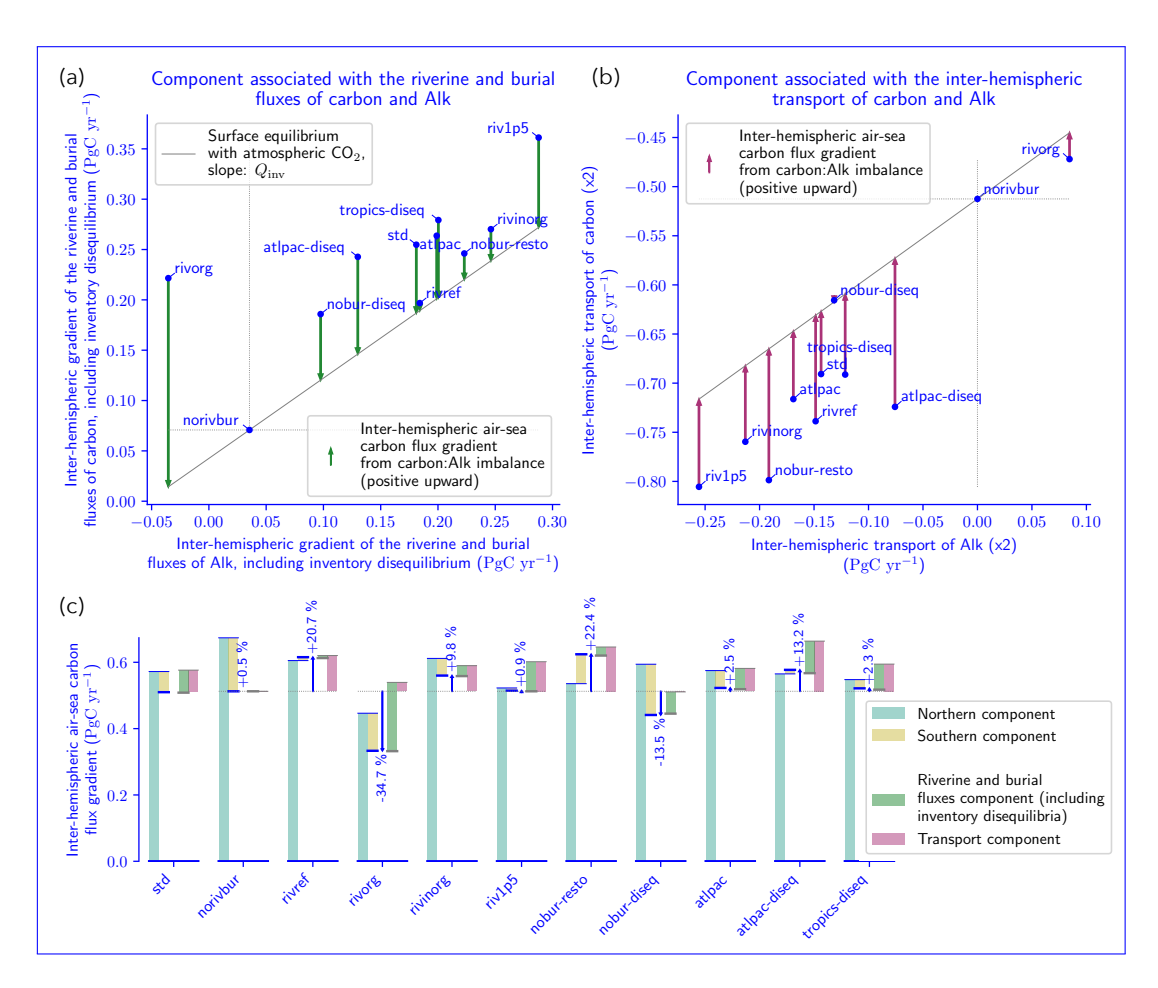


Figure D3. Partitioning of the inter-hemispheric air-sea carbon flux gradient from inter-hemispheric carbon:Alk budget imbalances (supplement to D2). (a, b) Visual construction of the inter-hemispheric air-sea carbon flux gradient resulting from regional carbon:Alk budget imbalances due to (a) riverine and burial fluxes (including inventory deviations), and (b) inter-hemispheric transport, defining the values used in Fig. D2. The reference was set on the simulation without riverine and burial fluxes (norivbur), so that the combination of the arrows of (a) and (b) results in the inter-hemispheric riverine/burial-driven air-sea carbon flux gradient. (c) Synthetic characterization for the whole set of NEMO-PISCES sensitivity simulations of the inter-hemispheric air-sea carbon flux gradient: with a southern/northern decomposition (as in Fig. D1b), and the partitioning resulting from regional carbon:Alk budget imbalances due to riverine and burial fluxes (including inventory deviations) – constructed in (a) –, and inter-hemispheric transport – constructed in (b).

(Regnier et al., 2022; Middelburg et al., 2020), which were used to construct the composite simulated estimate (Fig. E1, see Table 3 as well as Sect. 4.2.1 and 4.2.2).

a All the ocean biogeochemistry model used in the following studies both account for the physical carbon pump and the biological one (soft-tissue and carbon ade).

Boundaries at 15°5/N. Boundaries at the equator.

Table E1. Literature review of the net air-sea carbon flux and its characterization. Bold lines are those accounting for external fluxes and boundaries at 20°S/N for the spatial distribution.

	Describeron of the method							2112112
Source	and further characterization		South (<20°S)	Inter-tropics $(20^{\circ}\text{S} - 20^{\circ}\text{N})$	North (>20°N)	Total	Inter-hemispheric gradient (north - south)	transport of carbon
	PPOM	Moddeling approach <sup>a</sup>						
Murnane et al. (1999)	No external fluxes of carbon and Alk. The CaCO3 reaching the seafloor is redissolved	Princeton model	09.0	-1.20 <sup>b</sup>	0900	0.00	0.00 <sup>b</sup>	
	at the surface to conserve the global Alk inventory.							
Samiento et al. (2000)	Intercomparison study of three ocean biogeochemistry models with the same	Princeton model	-0.55°		-0.09€	-0.64		
	implicit riverine discharge of 0.64 PgC yr <sup>-1</sup> split between the northern and southern							
	hemispheres (respectively -0.21 and -0.43 PgC yr <sup>-1</sup> for the associated outgassing).							
		IPSL model	-0.53°		-0.11°	-0.64		
		MPI model	-0.39°		-0.25°	-0.64		
Aumont et al. (2001)	No external fluxes of carbon and Alk. The CaCO3 reaching the seafloor is redissolved	IPSL model	0.73	-1.40	0.67	0.00	-0.06	-0.10
	at depth to conserve the global Alk inventory.							
	Carbon and Alk riverine discharge of respectively 0.81 and 0.40 PgC yr <sup>-1</sup> , the global	IPSL model 0.43	0.43	-1.55	0.51	-0.61	80.0	-0.25
	Alk inventory being conserved through an equivalent CaCO3 burial. Regarding the							
	riverine carbon (0.41 PgC yr¹), 1/3 is injected as DIC at the river mouth and the rest							
	is injected as DOC with an oxidation time-scale of 100 yr.							
Lacroix et al. (2020)	No external fluxes of carbon and Alk. The CaCO3 reaching the seafloor is redissolved	MPI model				-0.05		
	homogeneously at the surface to conserve the global Alk inventory, same for organic							
	mater. This results in an equivalent implicit riverine discharge of 0.314 PgC yr¹for							
	carbon and 0.208 PgC yr <sup>-1</sup> for Alk.							
	Constrained riverine discharge (0.603 PgC yr <sup>-1</sup> for carbon and 0.366 PgC yr <sup>-1</sup> for Alk)	MPI model				0.18		
	based on a hierarchy of weathering and terrestrial organic matter export models,							
	while identifying regional hotspots of the riverine exports. OM and CaCO <sub>3</sub> burial are							
	considered and not constrained (respectively 0.582 and 0.188 PgC yr <sup>-1</sup> ), making free							
	the global Alk inventory.							
Present study	Linear combination of sensitivity simulations to match literature estimates of the	IPSL model	$0.01\pm0.13$	IPSL model $0.01\pm0.13$ $-0.99\pm0.10$	$\textbf{0.51} \pm \textbf{0.08}$	$\textbf{0.51} \pm \textbf{0.08}  \textbf{-0.46} \pm \textbf{0.24}  \textbf{0.50} \pm \textbf{0.15}$	$0.50\pm0.15$	$\textbf{-0.16} \pm \textbf{0.08}$
(composite simulated estimate)	(composite simulated estimate) external sources/sinks of carbon and AIk							

(continued)

	Decomingtion of the method			Net air-sea	Net air-sea carbon flux		Inter-homicahonio
Source	and further characterization	South (<20°S)	Inter-tropics $(20^{\circ}S - 20^{\circ}N)$	North (>20°N)	Total	Inter-hemispheric gradient (north - south)	transport of carbon
	- 1	inversion					
Sarmiento and Sundquist (1992)		$0.82^{b}$	-1.70°	0.28 <sup>b</sup>	-0.60	0.54 <sup>b</sup>	
	carbon uptake to the revised carbon budget by Tans et al. (1990) from a combination of an atmospheric transport						
	model with a compilation of observations of air-sea CO <sub>2</sub> difference.						
Jacobson et al. (2007)	Use of a combination of transport inversions of atmospheric (constraining fluxes into the atmosphere from both				$-0.39\pm0.19$		
	land and ocean) and oceanic observations (constraining only air-sea fluxes), using multiple circulation models to						
	assess the effects of errors in simulated transport. The ocean inversion estimates are corrected to remove the						
	riverine carbon discharge (0.45 PgC ${ m yr}^{1}$ ).						
	Ocean inversion						
Gloor et al. (2003)°	Use of an ocean general circulation model as well as observations of DIC and other tracers. The values were	0,32 <sup>d</sup>	-1.35 <sup>d</sup>	0.63 <sup>d</sup>	69:0-	0.60 <sup>d</sup>	
	corrected to remove the riverine carbon discharge with the estimate (0.45 PgC yr <sup>-1</sup> ) from Jacobson et al. (2007)						
Mikaloff Fletcher et al. (2007) <sup>f</sup>	Use of ten different ocean general circulation models (to quantify the error arising from uncertainties in the	he $0.21 \pm 0.16$	$\textbf{-1.10} \pm \textbf{0.16}$	$\textbf{0.40} \pm \textbf{0.14}$	$0.40 \pm 0.14$ -0.49 $\pm 0.27$	$\textbf{0.19} \pm \textbf{0.21}$	$\textbf{-0.19} \pm 0.09$
	modeled transport) as well as observations of DIC and other tracers. The values were corrected to remove the	the					
	riverine carbon discharge with the estimate (0.45 PgC yr <sup>-1</sup> ) from Jacobson et al. (2007).						
	pCO <sub>2</sub> -based						
Resplandy et al. (2018)	Reconstruction of the modern-day air-sea carbon flux from the global surface ocean Takahashi et al. (2009)	009) -0.16 ± 0.38	$-1.09 \pm 0.22$	$0.41\pm0.23$	$-0.84 \pm 0.50$	$0.57 \pm 0.44$	
	pCO <sub>2</sub> field. The anthropogenic carbon flux is then extracted using an observationnally						
	based reconstruction with a Green's function estimated from tracer data						
	(Khatiwala et al., 2009). The values were corrected to remove the riverine carbon						
	discharge with the estimate (0.45 PgC yr <sup>-1</sup> ) from Jacobson et al. (2007).						
	Wanninkhof et al. (2013)	013)			$\textbf{-1.00} \pm 0.67$		
	Landschützer et al. (2014)	014) $-0.04 \pm 0.38$	$-1.11 \pm 0.22$	$0.45\pm0.23$	$-0.70 \pm 0.50$	$0.49 \pm 0.44$	
	Same as above, except that riverine carbone discharge is constrained to ensure the Rödenbeck et al. (2013)	013) $0.00 \pm 0.38$	$-1.29 \pm 0.22$	$0.51\pm0.22$	$-0.78 \pm 0.50$	$0.51 \pm 0.44$	-0.43
	closing of the ocean carbon budget (only considering air-sea fluxes and riverine						
	carbon discharge).						
Regnier et al. (2022)	Reconstruction of the modern-day air-sea carbon flux from the global surface ocean $p$ CO <sub>2</sub> field	0.20	-1.47	0.61	$-0.65 \pm 0.30$	0.41	
	(Landschützer et al., 2014). The anthropogenic carbon flux is then extracted using three different methods: global	=					
	ocean bioseochemistry models, ocean circulation inverse model, and pCO <sub>2</sub> -based flux mapping models – with a						
	post-correction applied to the latter for the rivers (0.6 PgC yr <sup>-1</sup> ) – (DeVries et al., 2019). The values were corrected	pa					
	to remove the riverine carbon discharge with the estimate (0.45 PgC yr <sup>-1</sup> ) from Jacobson et al. (2007).						
	Mean	$Mean \pm std^g  0.00 \pm 0.22$	$\textbf{-1.24} \pm \textbf{0.13}$	$\textbf{0.46} \pm \textbf{0.13}$	$0.46 \pm 0.13$ $-0.74 \pm 0.29$ $0.46 \pm 0.25$	$\textbf{0.46} \pm \textbf{0.25}$	

<sup>b</sup> Boundaries at 15°SN. <sup>d</sup> Boundaries at 13°SN. <sup>c</sup> The values were extracted from the Supplementary Figure of Mikaloff Fleicher et al. (2007). <sup>f</sup> Values from Resplandy et al. (2018). <sup>g</sup> Accounting for all the pCO<sub>2</sub>-based estimates, except the one by Wanninkhof et al. (2013), which is incomplete.

and CaCO<sub>3</sub> burial. The values obtained from the composite simulated estimate are also shared in grey. Note that its riverine discharge, OM burial and CaCO<sub>3</sub> fluxes Table E2. Literature review of the riverine/burial-driven air-sea carbon flux estimates, sharing also values and a description of the riverine discharge, OM burial, (see Table 3) differ from those considered in the GCB and derived from Regnier et al. (2022), as we also account for flux on continental shelves.

							Air-sea carbon outgassing from	Partitioning	
	Riverine discharge		OM burial		CaCO <sub>3</sub> burial		riverine and burial	(south; inter-tropics; north)	north)
							fluxes of carbon and Alk	with boundaries at 20°S/N	0°S/N
Source	Comment	Flux (PgC yr <sup>-1</sup> )	Comment	Flux (PgC yr <sup>1</sup> )	Comment	Flux (PgC yr <sup>-1</sup> )	(PgC yr <sup>-1</sup> )	Comment	Flux (PgC yr <sup>4</sup> )
Present study	Linear combination of sensitivity		$0.90\pm0.26$ Linear combination of sensitivity $-0.11\pm0.05$ Linear combination of sensitivity $-0.25\pm0.05$ $0.51\pm0.24$	$-0.11 \pm 0.05$	Linear combination of sensitivity	$-0.25 \pm 0.05$	$0.51 \pm 0.24$	Partitioning shared with boundaries at 20°S/N	$(0.15 \pm 0.13; 0.20 \pm 0.10; 0.16 \pm 0.08)$
(composite simulated estimate)	simulations to match literature		simulations to match literature		simulations to match literature			Partitioning shared with boundaries at 30°S/N	$(0.13\pm0.13;0.24\pm0.12;0.13\pm0.07)$
	estimates		estimates		estimates				
Regnier et al. (2022)	Mass balance calculation through		$0.80 \pm 0.30$ From literature	$\textbf{-0.04} \pm 0.02$	-0.04 $\pm$ 0.02 From literature	$-0.13\pm0.02$	$-0.13 \pm 0.02$ $0.65 \pm 0.30^{a}$	Using Lacroix et al. (2020) partitioning;	(0.09; 0.42; 0.14)
	the land-to-ocean aquatic							e.g. Friedlingstein et al. (2023, 2024)	
	continuum loop							Using Aumont et al. (2001) partitioning;	(0.32; 0.16; 0.17)
								e.g. Friedlingstein et al. (2022b)	
Friedlingstein et al. (2020, 2022a) Mean of Murnane et al. (1999)	Mean of Murnane et al. (1999)	0.74	Mean of Resplandy et al. (2018) -0.05	-0.05	Mean of Resplandy et al. (2018) -0.08	-0.08	0.61	Using Aumont et al. (2001) partitioning;	(0.30; 0.15; 0.16)
	and Jacobson et al. (2007)		and Jacobson et al. (2007)		and Jacobson et al. (2007)			e.g. Friedlingstein et al. (2020, 2022a)	
Lacroix et al. (2020)	From a hydrological discharge	09'0	From an ocean biogeochemistry	-0.19	From an ocean biogeochemistry	-0.58	0.23 <sup>b</sup>	Partitioning at the equator between southern	(0,11; 0.12)
	model		model		model			and northern hemispheres	
Resplandy et al. (2018)	Scaled-up river flux of	$0.78\pm0.41$					$0.78 \pm 0.41$	Using IPSL GOBM partitioning;	(0.38; 0.19; 0.20)
	Jacobson et al. (2007) from heat							e.g. Le Quéré et al. (2018b) and Friedlingstein et al. (2019)	
	based constraint							Using Jacobson et al. (2007) partitionning;	$(0.03\pm0.02;0.38\pm0.19;0.36\pm0.17)$
								e.g. Resplandy et al. (2018)	
Jacobson et al. (2007)6	From global erosion model	0.71	From literature	-0.10	From literature	-0.16	$0.45 \pm 0.18^{d}$	Partitioning shared in Resplandy et al. (2018)	$(0.02\pm0.01;0.22\pm0.11;0.21\pm0.10)$
Aumont et al. (2001)	From a global erosion model	0.81			From an ocean biogeochemistry	-0.2	190		(0.30; 0.15; 0.16)
					model to conserve the global				
					Alk inventory				

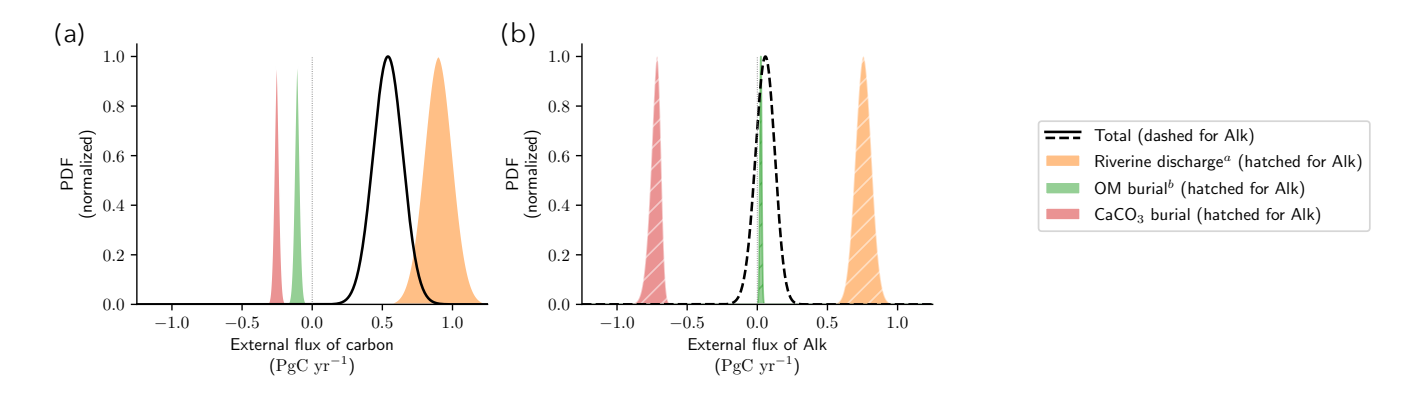


**Figure E1.** Literature-based estimates of the riverine discharge<sup>a</sup>, OM burial<sup>b</sup> and CaCO<sub>3</sub> burial, with their associated uncertainties/extremes through normalized PDFs.

980

985

990

## E2 Inter-hemispheric Reassessing the regional distribution of the riverine/burial-driven air-sea carbon fluxgradient

We share additional insights regarding the inter-hemispheric air-sea carbon flux gradient, which is crucial for the global carbon eyele in its connection with the atmosphere and land (e.g. Keeling et al., 1989; Resplandy et al., 2018). It is thus valuable to distinguish in this inter-hemispheric gradient the component associated with the net air-sea carbon flux in both the southern and northern regions (Fig. D1).

Moreover, in order to underscore the importance of the carbon:Alk imbalance resulting from riverine and burial fluxes in shaping this inter-hemispheric air-sea carbon flux gradient, we decompose this gradient into two components accounting for regional imbalances: one associated with carbon and Alk from riverine and burial fluxes (including inventory disequilibria), and another originating from the inter-hemispheric transport of provide a schematic of the practical framework introduced in this manuscript (Sect. 4.2.1), which follows a four-step workflow to construct a composite simulation aligning with the most recent carbon and Alk (see Eq. D7 and Sect. 3.3.2; budgets (Fig. D3). The deviation from this partitioning in the NEMO-PISCES sensitivity simulations is small (less than 0.01 PgC yr<sup>-1</sup>). E2).

Partitioning of the inter-hemispheric air-sea carbon flux gradient from inter-hemispheric carbon:Alk imbalances (supplement to 6b). (a, b) Visual construction of the inter-hemispheric air-sea carbon flux gradient resulting from regional carbon:Alk imbalances due to (a) riverine and burial fluxes (including inventory disequilibria), and (b) inter-hemispheric transport, defining the values used in Fig. 6b. The reference was set on the simulation without riverine and burial fluxes (norivbur), so that the combination of the arrows of (a) and (b) results in the inter-hemispheric riverine/burial-driven air-sea carbon flux gradient. (c) Synthetic characterization for the whole set of NEMO-PISCES sensitivity simulations of the inter-hemispheric air-sea carbon flux gradient: with a southern/northern decomposition (as in Fig. D1b), and the partitioning resulting from regional carbon:Alk imbalances due to riverine and burial fluxes (including inventory disequilibria) – constructed in (a) –, and inter-hemispheric transport – constructed in (b).

<sup>&</sup>lt;sup>a</sup>Including groundwater discharge for both carbon and Alk, and anaerobic processes Alk.

<sup>&</sup>lt;sup>b</sup>Including reverse weathering for Alk.

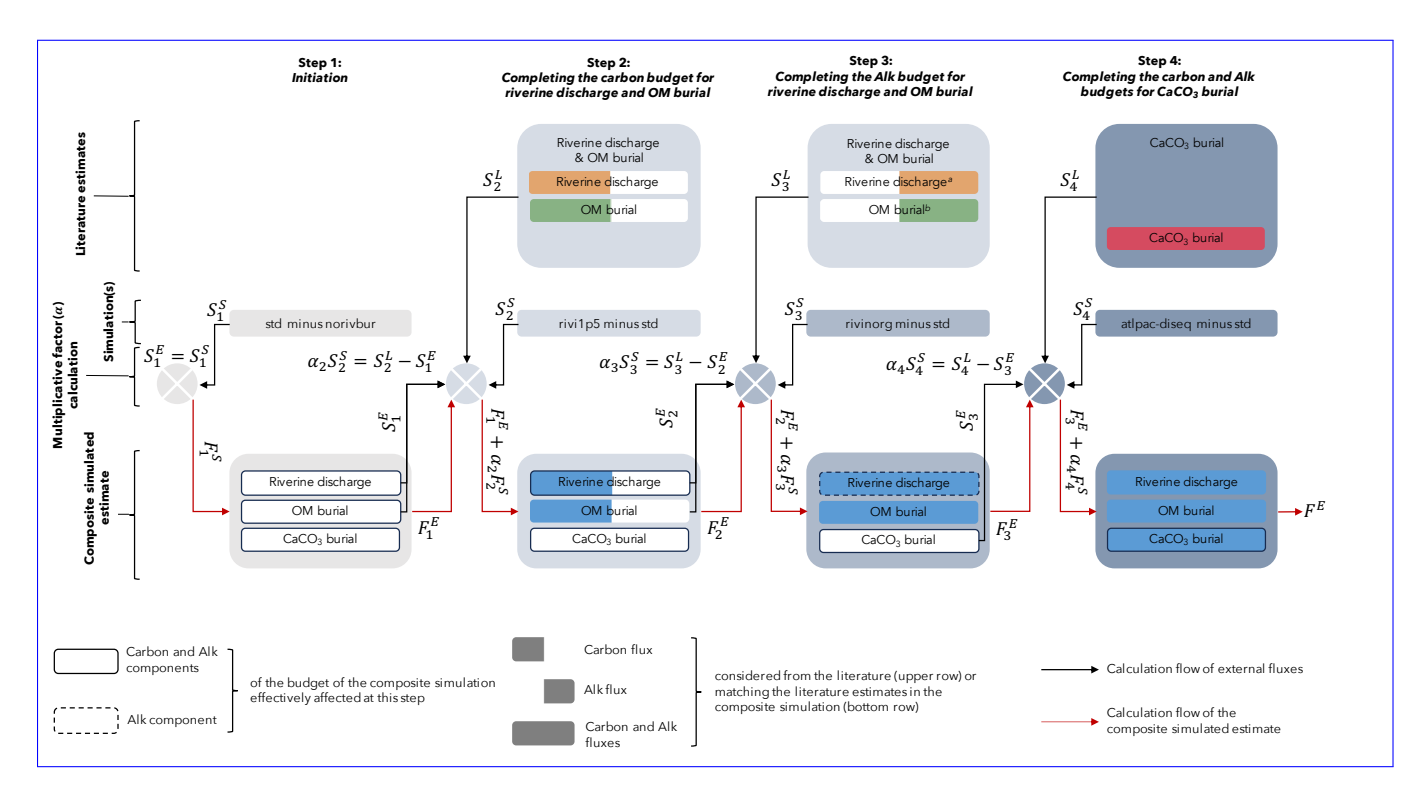
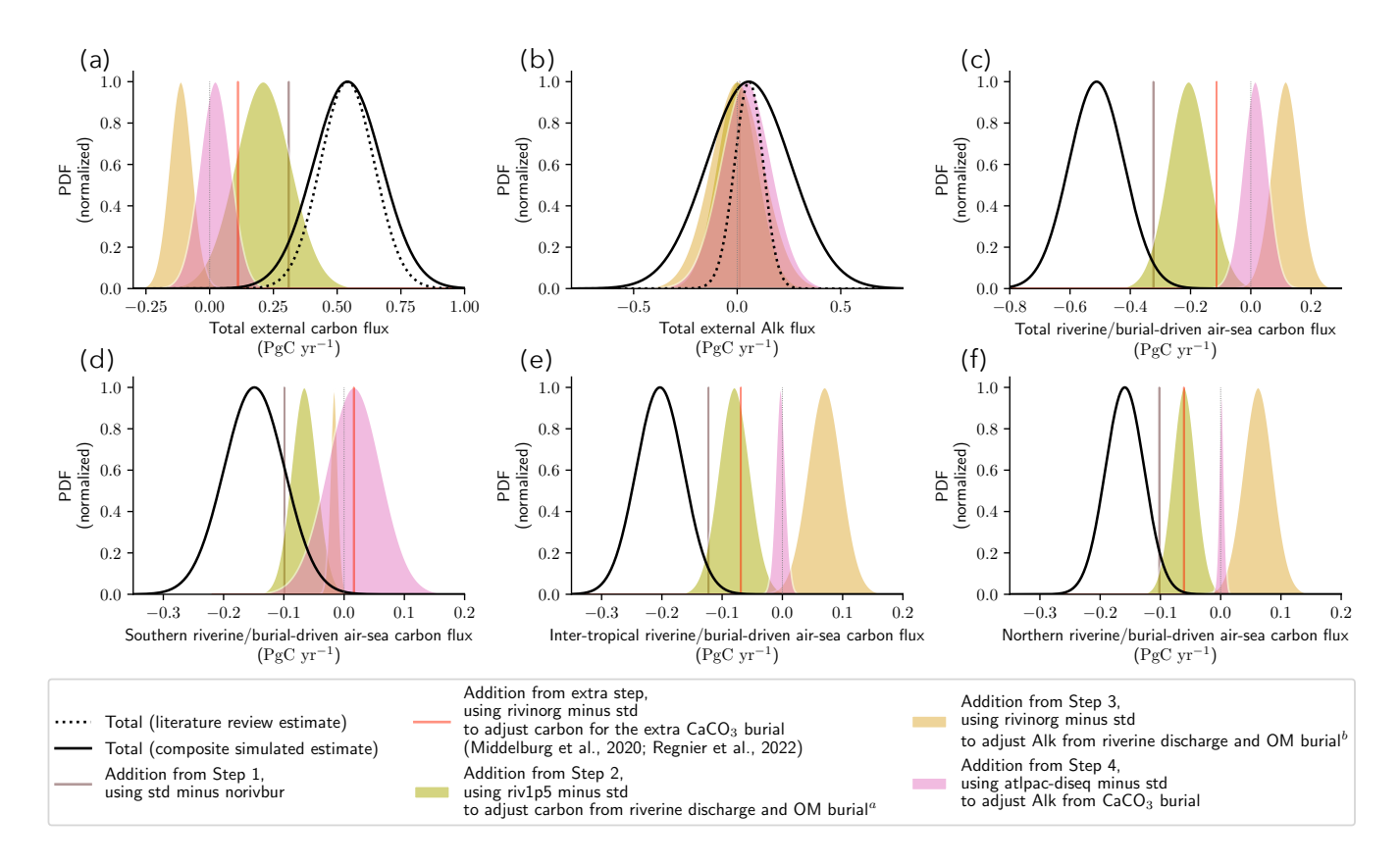


Figure E2. Decomposition Schematic of the inter-hemispheric air-sea carbon flux gradient (supplement four-step workflow to Figconstruct the composite simulation. 2). Decomposition The composite simulated estimate of the inter-hemispheric riverine/burial-driven air-sea carbon flux gradient into the net southern and northen air-sea carbon fluxes for (is built from a ) CMIP6 and GCB, and (b) the NEMO-PISCES linear combination of our sensitivity simulations . Filled contours correspond to match the inter-hemispheric air-sea most recent carbon flux gradient, and Alk budgets (ariverine discharge, OM burial, and CaCO<sub>3</sub> burial) The 15 CMIP6 ESMs (10 GCB GOBMs) are plotted with red squares (orange circles). The black square and circle refer An additional step, equivalent to the CMIP6 and GCB ensemble means. In (b) Step 3 but not shown in this general workflow, secondary axes have been added was necessary to characterize adjust the implied changes for the southern/northern air-land CaCO<sub>3</sub> burial of carbon flux relative to stdin excess (Regnier et al., 2022), if compared to the inter-hemispheric gradient is considered as well-represented values accounted for Alk (Middelburg et al., 2020). ThenIn the schematic, a decrease in the net sourthern (northern) air-sea carbon flux relative to std entails an increase exponents indicate the source of each variable/parameter: E denotes the same magnitude in the net southern (northern) air-land carbon flux relative composite simulated estimate, S refers to stdthe various sensitivity simulations, and conversely L stands for literature estimates.



**Figure E3.** Components of the composite simulated estimate (supplement to Fig. 7). Each of the components represents the elements added at the different stages of the composite simulated estimate construction process (Steps 1, 2, 3, 4, and the extra step; Fig. E2). (a, b) Decomposition of the composite simulated estimate PDF associated with the total (a) carbon and (b) Alk external fluxes. (c, d, e, f) Characterization of the riverine/burial air-sea carbon flux in the composite simulated estimate, showing the various components for (c) the total value, as well as the (d) southern, (e) inter-tropical, and (f) northern regions. The black solid lines represent the total values for the composite simulated estimate, while the black dotted lines (a, b) correspond to the total carbon and Alk external fluxes from literature estimates (Fig. E1).

#### E3 Composite simulated estimate

995

We In addition, we also share (Fig. E3) the various components of the composite simulated estimate creation process as described in Sect. 4.2.1, and the results of which are presented in Sect. 4.2.2 (see Fig. 7 and Table E2).

Code availability. NEMO is released under the terms of the CeCILL licence. The standard NEMO-PISCES version (PISCESv2; Aumont et al., 2015) slightly modified in this study (see Sect. 2.2.1) is accessible through https://www.nemo-ocean.eu (last access: January 2025). The other NEMO-PISCES versions are available on request from the corresponding author.

Data availability. All the CMIP ensemble data were available on at least one of the Earth System Grid Federation (ESGF) nodes https://esgf-node.ipsl.upmc.fr/projects/esgf-ipsl/ (last access: January 2025). The 2024 release of GCB data is currently available via their SFTP server upon request but is expected to become directly accessible soon through their data browser platform https://mdosullivan.github.io/GCB/ (last access: January 2025). The code of all the various configurations of NEMO-PISCES used in this study is accessible on Zenodo (https://doi.org/10.5281/zenodo.8421951), as well as two supplementary figures, S1 and S2 (https://doi.org/10.5281/zenodo.8421898).

Author contributions. This work is in the framework of the OMIP-BGC group, which contributed collectively to this study through the organization and execution of the CMIP exercises and the sharing of simulation outputs. AP: conceptualization, investigation, methodology, formal analysis, visualization, writing – original draft preparation – and project administration. LB and LK: supervision, funding acquisition, methodology, resources, conceptualization, and writing – original draft preparation.

1010 Competing interests. The contact author has declared that none of the authors has any competing interests.

1005

1015

1020

*Disclaimer.* This article reflects only the authors' views; the funding agencies and their executive agencies are not responsible for any use that may be made of the information that the article contains.

Acknowledgements. We would like to express our gratitude to Pierre Regnier and an anonymous reviewer for their careful and constructive review which greatly contributed to improving the quality and clarity of our work. We are also grateful to Jack Middelburg for being the associate editor. Thanks to Olivier Aumont and Olivier Sulpis for the discussions we had, respectively, regarding the evolution of the riverine/burial-driven air-sea carbon flux assessment, and the burial of CaCO<sub>3</sub>, as well as the global Alk inventory. We are grateful to the World Climate Research Programme's Working Group on Coupled Modelling, which is responsible for the CMIP exercises. For CMIP, the U.S. Department of Energy's Program for Climate Model Diagnosis and Intercomparison provided coordinating support and led the development of software infrastructure in partnership with the Global Organization for Earth System Science Portals. This study benefited from the ESPRI (Ensemble de Services Pour la Recherche à l'IPSL) computing and data centre (https://mesocentre.ipsl.fr, last access: January 2025), which is supported by CNRS, Sorbonne Université, École Polytechnique, and CNES and through national and international grants. We are grateful to the GCP for leading such a community effort around the carbon cycle, especially with yearly inter-model comparison exercises. We thank the PISCES community for actively using, developing, sharing knowledge around the marine biogeochemical model NEMO-PISCES (https://www.pisces-community.org, last access: January 2025). I would like to express my appreciation to the CEA (Commissariat

1025 à l'Énergie Atomique et aux énergies alternatives) and James C. Orr, the project coordinator of 'gen0040', for granting us access to the TGCC (*Très Grand Centre de Calcul*), particularly allowing us to conduct all our simulations on their 'Irène Rome' machine. Finally, we are also grateful to the administrative and technical staff at École Normale Supérieure/PSL.

Financial supports. Alban Planchat, Laurent Bopp and Lester Kwiatkowski are grateful to the ENS-Chanel research chair.

### References

- 1030 Aumont, O., Orr, J. C., Monfray, P., Ludwig, W., Amiotte-Suchet, P., and Probst, J.-L.: Riverine-driven interhemispheric transport of carbon, Global Biogeochemical Cycles, 15, 393–405, https://doi.org/10.1029/1999GB001238, \_eprint: https://onlinelibrary.wiley.com/doi/pdf/10.1029/1999GB001238, 2001.
  - Aumont, O., Ethé, C., Tagliabue, A., Bopp, L., and Gehlen, M.: PISCES-v2: an ocean biogeochemical model for carbon and ecosystem studies, Geoscientific Model Development, 8, 2465–2513, https://doi.org/10.5194/gmd-8-2465-2015, 2015.
- Bopp, L., Aumont, O., Kwiatkowski, L., Clerc, C., Dupont, L., Ethé, C., Gorgues, T., Séférian, R., and Tagliabue, A.: Diazotrophy as a key driver of the response of marine net primary productivity to climate change, Biogeosciences, 19, 4267–4285, https://doi.org/10.5194/bg-19-4267-2022, 2022.
  - Boucher, O., Servonnat, J., Albright, A. L., Aumont, O., Balkanski, Y., Bastrikov, V., Bekki, S., Bonnet, R., Bony, S., Bopp, L., Braconnot, P., Brockmann, P., Cadule, P., Caubel, A., Cheruy, F., Codron, F., Cozic, A., Cugnet, D., D'Andrea, F., Davini, P., Lavergne, C., Denvil, S.,
- Deshayes, J., Devilliers, M., Ducharne, A., Dufresne, J., Dupont, E., Éthé, C., Fairhead, L., Falletti, L., Flavoni, S., Foujols, M., Gardoll, S., Gastineau, G., Ghattas, J., Grandpeix, J., Guenet, B., Guez, E., L., Guilyardi, E., Guimberteau, M., Hauglustaine, D., Hourdin, F., Idelkadi, A., Joussaume, S., Kageyama, M., Khodri, M., Krinner, G., Lebas, N., Levavasseur, G., Lévy, C., Li, L., Lott, F., Lurton, T., Luyssaert, S., Madec, G., Madeleine, J., Maignan, F., Marchand, M., Marti, O., Mellul, L., Meurdesoif, Y., Mignot, J., Musat, I., Ottlé, C., Peylin, P., Planton, Y., Polcher, J., Rio, C., Rochetin, N., Rousset, C., Sepulchre, P., Sima, A., Swingedouw, D., Thiéblemont, R., Traore,
- A. K., Vancoppenolle, M., Vial, J., Vialard, J., Viovy, N., and Vuichard, N.: Presentation and Evaluation of the IPSL-CM6A-LR Climate Model, Journal of Advances in Modeling Earth Systems, 12, https://doi.org/10.1029/2019MS002010, 2020.
  - Boudreau, B. P., Middelburg, J. J., and Luo, Y.: The role of calcification in carbonate compensation, Nature Geoscience, 11, 894–900, https://doi.org/10.1038/s41561-018-0259-5, 2018.
- Canadell, J., Monteiro, P., Costa, M., Cotrim da Cunha, L., Cox, P., Eliseev, A., Henson, S., Ishii, M., Jaccard, S., Koven, C., Lohila,
  A., Patra, P., Piao, S., Rogelj, J., Syampungani, S., Zaehle, S., and Zickfeld, K.: Global Carbon and other Biogeochemical Cycles
  and Feedbacks, in: Climate Change 2021: The Physical Science Basis. Contribution of Working Group I to the Sixth Assessment Report of the Intergovernmental Panel on Climate Change, edited by Masson-Delmotte, V., Zhai, P., Pirani, A., Connors, S., Péan, C.,
  Berger, S., Caud, N., Chen, Y., Goldfarb, L., Gomis, M., Huang, M., Leitzell, K., Lonnoy, E., Matthews, J., Maycock, T., Waterfield, T.,
  Yelekçi, O., Yu, R., and Zhou, B., pp. 673–816, Cambridge University Press, Cambridge, United Kingdom and New York, NY, USA,
  https://doi.org/10.1017/9781009157896.007, type: Book Section, 2021.
  - Cartapanis, O., Galbraith, E. D., Bianchi, D., and Jaccard, S. L.: Carbon burial in deep-sea sediment and implications for oceanic inventories of carbon and alkalinity over the last glacial cycle, Climate of the Past, 14, 1819–1850, https://doi.org/10.5194/cp-14-1819-2018, publisher: Copernicus GmbH, 2018.
- Crisp, D., Dolman, H., Tanhua, T., McKinley, G. A., Hauck, J., Bastos, A., Sitch, S., Eggleston, S., and Aich, V.: How Well Do We Understand the Land-Ocean-Atmosphere Carbon Cycle?, Reviews of Geophysics, 60, e2021RG000736, https://doi.org/10.1029/2021RG000736, publisher: John Wiley & Sons, Ltd, 2022.
  - DeVries, T., Le Quéré, C., Andrews, O., Berthet, S., Hauck, J., Ilyina, T., Landschützer, P., Lenton, A., Lima, I. D., Nowicki, M., Schwinger, J., and Séférian, R.: Decadal trends in the ocean carbon sink, Proceedings of the National Academy of Sciences, 116, 11646–11651, https://doi.org/10.1073/pnas.1900371116, publisher: Proceedings of the National Academy of Sciences, 2019.

- DeVries, T., Yamamoto, K., Wanninkhof, R., Gruber, N., Hauck, J., Müller, J. D., Bopp, L., Carroll, D., Carter, B., Chau, T.-T.-T., Doney, S. C., Gehlen, M., Gloege, L., Gregor, L., Henson, S., Kim, J. H., Iida, Y., Ilyina, T., Landschützer, P., Le Quéré, C., Munro, D., Nissen, C., Patara, L., Pérez, F. F., Resplandy, L., Rodgers, K. B., Schwinger, J., Séférian, R., Sicardi, V., Terhaar, J., Triñanes, J., Tsujino, H., Watson, A., Yasunaka, S., and Zeng, J.: Magnitude, Trends, and Variability of the Global Ocean Carbon Sink From 1985 to 2018, Global Biogeochemical Cycles, 37, e2023GB007780, https://doi.org/10.1029/2023GB007780, publisher: John Wiley & Sons, Ltd, 2023.
- 1070 Dong, Y., Bakker, D. C. E., and Landschützer, P.: Accuracy of Ocean CO2 Uptake Estimates at a Risk by a Reduction in the Data Collection, Geophysical Research Letters, 2024.
  - Dufresne, J.-L., Foujols, M.-A., Denvil, S., Caubel, A., Marti, O., Aumont, O., Balkanski, Y., Bekki, S., Bellenger, H., Benshila, R., Bony, S., Bopp, L., Braconnot, P., Brockmann, P., Cadule, P., Cheruy, F., Codron, F., Cozic, A., Cugnet, D., de Noblet, N., Duvel, J.-P., Ethé, C., Fairhead, L., Fichefet, T., Flavoni, S., Friedlingstein, P., Grandpeix, J.-Y., Guez, L., Guilyardi, E., Hauglustaine, D., Hourdin, F., Idelkadi,
- A., Ghattas, J., Joussaume, S., Kageyama, M., Krinner, G., Labetoulle, S., Lahellec, A., Lefebvre, M.-P., Lefevre, F., Levy, C., Li, Z. X., Lloyd, J., Lott, F., Madec, G., Mancip, M., Marchand, M., Masson, S., Meurdesoif, Y., Mignot, J., Musat, I., Parouty, S., Polcher, J., Rio, C., Schulz, M., Swingedouw, D., Szopa, S., Talandier, C., Terray, P., Viovy, N., and Vuichard, N.: Climate change projections using the IPSL-CM5 Earth System Model: from CMIP3 to CMIP5, Climate Dynamics, 40, 2123–2165, https://doi.org/10.1007/s00382-012-1636-1, 2013.
- Eyring, V., Bony, S., Meehl, G. A., Senior, C. A., Stevens, B., Stouffer, R. J., and Taylor, K. E.: Overview of the Coupled Model Intercomparison Project Phase 6 (CMIP6) experimental design and organization, Geoscientific Model Development, 9, 1937–1958, https://doi.org/10.5194/gmd-9-1937-2016, 2016.

- Ford, D. J., Blannin, J., Watts, J., Watson, A. J., Landschützer, P., Jersild, A., and Shutler, J. D.: A Comprehensive Analysis of Air-Sea CO2 Flux Uncertainties Constructed From Surface Ocean Data Products, Global Biogeochemical Cycles, 38, e2024GB008188, https://doi.org/10.1029/2024GB008188, eprint: https://onlinelibrary.wiley.com/doi/pdf/10.1029/2024GB008188, 2024.
- Friedlingstein, P., Jones, M. W., O'Sullivan, M., Andrew, R. M., Hauck, J., Peters, G. P., Peters, W., Pongratz, J., Sitch, S., Le Quéré, C., Bakker, D. C. E., Canadell, J. G., Ciais, P., Jackson, R. B., Anthoni, P., Barbero, L., Bastos, A., Bastrikov, V., Becker, M., Bopp, L., Buitenhuis, E., Chandra, N., Chevallier, F., Chini, L. P., Currie, K. I., Feely, R. A., Gehlen, M., Gilfillan, D., Gkritzalis, T., Goll, D. S., Gruber, N., Gutekunst, S., Harris, I., Haverd, V., Houghton, R. A., Hurtt, G., Ilyina, T., Jain, A. K., Joetzjer, E., Kaplan, J. O., Kato, E.,
- Klein Goldewijk, K., Korsbakken, J. I., Landschützer, P., Lauvset, S. K., Lefèvre, N., Lenton, A., Lienert, S., Lombardozzi, D., Marland, G., McGuire, P. C., Melton, J. R., Metzl, N., Munro, D. R., Nabel, J. E. M. S., Nakaoka, S.-I., Neill, C., Omar, A. M., Ono, T., Peregon, A., Pierrot, D., Poulter, B., Rehder, G., Resplandy, L., Robertson, E., Rödenbeck, C., Séférian, R., Schwinger, J., Smith, N., Tans, P. P., Tian, H., Tilbrook, B., Tubiello, F. N., van der Werf, G. R., Wiltshire, A. J., and Zaehle, S.: Global Carbon Budget 2019, Earth System Science Data, 11, 1783–1838, https://doi.org/10.5194/essd-11-1783-2019, publisher: Copernicus GmbH, 2019.
- Friedlingstein, P., O'Sullivan, M., Jones, M. W., Andrew, R. M., Hauck, J., Olsen, A., Peters, G. P., Peters, W., Pongratz, J., Sitch, S., Le Quéré, C., Canadell, J. G., Ciais, P., Jackson, R. B., Alin, S., Aragão, L. E. O. C., Arneth, A., Arora, V., Bates, N. R., Becker, M., Benoit-Cattin, A., Bittig, H. C., Bopp, L., Bultan, S., Chandra, N., Chevallier, F., Chini, L. P., Evans, W., Florentie, L., Forster, P. M., Gasser, T., Gehlen, M., Gilfillan, D., Gkritzalis, T., Gregor, L., Gruber, N., Harris, I., Hartung, K., Haverd, V., Houghton, R. A., Ilyina, T., Jain, A. K., Joetzjer, E., Kadono, K., Kato, E., Kitidis, V., Korsbakken, J. I., Landschützer, P., Lefèvre, N., Lenton, A., Lienert, S.,
- Liu, Z., Lombardozzi, D., Marland, G., Metzl, N., Munro, D. R., Nabel, J. E. M. S., Nakaoka, S.-I., Niwa, Y., O'Brien, K., Ono, T., Palmer, P. I., Pierrot, D., Poulter, B., Resplandy, L., Robertson, E., Rödenbeck, C., Schwinger, J., Séférian, R., Skjelvan, I., Smith, A. J. P., Sutton, A. J., Tanhua, T., Tans, P. P., Tian, H., Tilbrook, B., van der Werf, G., Vuichard, N., Walker, A. P., Wanninkhof, R., Watson, A. J.,

- Willis, D., Wiltshire, A. J., Yuan, W., Yue, X., and Zaehle, S.: Global Carbon Budget 2020, Earth System Science Data, 12, 3269–3340, https://doi.org/10.5194/essd-12-3269-2020, publisher: Copernicus GmbH, 2020.
- 1105 Friedlingstein, P., Jones, M. W., O'Sullivan, M., Andrew, R. M., Bakker, D. C. E., Hauck, J., Le Quéré, C., Peters, G. P., Peters, W., Pongratz, J., Sitch, S., Canadell, J. G., Ciais, P., Jackson, R. B., Alin, S. R., Anthoni, P., Bates, N. R., Becker, M., Bellouin, N., Bopp, L., Chau, T. T. T., Chevallier, F., Chini, L. P., Cronin, M., Currie, K. I., Decharme, B., Djeutchouang, L. M., Dou, X., Evans, W., Feely, R. A., Feng, L., Gasser, T., Gilfillan, D., Gkritzalis, T., Grassi, G., Gregor, L., Gruber, N., Gürses, , Harris, I., Houghton, R. A., Hurtt, G. C., Iida, Y., Ilyina, T., Luijkx, I. T., Jain, A., Jones, S. D., Kato, E., Kennedy, D., Klein Goldewijk, K., Knauer, J., Korsbakken, J. I., Körtzinger,
- A., Landschützer, P., Lauvset, S. K., Lefèvre, N., Lienert, S., Liu, J., Marland, G., McGuire, P. C., Melton, J. R., Munro, D. R., Nabel, J. E. M. S., Nakaoka, S.-I., Niwa, Y., Ono, T., Pierrot, D., Poulter, B., Rehder, G., Resplandy, L., Robertson, E., Rödenbeck, C., Rosan, T. M., Schwinger, J., Schwingshackl, C., Séférian, R., Sutton, A. J., Sweeney, C., Tanhua, T., Tans, P. P., Tian, H., Tilbrook, B., Tubiello, F., van der Werf, G. R., Vuichard, N., Wada, C., Wanninkhof, R., Watson, A. J., Willis, D., Wiltshire, A. J., Yuan, W., Yue, C., Yue, X., Zaehle, S., and Zeng, J.: Global Carbon Budget 2021, Earth System Science Data, 14, 1917–2005, https://doi.org/10.5194/essd-14-1917-2022, publisher: Copernicus GmbH, 2022a.
  - Friedlingstein, P., O'Sullivan, M., Jones, M. W., Andrew, R. M., Gregor, L., Hauck, J., Le Quéré, C., Luijkx, I. T., Olsen, A., Peters, G. P., Peters, W., Pongratz, J., Schwingshackl, C., Sitch, S., Canadell, J. G., Ciais, P., Jackson, R. B., Alin, S. R., Alkama, R., Arneth, A., Arora, V. K., Bates, N. R., Becker, M., Bellouin, N., Bittig, H. C., Bopp, L., Chevallier, F., Chini, L. P., Cronin, M., Evans, W., Falk, S., Feely, R. A., Gasser, T., Gehlen, M., Gkritzalis, T., Gloege, L., Grassi, G., Gruber, N., Gürses, Harris, I., Hefner, M., Houghton, R. A.,
- Hurtt, G. C., Iida, Y., Ilyina, T., Jain, A. K., Jersild, A., Kadono, K., Kato, E., Kennedy, D., Klein Goldewijk, K., Knauer, J., Korsbakken, J. I., Landschützer, P., Lefèvre, N., Lindsay, K., Liu, J., Liu, Z., Marland, G., Mayot, N., McGrath, M. J., Metzl, N., Monacci, N. M., Munro, D. R., Nakaoka, S.-I., Niwa, Y., O'Brien, K., Ono, T., Palmer, P. I., Pan, N., Pierrot, D., Pocock, K., Poulter, B., Resplandy, L., Robertson, E., Rödenbeck, C., Rodriguez, C., Rosan, T. M., Schwinger, J., Séférian, R., Shutler, J. D., Skjelvan, I., Steinhoff, T., Sun, Q., Sutton, A. J., Sweeney, C., Takao, S., Tanhua, T., Tans, P. P., Tian, X., Tian, H., Tilbrook, B., Tsujino, H., Tubiello, F., van der Werf,
- G. R., Walker, A. P., Wanninkhof, R., Whitehead, C., Willstrand Wranne, A., Wright, R., Yuan, W., Yue, C., Yue, X., Zaehle, S., Zeng, J., and Zheng, B.: Global Carbon Budget 2022, Earth System Science Data, 14, 4811–4900, https://doi.org/10.5194/essd-14-4811-2022, publisher: Copernicus GmbH, 2022b.
  - Friedlingstein, P., O'Sullivan, M., Jones, M. W., Andrew, R. M., Bakker, D. C. E., Hauck, J., Landschützer, P., Le Quéré, C., Luijkx, I. T., Peters, G. P., Peters, W., Pongratz, J., Schwingshackl, C., Sitch, S., Canadell, J. G., Ciais, P., Jackson, R. B., Alin, S. R., Anthoni, P.,
- Barbero, L., Bates, N. R., Becker, M., Bellouin, N., Decharme, B., Bopp, L., Brasika, I. B. M., Cadule, P., Chamberlain, M. A., Chandra, N., Chau, T.-T.-T., Chevallier, F., Chini, L. P., Cronin, M., Dou, X., Enyo, K., Evans, W., Falk, S., Feely, R. A., Feng, L., Ford, D. J., Gasser, T., Ghattas, J., Gkritzalis, T., Grassi, G., Gregor, L., Gruber, N., Gürses, , Harris, I., Hefner, M., Heinke, J., Houghton, R. A., Hurtt, G. C., Iida, Y., Ilyina, T., Jacobson, A. R., Jain, A., Jarníková, T., Jersild, A., Jiang, F., Jin, Z., Joos, F., Kato, E., Keeling, R. F., Kennedy, D., Klein Goldewijk, K., Knauer, J., Korsbakken, J. I., Körtzinger, A., Lan, X., Lefèvre, N., Li, H., Liu, J., Liu, Z., Ma, L., Marland, G., Mayot,
- N., McGuire, P. C., McKinley, G. A., Meyer, G., Morgan, E. J., Munro, D. R., Nakaoka, S.-I., Niwa, Y., O'Brien, K. M., Olsen, A., Omar, A. M., Ono, T., Paulsen, M., Pierrot, D., Pocock, K., Poulter, B., Powis, C. M., Rehder, G., Resplandy, L., Robertson, E., Rödenbeck, C., Rosan, T. M., Schwinger, J., Séférian, R., Smallman, T. L., Smith, S. M., Sospedra-Alfonso, R., Sun, Q., Sutton, A. J., Sweeney, C., Takao, S., Tans, P. P., Tian, H., Tilbrook, B., Tsujino, H., Tubiello, F., van der Werf, G. R., van Ooijen, E., Wanninkhof, R., Watanabe, M., Wimart-Rousseau, C., Yang, D., Yang, X., Yuan, W., Yue, X., Zaehle, S., Zeng, J., and Zheng, B.: Global Carbon Budget 2023, Earth
- 1140 System Science Data, 15, 5301–5369, https://doi.org/10.5194/essd-15-5301-2023, publisher: Copernicus GmbH, 2023.

- Friedlingstein, P., O'Sullivan, M., Jones, M. W., Andrew, R. M., Hauck, J., Landschützer, P., Le Quéré, C., Li, H., Luijkx, I. T., Olsen, A., Peters, G. P., Peters, W., Pongratz, J., Schwingshackl, C., Sitch, S., Canadell, J. G., Ciais, P., Jackson, R. B., Alin, S. R., Arneth, A., Arora,
- V., Bates, N. R., Becker, M., Bellouin, N., Berghoff, C. F., Bittig, H. C., Bopp, L., Cadule, P., Campbell, K., Chamberlain, M. A., Chandra,
  - N., Chevallier, F., Chini, L. P., Colligan, T., Decayeux, J., Djeutchouang, L., Dou, X., Duran Rojas, C., Enyo, K., Evans, W., Fay, A.,
- Feely, R. A., Ford, D. J., Foster, A., Gasser, T., Gehlen, M., Gkritzalis, T., Grassi, G., Gregor, L., Gruber, N., Gürses, , Harris, I., Hefner,
- M., Heinke, J., Hurtt, G. C., Iida, Y., Ilyina, T., Jacobson, A. R., Jain, A., Jarníková, T., Jersild, A., Jiang, F., Jin, Z., Kato, E., Keeling,
  - R. F., Klein Goldewijk, K., Knauer, J., Korsbakken, J. I., Lauvset, S. K., Lefèvre, N., Liu, Z., Liu, J., Ma, L., Maksyutov, S., Marland, G.,
    - Mayot, N., McGuire, P., Metzl, N., Monacci, N. M., Morgan, E. J., Nakaoka, S.-I., Neill, C., Niwa, Y., Nützel, T., Olivier, L., Ono, T.,
    - Palmer, P. I., Pierrot, D., Oin, Z., Resplandy, L., Roobaert, A., Rosan, T. M., Rödenbeck, C., Schwinger, J., Smallman, T. L., Smith, S.,
- 1150 Sospedra-Alfonso, R., Steinhoff, T., Sun, Q., Sutton, A. J., Séférian, R., Takao, S., Tatebe, H., Tian, H., Tilbrook, B., Torres, O., Tourigny,
- E., Tsujino, H., Tubiello, F., van der Werf, G., Wanninkhof, R., Wang, X., Yang, D., Yang, X., Yu, Z., Yuan, W., Yue, X., Zaehle, S., Zeng,
  - N., and Zeng, J.: Global Carbon Budget 2024, https://doi.org/10.5194/essd-2024-519, publisher: Copernicus GmbH, 2024.
- Gloor, M., Gruber, N., Sarmiento, J., Sabine, C. L., Feely, R. A., and Rödenbeck, C.: A first estimate of present and preindustrial air-sea CO2 flux patterns based on ocean interior carbon measurements and models, Geophysical Research Letters, 30, 10–1–10–4,
- https://doi.org/10.1029/2002GL015594, eprint: https://onlinelibrary.wilev.com/doi/pdf/10.1029/2002GL015594, 2003,
- Gruber, N., Gloor, M., Mikaloff Fletcher, S. E., Doney, S. C., Dutkiewicz, S., Follows, M. J., Gerber, M., Jacobson, A. R.,
  - Joos, F., Lindsay, K., Menemenlis, D., Mouchet, A., Müller, S. A., Sarmiento, J. L., and Takahashi, T.: Oceanic sources,
    - sinks, and transport of atmospheric CO2, Global Biogeochemical Cycles, 23, https://doi.org/10.1029/2008GB003349, \_eprint:
    - https://onlinelibrary.wiley.com/doi/pdf/10.1029/2008GB003349, 2009.
- 1160 Gruber, N., Bakker, D. C. E., DeVries, T., Gregor, L., Hauck, J., Landschützer, P., McKinley, G. A., and Müller, J. D.: Trends and variability
- in the ocean carbon sink, Nature Reviews Earth & Environment, 4, 119–134, https://doi.org/10.1038/s43017-022-00381-x, 2023.
  - Hain, M. P., Sigman, D. M., and Haug, G. H.: Elemental and Isotopic Proxies of Past Ocean Temperatures, in: Treatise on Geochemistry, pp. 373–397, Elsevier, ISBN 978-0-08-098300-4, https://doi.org/10.1016/B978-0-08-095975-7.00614-8, 2014.
  - Hauck, J., Zeising, M., Le Quéré, C., Gruber, N., Bakker, D. C. E., Bopp, L., Chau, T. T. T., Gürses, , Ilyina, T., Landschützer, P., Lenton,
- 1165 A., Resplandy, L., Rödenbeck, C., Schwinger, J., and Séférian, R.: Consistency and Challenges in the Ocean Carbon Sink Estimate for the
- Global Carbon Budget, Frontiers in Marine Science, 7, https://www.frontiersin.org/article/10.3389/fmars.2020.571720, 2020.
  - Hauck, J., Mayot, N., Gregor, L., Bopp, L., Gehlen, M., Gloege, L., Gruber, N., Gürses, , Iida, Y., Ilyina, T., Jersild, A., Lindsay, K.,
    - Resplandy, L., Rödenbeck, C., Schwinger, J., Seferian, R., Shutler, J., Tsujino, H., Wright, R., and Zeng, J.: Global Carbon Budget
      - 2022, surface ocean fugactiy of CO2 (fCO2) and air-sea CO2 flux of individual Global ocean biogechemical models and surface ocean
- 1170 fCO2-based data-products, https://doi.org/10.5281/zenodo.7273309, 2022.
  - Hauck, J., Nissen, C., Landschützer, P., Rödenbeck, C., Bushinsky, S., and Olsen, A.: Sparse observations induce large biases in estimates of
  - the global ocean CO<sub>2</sub> sink; an ocean model subsampling experiment, Philosophical Transactions of the Royal Society A: Mathematical,
    - Physical and Engineering Sciences, 381, 20220 063, https://doi.org/10.1098/rsta.2022.0063, 2023.
- Humphreys, M. P., Daniels, C. J., Wolf-Gladrow, D. A., Tyrrell, T., and Achterberg, E. P.: On the influence of ma-
- 1175 rine biogeochemical processes over CO2 exchange between the atmosphere and ocean, Marine Chemistry, 199, 1-11,
- https://doi.org/10.1016/j.marchem.2017.12.006, 2018.

- Jacobson, A. R., Mikaloff Fletcher, S. E., Gruber, N., Sarmiento, J. L., and Gloor, M.: A joint atmosphere-ocean inversion for surface fluxes of carbon dioxide: 1. Methods and global-scale fluxes, Global Biogeochemical Cycles, 21, https://doi.org/10.1029/2005GB002556, \_eprint: https://onlinelibrary.wiley.com/doi/pdf/10.1029/2005GB002556, 2007.
- 1180 Keeling, C. D., Bacastow, R. B., Carter, A. F., Piper, S. C., Whorf, T. P., Heimann, M., Mook, W. G., and Roeloffzen, H.: A three-dimensional model of atmospheric CO2 transport based on observed winds: 1. Analysis of observational data, in: Aspects of Climate Variability in the Pacific and the Western Americas, pp. 165–236, American Geophysical Union (AGU), ISBN 978-1-118-66428-5, https://doi.org/10.1029/GM055p0165, \_eprint: https://onlinelibrary.wiley.com/doi/pdf/10.1029/GM055p0165, 1989.
- Khatiwala, S., Primeau, F., and Hall, T.: Reconstruction of the history of anthropogenic CO2 concentrations in the ocean, Nature, 462, 346–349, https://doi.org/10.1038/nature08526, 2009.
  - Lacroix, F., Ilyina, T., and Hartmann, J.: Oceanic CO<sub>2</sub> outgassing and biological production hotspots induced by pre-industrial river loads of nutrients and carbon in a global modeling approach, Biogeosciences, 17, 55–88, https://doi.org/10.5194/bg-17-55-2020, publisher: Copernicus GmbH, 2020.
- Landschützer, P., Gruber, N., Bakker, D. C. E., and Schuster, U.: Recent variability of the global ocean carbon sink, Global Biogeochemical

  Cycles, 28, 927–949, https://doi.org/10.1002/2014GB004853, \_eprint: https://onlinelibrary.wiley.com/doi/pdf/10.1002/2014GB004853,

  2014.
  - Landschützer, P., Tanhua, T., Behncke, J., and Keppler, L.: Sailing through the southern seas of air–sea CO<sub>2</sub> flux uncertainty, Philosophical Transactions of the Royal Society A: Mathematical, Physical and Engineering Sciences, 381, 20220064, https://doi.org/10.1098/rsta.2022.0064, 2023.
- Le Quéré, C., Andrew, R. M., Canadell, J. G., Sitch, S., Korsbakken, J. I., Peters, G. P., Manning, A. C., Boden, T. A., Tans, P. P., Houghton, R. A., Keeling, R. F., Alin, S., Andrews, O. D., Anthoni, P., Barbero, L., Bopp, L., Chevallier, F., Chini, L. P., Ciais, P., Currie, K., Delire, C., Doney, S. C., Friedlingstein, P., Gkritzalis, T., Harris, I., Hauck, J., Haverd, V., Hoppema, M., Klein Goldewijk, K., Jain, A. K., Kato, E., Körtzinger, A., Landschützer, P., Lefèvre, N., Lenton, A., Lienert, S., Lombardozzi, D., Melton, J. R., Metzl, N., Millero, F., Monteiro, P. M. S., Munro, D. R., Nabel, J. E. M. S., Nakaoka, S.-i., O'Brien, K., Olsen, A., Omar, A. M., Ono, T., Pierrot, D., Poulter,
- B., Rödenbeck, C., Salisbury, J., Schuster, U., Schwinger, J., Séférian, R., Skjelvan, I., Stocker, B. D., Sutton, A. J., Takahashi, T., Tian, H., Tilbrook, B., van der Laan-Luijkx, I. T., van der Werf, G. R., Viovy, N., Walker, A. P., Wiltshire, A. J., and Zaehle, S.: Global Carbon Budget 2016, Earth System Science Data, 8, 605–649, https://doi.org/10.5194/essd-8-605-2016, publisher: Copernicus GmbH, 2016.
  - Le Quéré, C., Andrew, R. M., Friedlingstein, P., Sitch, S., Hauck, J., Pongratz, J., Pickers, P. A., Korsbakken, J. I., Peters, G. P., Canadell, J. G., Arneth, A., Arora, V. K., Barbero, L., Bastos, A., Bopp, L., Chevallier, F., Chini, L. P., Ciais, P., Doney, S. C., Gkritzalis, T., Goll,
- D. S., Harris, I., Haverd, V., Hoffman, F. M., Hoppema, M., Houghton, R. A., Hurtt, G., Ilyina, T., Jain, A. K., Johannessen, T., Jones, C. D., Kato, E., Keeling, R. F., Goldewijk, K. K., Landschützer, P., Lefèvre, N., Lienert, S., Liu, Z., Lombardozzi, D., Metzl, N., Munro, D. R., Nabel, J. E. M. S., Nakaoka, S.-i., Neill, C., Olsen, A., Ono, T., Patra, P., Peregon, A., Peters, W., Peylin, P., Pfeil, B., Pierrot, D., Poulter, B., Rehder, G., Resplandy, L., Robertson, E., Rocher, M., Rödenbeck, C., Schuster, U., Schwinger, J., Séférian, R., Skjelvan, I., Steinhoff, T., Sutton, A., Tans, P. P., Tian, H., Tilbrook, B., Tubiello, F. N., van der Laan-Luijkx, I. T., van der Werf, G. R., Viovy,
- N., Walker, A. P., Wiltshire, A. J., Wright, R., Zaehle, S., and Zheng, B.: Global Carbon Budget 2018, Earth System Science Data, 10, 2141–2194, https://doi.org/10.5194/essd-10-2141-2018, publisher: Copernicus GmbH, 2018a.
  - Le Quéré, C., Andrew, R. M., Friedlingstein, P., Sitch, S., Pongratz, J., Manning, A. C., Korsbakken, J. I., Peters, G. P., Canadell, J. G., Jackson, R. B., Boden, T. A., Tans, P. P., Andrews, O. D., Arora, V. K., Bakker, D. C. E., Barbero, L., Becker, M., Betts, R. A., Bopp, L., Chevallier, F., Chini, L. P., Ciais, P., Cosca, C. E., Cross, J., Currie, K., Gasser, T., Harris, I., Hauck, J., Haverd, V., Houghton, R. A.,

- Hunt, C. W., Hurtt, G., Ilyina, T., Jain, A. K., Kato, E., Kautz, M., Keeling, R. F., Klein Goldewijk, K., Körtzinger, A., Landschützer, P., Lefèvre, N., Lenton, A., Lienert, S., Lima, I., Lombardozzi, D., Metzl, N., Millero, F., Monteiro, P. M. S., Munro, D. R., Nabel, J. E. M. S., Nakaoka, S.-i., Nojiri, Y., Padin, X. A., Peregon, A., Pfeil, B., Pierrot, D., Poulter, B., Rehder, G., Reimer, J., Rödenbeck, C., Schwinger, J., Séférian, R., Skjelvan, I., Stocker, B. D., Tian, H., Tilbrook, B., Tubiello, F. N., van der Laan-Luijkx, I. T., van der Werf, G. R., van Heuven, S., Viovy, N., Vuichard, N., Walker, A. P., Watson, A. J., Wiltshire, A. J., Zaehle, S., and Zhu, D.: Global Carbon Budget 2017,
  Earth System Science Data, 10, 405–448, https://doi.org/10.5194/essd-10-405-2018, publisher: Copernicus GmbH, 2018b.
  - Li, M., Peng, C., Wang, M., Xue, W., Zhang, K., Wang, K., Shi, G., and Zhu, Q.: The carbon flux of global rivers: A re-evaluation of amount and spatial patterns, Ecological Indicators, 80, 40–51, https://doi.org/10.1016/j.ecolind.2017.04.049, 2017.
  - Ludwig, W., Amiotte Suchet, P., and Probst, J.-L.: River discharges of carbon to the world's oceans: determining local inputs of alkalinity and of dissolved and particulate organic carbon, Sciences de la terre et des planètes (Comptes rendus de l'Académie des sciences), t. 323, 1007–1014, https://oatao.univ-toulouse.fr/3498/, publisher: Gauthier-Villars, 1996.

1250

- Mayot, N., Le Quéré, C., Rödenbeck, C., Bernardello, R., Bopp, L., Djeutchouang, L. M., Gehlen, M., Gregor, L., Gruber, N., Hauck, J., Iida, Y., Ilyina, T., Keeling, R. F., Landschützer, P., Manning, A. C., Patara, L., Resplandy, L., Schwinger, J., Séférian, R., Watson, A. J., Wright, R. M., and Zeng, J.: Climate-driven variability of the Southern Ocean CO<sub>2</sub> sink, Philosophical Transactions of the Royal Society A: Mathematical, Physical and Engineering Sciences, 381, 20220055, https://doi.org/10.1098/rsta.2022.0055, 2023.
- Mayot, N., Buitenhuis, E. T., Wright, R. M., Hauck, J., Bakker, D. C. E., and Le Quéré, C.: Constraining the trend in the ocean CO2 sink during 2000–2022, Nature Communications, 15, 8429, https://doi.org/10.1038/s41467-024-52641-7, 2024.
  - Middelburg, J. J., Soetaert, K., and Hagens, M.: Ocean Alkalinity, Buffering and Biogeochemical Processes, Reviews of Geophysics, 58, https://doi.org/10.1029/2019RG000681, 2020.
- Mikaloff Fletcher, S. E., Gruber, N., Jacobson, A. R., Gloor, M., Doney, S. C., Dutkiewicz, S., Gerber, M., Follows, M., Joos, F., Lindsay, K., Menemenlis, D., Mouchet, A., Müller, S. A., and Sarmiento, J. L.: Inverse estimates of the oceanic sources and sinks of natural CO2 and the implied oceanic carbon transport, Global Biogeochemical Cycles, 21, https://doi.org/10.1029/2006GB002751, \_eprint: https://onlinelibrary.wiley.com/doi/pdf/10.1029/2006GB002751, 2007.
  - Milliman, J. D.: Production and accumulation of calcium carbonate in the ocean: Budget of a nonsteady state, Global Biogeochemical Cycles, 7, 927–957, https://doi.org/10.1029/93GB02524, 1993.
- Murnane, R. J., Sarmiento, J. L., and Le Quéré, C.: Spatial distribution of air-sea CO2 fluxes and the interhemispheric transport of carbon by the oceans, Global Biogeochemical Cycles, 13, 287–305, https://doi.org/10.1029/1998GB900009, \_eprint: https://onlinelibrary.wiley.com/doi/pdf/10.1029/1998GB900009, 1999.
  - Orr, J. C., Najjar, R. G., Aumont, O., Bopp, L., Bullister, J. L., Danabasoglu, G., Doney, S. C., Dunne, J. P., Dutay, J.-C., Graven, H., Griffies, S. M., John, J. G., Joos, F., Levin, I., Lindsay, K., Matear, R. J., McKinley, G. A., Mouchet, A., Oschlies, A., Romanou, A., Schlitzer, R.,
- Tagliabue, A., Tanhua, T., and Yool, A.: Biogeochemical protocols and diagnostics for the CMIP6 Ocean Model Intercomparison Project (OMIP), Geoscientific Model Development, 10, 2169–2199, https://doi.org/10.5194/gmd-10-2169-2017, 2017.
  - Planchat, A., Kwiatkowski, L., Bopp, L., Torres, O., Christian, J. R., Butenschön, M., Lovato, T., Séférian, R., Chamberlain, M. A., Aumont, O., Watanabe, M., Yamamoto, A., Yool, A., Ilyina, T., Tsujino, H., Krumhardt, K. M., Schwinger, J., Tjiputra, J., Dunne, J. P., and Stock, C.: The representation of alkalinity and the carbonate pump from CMIP5 to CMIP6 Earth system models and implications for the carbon cycle, Biogeosciences, 20, 1195–1257, https://doi.org/10.5194/bg-20-1195-2023, publisher: Copernicus GmbH, 2023.
  - Regnier, P., Resplandy, L., Najjar, R. G., and Ciais, P.: The land-to-ocean loops of the global carbon cycle, Nature, 603, 401–410, https://doi.org/10.1038/s41586-021-04339-9, 2022.

- Resplandy, L., Keeling, R. F., Rödenbeck, C., Stephens, B. B., Khatiwala, S., Rodgers, K. B., Long, M. C., Bopp, L., and Tans, P. P.:
  Revision of global carbon fluxes based on a reassessment of oceanic and riverine carbon transport, Nature Geoscience, 11, 504–509,
  https://doi.org/10.1038/s41561-018-0151-3, number: 7 Publisher: Nature Publishing Group, 2018.
  - Revelle, R. and Suess, H. E.: Carbon Dioxide Exchange Between Atmosphere and Ocean and the Question of an Increase of Atmospheric CO<sub>2</sub> during the Past Decades, Tellus, 9, 18–27, https://doi.org/10.1111/j.2153-3490.1957.tb01849.x, 1957.
  - Ridgwell, A. and Zeebe, R.: The role of the global carbonate cycle in the regulation and evolution of the Earth system, Earth and Planetary Science Letters, 234, 299–315, https://doi.org/10.1016/j.epsl.2005.03.006, 2005.
- Rödenbeck, C., Keeling, R. F., Bakker, D. C. E., Metzl, N., Olsen, A., Sabine, C., and Heimann, M.: Global surface-ocean *p*<sup>CO<sub>2</sub></sup> and sea–air CO<sub>2</sub> flux variability from an observation-driven ocean mixed-layer scheme, Ocean Science, 9, 193–216, https://doi.org/10.5194/os-9-193-2013, publisher: Copernicus GmbH, 2013.
  - Sarmiento, J. L. and Gruber, N.: Ocean biogeochemical dynamics, Princeton University Press, Princeton, ISBN 978-0-691-01707-5, oCLC: ocm60651167, 2006.
- 1265 Sarmiento, J. L. and Sundquist, E. T.: Revised budget for the oceanic uptake of anthropogenic carbon dioxide, Nature, 356, 589–593, https://doi.org/10.1038/356589a0, 1992.
  - Sarmiento, J. L., Orr, J. C., and Siegenthaler, U.: A perturbation simulation of CO2 uptake in an ocean general circulation model, Journal of Geophysical Research: Oceans, 97, 3621–3645, https://doi.org/10.1029/91JC02849, \_eprint: https://onlinelibrary.wilev.com/doi/pdf/10.1029/91JC02849, 1992.
- 1270 Sarmiento, J. L., Monfray, P., Maier-Reimer, E., Aumont, O., Murnane, R. J., and Orr, J. C.: Sea-air CO2 fluxes and carbon transport: A comparison of three ocean general circulation models, Global Biogeochemical Cycles, 14, 1267–1281, https://doi.org/10.1029/1999GB900062, eprint: https://onlinelibrary.wiley.com/doi/pdf/10.1029/1999GB900062, 2000.
  - Stock, C. A., Dunne, J. P., Fan, S., Ginoux, P., John, J., Krasting, J. P., Laufkötter, C., Paulot, F., and Zadeh, N.: Ocean Biogeochemistry in GFDL's Earth System Model 4.1 and Its Response to Increasing Atmospheric CO<sub>2</sub>, Journal of Advances in Modeling Earth Systems, 12, https://doi.org/10.1029/2019MS002043, 2020.
  - Takahashi, T., Sutherland, S. C., Wanninkhof, R., Sweeney, C., Feely, R. A., Chipman, D. W., Hales, B., Friederich, G., Chavez, F., Sabine, C., Watson, A., Bakker, D. C., Schuster, U., Metzl, N., Yoshikawa-Inoue, H., Ishii, M., Midorikawa, T., Nojiri, Y., Körtzinger, A., Steinhoff, T., Hoppema, M., Olafsson, J., Arnarson, T. S., Tilbrook, B., Johannessen, T., Olsen, A., Bellerby, R., Wong, C., Delille, B., Bates, N., and de Baar, H. J.: Climatological mean and decadal change in surface ocean pCO2, and net sea–air CO2 flux over the global oceans, Deep Sea Research Part II: Topical Studies in Oceanography, 56, 554–577, https://doi.org/10.1016/j.dsr2.2008.12.009, 2009.
  - Tans, P. P., Fung, I. Y., and Takahashi, T.: Observational Constraints on the Global Atmospheric CO2 Budget, 247, 1990.

1280

- Terhaar, J., Frölicher, T. L., and Joos, F.: Observation-constrained estimates of the global ocean carbon sink from Earth system models, Biogeosciences, 19, 4431–4457, https://doi.org/10.5194/bg-19-4431-2022, 2022.
- Terhaar, J., Goris, N., Müller, J. D., DeVries, T., Gruber, N., Hauck, J., Perez, F. F., and Séférian, R.: Assessment of Global Ocean Biogeochemistry Models for Ocean Carbon Sink Estimates in RECCAP2 and Recommendations for Future Studies, Journal of Advances in Modeling Earth Systems, 16, e2023MS003 840, https://doi.org/10.1029/2023MS003840, 2024.
  - Wanninkhof, R., Park, G. H., Takahashi, T., Sweeney, C., Feely, R., Nojiri, Y., Gruber, N., Doney, S. C., McKinley, G. A., Lenton, A., Le Quéré, C., Heinze, C., Schwinger, J., Graven, H., and Khatiwala, S.: Global ocean carbon uptake: magnitude, variability and trends, Biogeosciences, 10, 1983–2000, https://doi.org/10.5194/bg-10-1983-2013, 2013.